CONTINUOUS AND DISCONTINUOUS MODELING OF FAILURE FOR *QUASI*-BRITTLE MATERIALS IN MODE I AND MIXED MODE (I+II)

JOSÉ FABIANO ARAÚJO MOREIRA

TESE DE DOUTORADO EM ESTRUTURAS E CONSTRUÇÃO CIVIL
DEPARTAMENTO DE ENGENHARIA CIVIL E AMBIENTAL

FACULDADE DE TECNOLOGIA

UNIVERSIDADE DE BRASÍLIA

UNIVERSIDADE DE BRASÍLIA
FACULDADE DE TECNOLOGIA
DEPARTAMENTO DE ENGENHARIA CIVIL E AMBIENTAL

CONTINUOUS AND DISCONTINUOUS MODELING OF FAILURE FOR *QUASI*-BRITTLE MATERIALS IN MODE I AND MIXED MODE (I+II)

JOSÉ FABIANO ARAÚJO MOREIRA

ORIENTADOR: FRANCISCO EVANGELISTA JUNIOR

TESE DE DOUTORADO EM ESTRUTURAS E CONSTRUÇÃO CIVIL

PUBLICAÇÃO: TD 03A/23

BRASÍLIA/DF: FEVEREIRO – 2023

UNIVERSIDADE DE BRASÍLIA
FACULDADE DE TECNOLOGIA
DEPARTAMENTO DE ENGENHARIA CIVIL E AMBIENTAL

CONTINUOUS AND DISCONTINUOUS MODELING OF FAILURE FOR *QUASI*-BRITTLE MATERIALS IN MODE I AND MIXED MODE (I+II).

JOSÉ FABIANO ARAÚJO MOREIRA

TESE SUBMETIDA AO DEPARTAMENTO DE ENGENHARIA CIVIL E AMBIENTAL DA FACULDADE DE TECNOLOGIA DA UNIVERSIDADE DE BRASÍLIA COMO PARTE DOS REQUISITOS NECESSÁRIOS PARA A OBTENÇÃO DO GRAU DE DOUTOR EM ESTRUTURAS E CONSTRUÇÃO CIVIL.

APROVADA POR:

Prof. Francisco Evangelista Júnior, PhD (ENC-UnB)
(Orientador)

Prof. Fábio Comes de Castro, D.Sc (ENM-UnB)
(Examinador Interno)

Prof. Igor Fernandes Gomes, D.Sc (CTG-UFPE)
(Examinador Externo)

Prof. Marcelo Silva Medeiros Júnior, PhD (DEECC -UFC)
(Examinador Externo)

BRASÍLIA/DF, 24 DE FEVEREIRO DE 2023.

FICHA CATALOGRÁFICA

MOREIRA, JOSÉ FABIANO ARAÚJO
Continuous and discontinuous modeling of failure for *quasi*-brittle materials in mode I and mixed mode (I+II) [Distrito Federal] 2023.

xix, 79p., 210 x 297 mm (ENC/FT/UnB, Doutor, Estruturas e Construção Civil, 2023).
Tese de Doutorado – Universidade de Brasília. Faculdade de Tecnologia.
Departamento de Engenharia Civil e Ambiental.

1. Continuum damage mechanics	2. Regularization of fracture energy
3. Cohesive zone model	4. *Quasi*-brittle materials
5. G/XFEM	6. Park-Paulino-Roesler law
I. ENC/FT/UnB	II. Título (Doutor)

REFERÊNCIA BIBLIOGRÁFICA

MOREIRA, J. F. A. (2023). Continuous and discontinuous modeling of failure for *quasi*-brittle materials in mode I and mixed mode (I+II). Tese de Doutorado em Estruturas e Construção Civil, Publicação TD 03A/23, Departamento de Engenharia Civil e Ambiental, Universidade de Brasília, Brasília, DF, 81p.

CESSÃO DE DIREITOS

AUTOR: José Fabiano Araújo Moreira.

TÍTULO: Continuous and discontinuous modeling of failure for *quasi*-brittle materials in mode I and mixed mode (I+II).

GRAU: Doutor ANO: 2023

José Fabiano Araújo Moreira
QR 510 CJ 03 Casa 08, Samambaia Sul.
72.312-603 Brasília – DF – Brasil.
jf_moreira1991@hotmail.com

ACKNOWLEDGEMENTS

I would like to address my thanks to:

- God, for always being present in my life.
- my advisor Francisco Evangelista Júnior, for his objective, safe, and competent guidance, and the idealization of the entire research.
- my dear parents Assis and Teresinha, who dedicated their lives to raising and educating their children.
- my wife Bruna Alcantara, for always being by my side in good and bad times.
- my family who live in Brasília: Francisco Araújo, Ermelina Araújo, Helton Neto, Maria Herlane, Francisco Wesley, Wallace Vicente, Rosilane Moreira, Wéllio Cristino, and Guilherme Araújo.
- Gelson Alves and Guilherme Paiva, for their friendship, encouragement, and indispensable support in the preparation of this thesis.
- the friends: Álvaro Martins, Gabriel Costa, Welington Vital, Nathaly Sarasty and Iago Almeida.
- all the professors of the Graduate Program in Structures and Civil Construction at the University of Brasília.
- CNPq for financial support.

RESUMO

MODELAGEM CONTÍNUA E DESCONTÍNUA DE FALHA PARA MATERIAIS *QUASI*-FRÁGEIS EM MODO I E MODO MISTO (I+II) DE ABERTURA DE TRINCA

Autor: José Fabiano Araújo Moreira
Orientador: Franscisco Evangelista Junior
Programa de Pós-graduação em Estruturas e Construção Civil
Brasília, Fevereiro - 2023

Este trabalho formulou e implementou abordagens contínuas e descontínuas para prever falhas em materiais quase-frágeis com comportamento de fratura em modo I e modo misto (I+II). A abordagem contínua consiste em um modelo de dano baseado na termodinâmica de processos irreversíveis, e a abordagem descontínua combina as vantagens do Modelo de Zona Coesa através da lei de Park-Paulino-Roesler e o Método dos Elementos Finitos Generalizados. As leis de evolução do dano são baseadas apenas em parâmetros físicos da mecânica da fratura, que podem ser obtidos através de testes de fratura e resistência sem a necessidade de calibração adicional, e a lei de Park-Paulino-Roesler pode ser aplicada para vários tipos de modos de fratura. Ambas as abordagens foram testadas e validadas comparando resultados para vários problemas de referência em modo I e modo misto encontrados na literatura. A comparação mostrou a eficiência e precisão das abordagens propostas em prever a resistência à tração e toda a resposta de carga-deslocamento dos experimentos para vários níveis de refinamento de malha, incluindo malhas muito grosseiras. O resultado desta tese é uma ferramenta robusta capaz de simular estruturas complexas feitas de materiais quase-frágeis para vários tipos de modos de fratura.

Palavras-chave: Mecânica do dano contínuo, Regularização da energia de fratura, Modelo de zona coesiva, Materiais quase-frágeis, G/XFEM, Lei de Park-Paulino-Roesler.

ABSTRACT

CONTINUOUS AND DISCONTINUOUS MODELING OF FAILURE FOR *QUASI*-BRITTLE MATERIALS IN MODE I AND MIXED MODE (I+II)

Author: José Fabiano Araújo Moreira
Supervisor: Franscisco Evangelista Junior
Graduate Program in Structures and Civil Construction
Brasília, February - 2023

This work formulated and implemented a continuous and discontinuous approach to predict failures in *quasi*-brittle materials for mode I and mixed (I+II) fracture behavior. The continuous approach consists of a damage model based on the thermodynamics of irreversible processes, and the discontinuous approach combines the advantages of the Cohesive Zone Model by the Park-Paulino-Roesler law and the Generalized Finite Element Method. The damage evolution laws are based only on physical parameters from fracture mechanics, which can be obtained through fracture and resistance tests without the need of further calibration, and the Park-Paulino-Roesler law can be applied to various types for fracture modes. Both approaches were tested and validated by comparison of the results of several modes I and mixed mode benchmark problems from the literature. The comparison showed the efficiency and accuracy of the proposed approaches to predict the tensile strength and the entire load-displacement response of the experiments for various levels of mesh refinement, including very coarse meshes. The result of this thesis is a robustness tool capable of simulating complex structures of *quasi*-brittle materials with various types of fracture behavior.

Keywords: Continuum damage mechanics, Regularization of fracture energy, Cohesive zone model, *Quasi*-brittle materials, G/XFEM, Park-Paulino-Roesler law.

CONTENTS

LIST OF TABLES

LIST OF FIGURES

LIST OF SYMBOLS

B	Thickness
$\mathbf{B}$	A matrix containing derivatives of shape functions
D	Damage variable
$\dot{D}$	Damage rate
$\mathbf{D_0}$	Constitutive tensor
D_i	Damage function
E	Young's Modulus
$\overline{E}$	Stiffness that depends on plane stress, plane strain, or 3D assumptions
F	The peak load of the splitting tensile strength test
F_{tip}	Branch enrichment function
$F(\varepsilon_{eq})$	Continuous and positive function of ε_{eq}
G_F	Total fracture energy
G_f	Initial fracture energy
G_{FRC}	Total fracture energy for fiber incorporation
H	Specimen depth
$I_{\varepsilon 1}$	First strain invariant (trace of the strain tensor)
$J_{\varepsilon 2}$	Second deviatoric strain invariant
K	The ratio between compressive strength and tensile strength
$\mathbf{K_{aa}}$	Matrix of the standard stiffness
$\mathbf{K_{ab}}$	Matrix of standard/enriched stiffness
$\mathbf{K_{ba}}$	Transpose matrix of $\mathbf{K_{ab}}$
$\mathbf{K_{bb}}$	Matrix of the enriched stiffness
K_{IC}	Critical stress intensity factor (fracture toughness)
L	Length
M	Number of elements on a mesh
$\mathbf{N}$	A matrix containing shape functions
P	Load
P_{max}	Peak load
S	Set of integration points located within the V-shaped
$\mathbf{T}$	Matrix of constitutive model expressed in a traction versus crack opening curve

T_n	Normal traction-displacements
T_t	Tangential traction-displacements
U_n	Normal displacement
U_t	Tangential displacement
$\mathbf{a}$	Vector of regular degrees of freedom
$\mathbf{b}$	Vector of enhanced degrees of freedom
$\bar{\mathbf{b}}$	Body forces
$\mathbf{c}$	Vector of the degree of freedom related to crack tip enrichment
d	Cylinder diameter
f_c	Compressive strength
$\mathbf{f_{ext}}$	External force vector
$\mathbf{f_{ext}}$	Internal force vector
f_t	Tensile strength
$f(\varepsilon_{eq})$	Evolving limit of the damaged surface
i	Gauss point
k	The exponent of the branch enrichment function
L	Rate of decay of the weight function
l_b	Fiber length
l_h	Localized failure finite-width region
L_{st}	Cylinder length
$\mathbf{n}$	Unit normal vector to the boundary
$\mathbf{n_i}$	Vector of the principal direction
r	Local polar coordinates at the crack (distance to the crack tip)
$\mathbf{r_i}$	Position vector in the direction of point i
$\mathbf{r_{\Gamma_d}}$	A vector in the perpendicular direction of the crack propagation
$\bar{\mathbf{t}}$	Tractions
t_n	Normal traction-separation law
t_t	Tangential traction-separation law
$\mathbf{u}$	Displacement vector
$\bar{\mathbf{u}}$	Prescribed displacement
$[\![\mathbf{u}]\!]$	Crack opening (displacement jump)
$\mathbf{x}$	Global coordinate

w	Displacement on a crack
$[\![\Delta]\!]_n$	The largest value of the normal separation of the crack
∇	Differential operators
$\boldsymbol{\mathcal{H}}$	Heaviside function
$\mathbf{I}$	Second-order identity tensor
$\mathbf{II}$	Fourth-order identity tensor
Λ_n	Normal energy constant
Λ_t	Tangential energy constant
Γ	Body boundary
Γ_t	Force boundary conditions
Γ_u	Displacement boundary conditions
Φ_F	The energy dissipated per unit volume
$\emptyset_n$	Normal fracture energy of PPR law
$\emptyset_t$	Tangential fracture energy of PPR law
Ψ	Potential form of the PPR law
Ψ_1	First kink point ratio of damage laws
Ψ_2	Second kink point ratio of damage laws
Ω	Continuous body
Ω^+	Positive region of a continuous body
Ω^-	Negative region of a continuous body
α	Shape parameters of PPR law
β	Shape parameters of PPR law
δ	Displacement
δ_1	Normal traction-displacement
$\boldsymbol{\delta}_\mathbf{a}$	The standard degree of freedom
$\boldsymbol{\delta}_\mathbf{b}$	Enriched degree of freedom
δ_k	Normal traction-displacement on the kink point
δ_f	Maximum opening displacement
θ	Local polar coordinates at the crack (angle)
$\boldsymbol{\varepsilon}$	Strain tensor
ε_1	Horizontal axis intersection of damage laws
ε_2	The maximum strain of damage laws
ε_{d0}	Critical elastic strain

ε_{eq}^{f}	Integral limit
ε_{eq}^{max}	Current maximum equivalent strain
ε_{eq}	Equivalent strain
ε_{eq}^{s}	Critical strain value
ε_{i}	Principal strain in the i direction
$\langle\varepsilon_{i}\rangle_{+}$	The positive part of ε_{i}
ε_{eq}^{MA}	Mazars equivalent strain
ε_{eq}^{VM}	von Mises equivalent strain
ε_{k1}	First kink point value of damage laws
ε_{k2}	Second kink point value of damage laws
η_{i}	Weight calculated using a Gaussian function
λ	Lamé's parameter
μ	Lamé's parameter
π	The ratio of the circumference to the diameter of the circle
$\boldsymbol{\sigma}$	Cauchy stress tensor
σ	Tractions on a crack
σ_{i}	Principal tensile stress
σ_{N}	Maximum nominal strength is induced in a structure with a pre-existing crack to cause its unstable propagation.
σ_{n}	Principal stress
σ_{max}	The normal cohesive strength of PPR law
σ_{st}	Tensile strength of the splitting tensile strength test
τ_{max}	Maximum shear stress / tangential cohesive strength of PPR law
υ	Poisson ratio
$\otimes$	Tensor product
$(\cdot)^{S}$	Symmetric part of $(\cdot)$
$\langle\cdot\rangle$	Macaulay bracket

LIST OF ABBREVIATIONS

1D	One-Dimensional domain
2D	Two-Dimensional domain
3D	Three-Dimensional domain
ASTM	American Society for Testing and Materials
CDM	Continuum Damage Mechanics
CMOD	Crack Mouth Opening Displacement
CMSD	Crack Mouth Sliding Displacement
CT	Crack Tip
$\mathrm{CTOD_c}$	Crack Tip Opening Displacement
CZM	Cohesive Zone Models
DCT	Disk-shaped Compact Tension
DENT	Double-Edge-Notched Tension
FEM	Finite Element Method
FPS	Four-Point Shear
FPZ	fracture process zone
G/XFEM	Generalized/eXtended Finite Element Method
LEFM	Linear Elastic Fracture Mechanic
PPR	Park-Paulino-Roesler
RILEM	*Réunion Internationale des Laboratoires et Experts des Matériaux*
SEN(B)	Single Edge Notched Beam
TPB	Three-Point Bending
TPFM	Two-Parameter Fracture Model

1 INTRODUCTION

One of the major concerns of engineering has been to understand and control the process of rupture or failure in materials and structures to avoid catastrophic events. Understanding the nonlinear behavior of materials has been a challenge, especially for *quasi*-brittle materials, since it presents a rupture in which small plastic deformations occur after the elastic limit and eventually lead to a sudden failure [1]. In these materials, there is a Damage/Fracture Process Zone (FPZ) ahead of the macrocrack, which size is large in comparison to the size of the crack and with the characteristic size of the structure. Most of this zone is characterized by a nonlinear behavior caused mainly by inelastic deformations. Fiber cementitious materials are an example of a material with a large process zone that has a considerable distribution of microcracks scattered around the crack tip. The FPZ present in *quasi*-brittle materials is extensively studied in the literature by a continuous approach (Continuum Mechanics) and by a discrete approach (Fracture Mechanics).

In the first approach, we include the constitutive models capable of reproducing processes of diffuse damaging and plastification that affect the response of materials ideally considered as continuous media. In this sense, the formulations that derive from the application of the damage mechanic [2, 3] stand out, whose conceptual basis is found in the Thermodynamics of Solids. The strongest objection to continuous theories is that brittle rupture is often governed by the growth of a dominant fissure. Here is the second approach. Fracture Mechanics deals with the discontinuity of the media due to the formation and growth of a macrocrack. A common idealization in Fracture Mechanics is the Cohesive Zone Model (CZM), first introduced by [4, 5] and [6], to address stress singularity at the crack tips. In these models, all nonlinearities take place in a cohesive zone ahead of the crack tip which is associated with the FPZ.

The subject of this thesis, therefore, addresses the central theme of the research activity currently underway in Computational Mechanics at the international level, namely the development, testing, and validation of new numerical formulations and their application in the modeling of nonlinear behavior of structures.

1.1 MOTIVATION

This research is justified by the limitations observed in the application of the conventional model in displacements of the finite element method in the nonlinear analysis of structures, particularly concerning the implementation of fracture and elastoplastic models of increasing importance for the simulation of rupture processes. The feasibility of this development requires investment in complementary areas that ensure high-performance indices, such as the study of the convergence and stability of numerical approximations, the exploration of adaptive enrichment techniques, and the use of computational techniques that allow the solution of nonlinear systems of large size. Thus, the motivation of this doctoral research is to contribute to the modeling of failures in *quasi*-brittle materials subject to realistic boundary conditions by using continuous and discontinuous strategies. As a contribution, robust software was created where a continuous approach based on continuous damage mechanics and a discontinuous strategy through cohesive laws and the Generalized Finite Element method was implemented to simulate the problems independent of the finite element mesh used.

1.2 OBJECTIVES

1.2.1 General objective

The present thesis aims to formulate and implement two and three-dimensional models based on continuous and discontinuous approaches for damage and crack propagation in structures of *quasi*-brittle materials for mode I and mixed mode (I+II) of failure. The continuous approach consists in formulate and implement a novel damage strategy based on fracture mechanics and on the thermodynamics of irreversible processes, and the discontinuous approach consists of implementing the Park-Paulino-Roesler (PPR) law by the framework of the Generalized/eXtended Finite Element Method (G/XFEM).

1.2.2 Specific objectives

The following specific objectives are proposed:

- Present a continuous strategy allied to the generalized finite element method that aims to propagate the crack independently of the finite element mesh;

- Implement the crack propagation considering crack tip enrichment for simulations with coarse meshes.

- Verify the efficiency of the proposed regularization strategy in overcoming the problem of non-objectivity of the mesh.

- Check the ability of the proposed models to reproduce the behavior and the maximum structural load of the benchmark tests independent of the mesh refinement and specimen size;

- Validate the models by comparison with experimental, analytical, and numerical results of benchmark problems from the literature; and

- Create a finite element program to simulate the fracture of *quasi*-brittle materials through the proposed damage model and the generalized finite element approach and cohesive laws.

1.3 CONTRIBUTIONS

The contribution of this thesis is the formulation and implementation of a continuum damage model with normalization via fracture energy and damage evolution laws based only on physical parameters obtained from resistance and fracture tests. The regularization based on normalization via fracture energy adopted to avoid the mesh non-objectivity is established to adapt the dissipated energy with a characteristic length taken equal to the typical element size of the finite element mesh. This regularization technique presents a lower computational cost when compared with others such as non-local damage variables and higher gradient fields. In the literature, was not found an article that combines a regularized continuum damage model with fracture laws based only on material properties without the need for calibration with a compatible energy balance and independent of the finite element mesh.

In addition, a discontinuous model that combines the benefits of the G/XFEM with cohesive zone laws was implemented. The constitutive law adopted to describe the nonlinear fracture processes developing ahead of the fracture tip is the potential-based PPR cohesive law. This law is more powerful and able to describe fracture propagation for various types of materials, including materials with heterogeneous structures. The cohesive zone model has been only recently explored to model fracturing problems into the G/XFEM framework and no articles are found that adopt a more powerful law such as PPR to relate the traction to the fracture.

In this way, this work is intended to contribute to the development of models able to simulate the resistance of structural members under failures in an efficient way and with mesh objectivity. Thus, contributing to advances in the analysis of structures in rupture regimes due to the propagation of two and three-dimensional cracks by the implementation of a sufficiently robust numerical tool that allows more effective (low computational cost) and realistic Three-Dimensional (3D) domain analyses of integrity and life expectancy of a structural component.

Additionally, for numerical implementations and simulations, a software based on Finite Element Method called LACHESYS was developed by the author in collaboration with researchers from the graduate program in structures and civil construction at the University of Brasilia (PECC-UnB). The LACHESYS software is written in C++ language, which makes it easy to add new tools to the software. The program simulates the nonlinear problem by the secant method, solves the equation system using the conjugate gradient technique, and makes use of the sparse allocation method to optimize the memory allocation. For mesh generation was used the open-source software Gmsh, developed by Christophe Geuzaine and Jean-François Remacle [7]. Post-processing was done using ParaView, an open-source multiple-platform application for interactive, scientific visualization, developed by Sandia National Laboratories, Kitware Inc, and Los Alamos National Laboratory.

1.4 SCIENTIFIC PRODUCTION

The scientific production during this doctorate is listed below:

- **Complete papers in conference proceedings**

J. F. A. Moreira e F. Evangelista Jr., "Modelo bidimensional contínuo-descontínuo de falha para materiais quase-frágeis," in *XXXVII Iberian Latin-American Congress on Computational Methods in Engineering*, Brasília, 2016.

J. F. A. Moreira e F. Evangelista Jr., "Implementação bidimensional do modelo de zona coesiva PPR por meio do Método dos Elementos Finitos Generalizados," in *XXXVIII Iberian Latin-American Congress on Computational Methods in Engineering*, Florianópolis, 2017.

J. F. A. Moreira and F. Evangelista Jr., “Continuous and Discontinuous Modelling of Mixed Mode Failure for *Quasi*-Brittle Materials”. In: *XL Iberian Latin-American Congress on Computational Methods in Engineering*, Natal, 2019.

- **Papers in journal**

F. Evangelista Jr. and J. F. A. Moreira. “A novel continuum damage model to simulate *quasi*-brittle failure in mode I and mixed-mode conditions using a continuous or a continuous-discontinuous strategy”. *Theoretical and applied fracture mechanics*, v. 1, p. 102745, 2020.

J. F. A. Moreira and F. Evangelista Jr., "A novel damage approach based on fracture mechanics for failure in *quasi*-brittle materials within the context of the thermodynamics of irreversible processes," In preparation.

J. F. A. Moreira and F. Evangelista Jr., " Implementation of the PPR Cohesive Zone Model in the Generalized Finite Element Method framework," In preparation.

1.5 ORGANIZATION OF THIS THESIS

The following chapters are organized in a paper format. Chapter 2 formulated and validated a new three-dimensional damage model based on the thermodynamics of irreversible processes to predict failures in *quasi*-brittle materials. Chapter 3 implemented and validated the potential-based PPR law and other cohesive zone laws into the framework of the G/XFEM to predict the mode I and mixed (I+II) fracture behavior in structures of *quasi*-brittle materials. Chapter 4 presents the general conclusions and suggestions for future work.

2 A NOVEL DAMAGE APPROACH BASED ON FRACTURE MECHANICS FOR FAILURE IN *QUASI*-BRITTLE MATERIALS WITHIN THE CONTEXT OF THE THERMODYNAMICS OF IRREVERSIBLE PROCESSES

This research aims to formulate and implement a novel three-dimensional damage approach based on the thermodynamics of irreversible processes able to predict failures in *quasi*-brittle materials for crack opening mode I and mixed mode. This damage approach is based on a new damage evolution law using only physical parameters from fracture mechanics, which can be obtained through fracture and resistance tests without the need for further calibration. The problem of non-convergence is avoided by local energy dissipation controlled by the regularization of fracture energy and the element length ensures that different mesh densities dissipated the same specific energy during the damage evolution. Comparison with experimental results for various types of tests in mode I and mixed mode conditions were performed: three-point bending in a single-edge notch beam, double-edge-notched tension specimen, concrete slab on a soil foundation, and a real scale dam. The results confirmed the efficiency and accuracy of the damage approach in predicting maximum load and entire load-displacement curves always presenting good agreement with experiments. In addition, comparisons of results with other simulations of the literature showed that the proposed strategy can provide equivalent accuracy using coarser meshes. The results of the concrete slab on a soil foundation show that the proposed damage approach provides good results even with coarsest meshes that use up to 28 times fewer elements than numerical reference results from the literature.

2.1 INTRODUCTION

The behavior of *quasi*-brittle materials such as concrete, rocks, mortar, and others is particularly difficult to predict. Because of this, the numerical modeling of the failure of these materials has received important attention from researchers over the last decades. The researchers have adopted different approaches, leading to different models, such as discrete crack models [8], extended finite element method [9], discrete element method [10], smeared crack models [11], continuum damage mechanics [12], and others. Many of these models consider that a strain localization resulting from a microcracking process appears in a region called the Fracture Process Zone (FPZ) located ahead of the macrocrack. Macrocracks are the consequence of microcrack growth and coalescence. A feature of this zone is that it is large when compared to the size of the crack and the characteristic size of the structure [11, 13-17], most of it is characterized by a nonlinear behavior caused mainly by inelastic deformations. This FPZ is widely studied in the literature by fracture mechanics and continuum mechanics [18-25].

Fracture mechanics deals with discontinuities caused by the formation and growth of a macrocrack. A very common idealization is the Cohesive Zone Model (CZM), initially introduced by Barenblatt [4, 5] and Dugdale [6], to address the crack tip singularities. In these models, all nonlinearities are located in a cohesive zone ahead of the crack tip that is associated with FPZ. The pioneering paper of Hillerborg *et al.* [13] applied the CZM concepts to overcome some limitations of the Linear Elastic Fracture Mechanism (LEFM), called the fictitious crack model, using the finite element method to investigate fracture behavior in concrete. The CZM has been widely used in materials and structures analysis [17, 22, 26-33].

Continuum mechanics has also been used to describe the dissipation behavior of materials induced by the initiation and development of microcracks around a macrocrack. One approach is the Continuum Damage Mechanics (CDM), which considers variable states related to the loading direction to describe the irreversible processes, such as the state of damaging, hardening, and softening [34, 35]. The main drawback of damage models is the non-convergence of numerical results on mesh refinement. This is often referred in the literature as mesh non-objectivity [17, 36-38], and is related to changing the differential equation of motion from elliptical to hyperbolic in static problems, becoming the boundary value problem ill-posed [39]. Furthermore, unrealistic stress transfer between completely damaged elements is reported due to the inability of the continuous field model to represent the discontinuity [40]. The first drawback cited can be overcome by regularization techniques based on non-local damage variables [38, 41-46], higher gradient fields [37, 47-52], or normalization using fracture energy [53-57]. It is important to point out that the first two techniques are costly numerically; this cost is caused by the additional task related to the determination of an integral radius parameter or a gradient parameter, whose physical meaning is considered ambiguous [58, 59]. Moreover, it has been reported that these first two techniques may introduce some inconsistencies, such as artificial spreading of damage

[60], incorrect location of damage initiation and incorrect damage propagating after failure due to non-local averaging [61], deficiencies at capturing spalling properly in dynamics [62].

As can be observed, the regularization technique based on non-local damage variables or higher gradient fields seems to be not attractive. This leads us to the third regularization technique based on normalization using fracture energy. This normalization consists of the dissipation of energy in a specific region, related to smeared microcracks, called crack bandwidth which is similar to the FPZ. The characteristic width of this crack band is related to the finite element size in the classical Finite Element Method (FEM) formulation, which remains local because it avoids the determination of additional non-local parameters such as the integral radius parameter and gradient parameter. This concept of regularization emerged in the 1980's from works of [14, 53, 63-68] and has been called in the literature as the crack band approach. Jirásek and Bauer [55] analyzed various components of a modeling strategy based on this approach on the energy dissipated in the failure process such as the formula for estimation of the crack bandwidth and equivalent strain expression for strain-driver. The results of the study showed that these two components have a strong influence on the global response. Although the different equivalent strain expressions exhibit very close behavior in the One-Dimensional (1D) domain, it does not necessarily happen in the Two-Dimensional (2D) domain, differences may arise due to the biaxial state of tension. For the effective width of a crack band, the author showed that it is affected by other components such as the element type, element shape, and direction of the crack band concerning the mesh lines and by the integration scheme for higher-order elements. Their analyses were restricted to 1D and 2D problems in mode I for materials with isotropic and *quasi*-brittle behavior.

Published works have used the normalization with fracture energy to prevent the non-objectivity of numerical response on finite element simulations. Wosatko *et al.* [57] examined the efficiency of two different established damage-plasticity models for concrete from the viewpoint of a localization limiter and the so-called crack-closing effect. One of the models uses two methods for reducing the non-objectivity and one of the methods is based on the fracture energy and the characteristic width of a band. This regularization did not provide full mesh objectiveness. Kurumatani *et al.* [56] proposed a damage model based on fracture mechanics for *quasi*-brittle materials and validated it with 2D and 3D numerical experiments in mode I and mixed. Their damage model uses a simple exponential evolution law as a function only of the fracture energy and the element length normalizes that. For numerical simulations, the mesh-size dependency was avoided. The evolution law was obtained from the incorporation of the CZM into the conventional damage model by the framework of fracture mechanics.

The combination of a discontinuous approach through fracture mechanics to a continuous approach through damage mechanics has been receiving large attention from researchers. The papers [26, 40, 69-74] have successfully combined continuous and discontinuous approaches to model crack damage and propagation in 2D and 3D domains. Some papers make use of the advantages of developed methods for crack propagation [75] and elastic-degradation constitutive models [76-78] that use the Partition of Unit, such as the Generalized/eXtended Finite Element Method (G/XFEM). However, approaches that combine CZM with methods that replace the cracking by the degradation of stiffness represented by regularized CDM, like that proposed by [56], are recent and there are few works in this area. Therefore, additional studies are necessary to incorporate other important fracture parameters as well as other fracture laws and improve the potential of this approach for other more complex numerical problems. The literature was not found a paper that combines the regularized CDM with fracture laws based only on material properties without the need for calibration with a compatible energy balance and independent of the finite element mesh. A paper that is validated not only with crack patterns but also with quantitative analysis with softening experimental curves for modes I and mixed of fracture in *quasi*-brittle materials with and without fiber incorporation.

This chapter formulated a 3D damage approach based on fracture mechanics and on the thermodynamics of irreversible processes for the mode I and mixed (I+II) of crack opening to predict the failures in *quasi*-brittle structures. Its main contribution is the development of a model able to simulate the resistance of structural members under mode I and mixed failures efficiently and with mesh objectivity. The damage evolution law is based on a bilinear law related only to physical parameters obtained in resistance and fracture tests without the need for additional calibration or curve fitting for the sample response curve. Validation was done by comparison with experimental results for various types of tests and different modes of failure. Another key contribution of this work is the 3D simulation of a concrete slab on an elastic foundation and quantitative comparison with the experimental data. In addition, the robustness of the proposed approach was compared with other recent models of literature.

This chapter is organized as follows. Section 2.2 presents the problem definition. Section 2.3 develops the proposed strategy formulation for 1D and its extension to a multi-dimensional problem by a strain driver based on the Mazars and on the modified von Mises equivalent strain. The damage laws and experimental testing used to identify its parameter are detailed. In section 2.4, the model is validated by several numerical problems that involve mode I and mixed failure. The ability to reproduce the corresponding experimental result with mesh-objectivity is demonstrated, proving the robustness of the model in reproducing the failure of *quasi*-brittle materials with and without fiber incorporation.

2.2 PROBLEM DEFINITION

The equilibrium equation and boundary conditions for a continuous body Ω, with boundary $\Gamma = \Gamma_t \cup \Gamma_u$, as shown in Figure 2.1, are:

$$\nabla \cdot \boldsymbol{\sigma} + \bar{\mathbf{b}} = 0 \text{ in } \Omega$$

$$\mathbf{u} = \bar{\mathbf{u}} \text{ on } \Gamma_u \qquad (2.1\text{a-c})$$

$$\boldsymbol{\sigma} \cdot \mathbf{n} = \bar{\mathbf{t}} \text{ on } \Gamma_t$$

in which $\boldsymbol{\sigma}$ is the Cauchy stress tensor, $\bar{\mathbf{b}}$ represents the body forces, $\mathbf{n}$ is a unit normal vector to the boundary $\Gamma(\Gamma_t \subset \Gamma)$, $\bar{\mathbf{t}}$ are the tractions prescribed on Γ_t, $\bar{\mathbf{u}}$ have prescribed displacement on Γ_u.

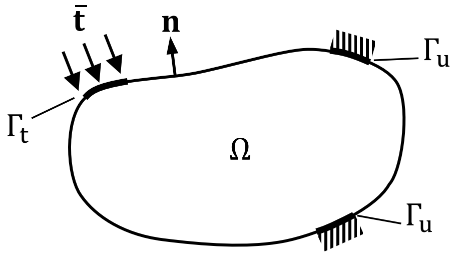

Figure 2.1 – Continuum Body Ω and boundary conditions.

It is assumed a constitutive linear elastic relation of the form:

$$\boldsymbol{\sigma} = \left[1 - \mathrm{D}\left(\varepsilon_{eq}\right)\right]\mathbf{D_0}\boldsymbol{\varepsilon} \qquad (2.2)$$

in which $D(\varepsilon_{eq})$ is a damage variable, in the range $0 \leq D \leq 1$, that maps the damaged state of the body through an equivalent strain $\varepsilon_{eq}(\varepsilon)$, $\boldsymbol{\varepsilon}$ is the strain tensor, and $\mathbf{D_0}$ is the constitutive tensor of the undamaged state defined for the linear elastic case as:

$$\mathbf{D_0} = \lambda(\mathbf{I} \otimes \mathbf{I}) + 2\mu\mathbf{II} \tag{2.3}$$

in which λ and μ are Lamé's parameters, **I** and **II** are second and fourth-order identity tensors, for the case of small strains:

$$\boldsymbol{\varepsilon} = \nabla^S \mathbf{u}(\mathbf{x}) \tag{2.4}$$

in which $(\cdot)^S$ refers to the symmetric part of $(\cdot)$ and $\mathbf{u}(\mathbf{x})$ is the displacement vector at global coordinates $\mathbf{x}$. Equation (2.2) shows that the damage variable reduces the stress with the increase of strain with no plastic strain considered. This is suitable for materials and structures that present a *quasi*-brittle type of failure which is recognized to macroscopically fail with negligible plastic strain and without yielding phenomenon [1, 17]. Moreover, in the absence of high confined compression, no work hardening is observed unless artificial fibers are added as an extra material component [33].

The damage variable $D(\varepsilon_{eq})$ describes the material softening as a result of dissipated energy during the irreversible processes of damage by microcrack evolution and coalescence during the condition $0 \leq D(\varepsilon_{eq}) \leq 1$, when no discontinuity is present (Figure 2.1). The next section describes the continuum damage model representing this state.

2.3 PROPOSED DAMAGE APPROACH

This section presents the proposed strategy to simulate failure based on a continuum damage model (CDM) applied to the *quasi*-brittle materials under mode I or mixed mode (I+II) crack propagation. The fundamental hypotheses, which define the capacity and scope of the model, consider that: (i) the damage state is represented by a scalar variable D $(0 \leq D \leq 1)$; (ii) the material is considered elastic and neither plastic nor inelastic deformations are considered; (iii) the damage state variable D relates to the strain tensor by an equivalent strain ε_{eq}, which controls the damage evolution process.

2.3.1 Control variable and damage surface activation criteria

Two different equivalent strain (ε_{eq}) definitions are considered here, and the application of either one is based on the type of failure. For cases where there is a predominance of hydrostatic deformations and the local shear strain are negligible (mode I), the ε_{eq} presented by Mazars [79], here called ε_{eq}^{MA}, is suggested by literature as a simple and efficient measurement [11, 40, 55, 79-82]

$$\varepsilon_{eq}^{MA} = \sqrt{\sum_{i=1}^{3}\left(\langle\varepsilon_i\rangle_+\right)^2} \tag{2.5}$$

with $\langle\varepsilon_i\rangle_+ = (\varepsilon_i + |\varepsilon_i|)/2$ and ε_i is the principal strain in the i direction.

In situations where shear stresses are not negligible in the strain state definition (*i.e.* mixed mode), the modified von Mises equivalent strain, here called ε_{eq}^{VM}, is a good alternative for the damage control variable [11, 40, 55, 80, 83, 84]

$$\varepsilon_{eq}^{VM} = \frac{K-1}{2K(1-2\upsilon)}I_{\varepsilon 1} + \frac{1}{2K}\sqrt{\frac{(K-1)^2}{(1-2\upsilon)^2}I_{\varepsilon 1}^2 + \frac{12k}{(1+\upsilon)^2}J_{\varepsilon 2}} \tag{2.6}$$

in which $I_{\varepsilon 1}$ is the first strain invariant (trace of the strain tensor), $J_{\varepsilon 2}$ is the second deviatoric strain invariant, K is the ratio between compressive strength (f_c) and tensile strength (f_t) and υ is the Poisson ratio.

The criterion for the damage evolution is related to the equivalent strain when it reaches a critical strain value (ε_{eq}^{s}), with the damage threshold function given as:

$$f(\varepsilon_{eq}) = \varepsilon_{eq} \leq \varepsilon_{eq}^{s} \tag{2.7}$$

with

$$\varepsilon_{eq}^{s} = \max\left\{\varepsilon_{d0}, \varepsilon_{eq}^{max}\right\} \tag{2.8}$$

in which ε_{eq}^{max} is the current maximum equivalent strain and ε_{d0} is a critical elastic strain corresponding to the tensile strength of the material $\varepsilon_{d0} = f_t/E$ in which E is Young's Modulus. Considering the limit state, $f(\varepsilon_{eq}) = 0$, Equation (2.7) becomes $\varepsilon_{eq} = \varepsilon_{eq}^{s}$ which defines the evolving limit of the damaged surface, $f(\varepsilon_{eq})$. Assuming the damage rate can be described by a function $F(\varepsilon_{eq})$, it can be written to have a thermodynamically consistent model:

$$\dot{D} = \begin{cases} F(\varepsilon_{eq}) & \text{if } f(\varepsilon_{eq}) = 0 \text{ and } \dot{f}(\varepsilon_{eq}) > 0 \\ 0 & \text{if } f(\varepsilon_{eq}) < 0; \text{or } f(\varepsilon_{eq}) = 0 \text{ and } \dot{f}(\varepsilon_{eq}) < 0 \end{cases} \tag{2.9}$$

in which $F(\varepsilon_{eq})$ is a continuous and positive function of ε_{eq} describing the damage evolution. Considering a monotonic loading history up to a crack opening of ε_{eq}^{f}:

$$D(\varepsilon_{eq}) = \int_0^{\varepsilon_{eq}^{f}} F(\varepsilon_{eq}) d\varepsilon_{eq} \tag{2.10}$$

The above equation can be rewritten in the form:

$$\begin{gathered} D(\varepsilon_{eq}) = D_0(\varepsilon_{eq}) + D_1(\varepsilon_{eq}) + \cdots + D_i(\varepsilon_{eq}) + \cdots + D_n(\varepsilon_{eq}) \\ D_i(\varepsilon_{eq}) = \int_{\varepsilon_{eq_i}}^{\varepsilon_{eq_{i+1}}} F_i(\varepsilon_{eq}) d\varepsilon_{eq} \text{ for } \varepsilon_{eq_i} \leq \varepsilon_{eq} \leq \varepsilon_{eq_{i+1}} \end{gathered} \tag{2.11}$$

with $\varepsilon_{eq_i} = 0$ for D_0 and $\varepsilon_{eq_{i+1}} = \varepsilon_{eq}^{f}$ for D_n. This equation allows that each function $D_i(\varepsilon_{eq})$ can describe a distinct phenomenon within the softening process. Each function $F_i(\varepsilon_{eq})$ is continuous within the respective limits of the integration ($\varepsilon_{eq_i} \leq \varepsilon_{eq} \leq \varepsilon_{eq_{i+1}}$). Note that the form of Equation (2.11) allows generalized damage laws such as exponential, bilinear, or trilinear to cite a few.

2.3.2 Damage evolution laws

The proposed approach establishes that a localized failure finite-width region, l_h, relates the energy dissipated per unit volume upon complete failure (Φ_F), with the fracture energy (G_F) which is the energy dissipated per unit area of the macroscopic crack surface, through the relation $G_F = l_h \Phi_F$. This relation is the basis of the regularization by the fracture energy method, and it has been used in literature over the past decades [55, 63, 65, 67, 85, 86]. Following this equivalence, the constitutive relation σ-ε for the strain softening curve of the proposed continuum damage model is related to a finite-width region (or band) l_h. Therefore, we formulated the scalar damage variable based on a traction-displacement (σ-w) cohesive fracture law, such that $D(\sigma\text{-}\varepsilon_{eq})$ is obtained from (σ-w), with $w = \varepsilon_{eq} l_h$. Regarding the implementation in a finite element framework, the damage evolution is appropriately adjusted to the width of the numerically resolved localized band by the finite element mesh. Hence, the regularization procedure establishes that the width of the localized band is defined as an equivalent size of the elements in the mesh. The constitutive Equation **Erro! Fonte de referência não encontrada.** and all formulation in Section 2.2 and Section 2.3.1 remains the same since it is independent of the damage evolution law. Only the damage evolution law $D(\varepsilon_{eq})$, detailed in the next paragraphs, that is modified to adapt the energy dissipation to each finite element size in the mesh regions undergoing the damage process. In our approach, this size is estimated by projecting the element onto the direction of the major principal strain axis taken at the element center. This projection method is detailed in [55], which shows its superior performance among other alternatives, especially the commonly adopted equivalent size as the square root of the finite element area or the cubic root of the finite element volume for 2D and 3D elements, respectively.

A specific bilinear softening law for cohesive zone models was formulated in [87] and further used in [33, 88] to successfully describe the traction-displacement behavior for mode I fracture of conventional *quasi*-brittle materials. Based on that curve, and the regularization of the energy dissipated in the volume with the $G_F = l_h \Phi_F$, a strain-softening law σ-w is assumed to describe the fracture process zone ahead of the crack tip as shown in Figure 2.2a. The energy dissipation at the nonlinear damage/fracture zone is decoupled into two regions with the corresponding initial (G_f/l_h) and total (G_F/l_h) dissipated energies. Herein, the initial fracture energy (G_f) is the energy release rate, which can be defined as $G_f = \frac{K_{IC}}{\overline{E}}$, in which K_{IC} is the critical stress intensity factor (fracture toughness), and $\overline{E}$ is the stiffness that depends on plane stress, plane strain, or 3D assumptions. The correspondent bilinear damage law $D(\varepsilon_{eq})$ is shown in Figure 2.2b. The damage law is depleted when all the fracture energy (G_F/l_h) is dissipated ($D \rightarrow 1$) and $\varepsilon_{eq} \rightarrow \varepsilon_2$.

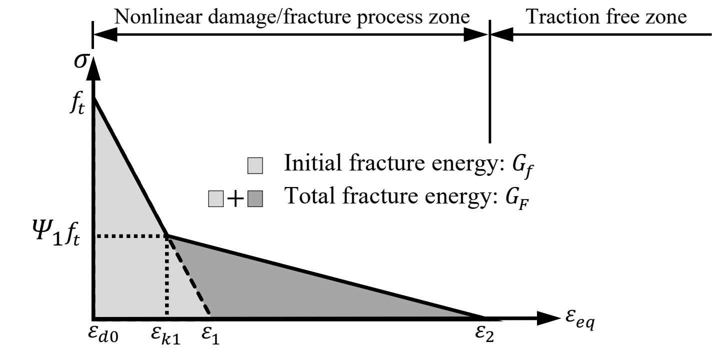

(a)

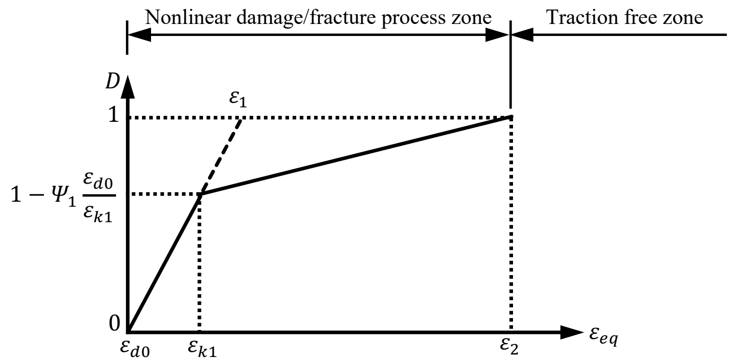

(b)

Figure 2.2 – Damage evolution law: (a) bilinear traction-strain (σ-ε_{eq}) curve (adapted from [30, 33]); (b) bilinear damage evolution law

The key coordinate points ($\varepsilon_{d0}, \varepsilon_{k1}, \varepsilon_1, \varepsilon_2, \Psi_1$) that define the damage law are based only on material properties from fracture and resistance properties: fracture energies (G_f and G_F); critical Crack Tip Opening Displacement ($CTOD_c$); and f_t. Those quantities are determined from standard tests, as specified forward in this section.

The G_f defines the horizontal axis intersection (ε_1) of the initial softening slope curve.

$$\varepsilon_1 = \frac{2G_f}{f_t l_h} \tag{2.12}$$

Park *et al*. [31] demonstrated that the kink point value (ε_{k1}) can be assumed to be the $CTOD_C$, resulting in the kink point ratio as:

$$\Psi_1 = 1 - \frac{CTOD_C\, f_t}{2G_f} \tag{2.13}$$

In situations in which the $CTOD_C$ is unknown, Bažant [89] points out that the range $0.15 \leq \Psi_1 \leq 0.33$ can be assumed. Wittman *et al*. [90] suggest a fixed value of $\Psi_1 = 0.25$ based on a comprehensive experimental analysis.

The maximum strain undertaken by the material (ε_2) is obtained by equalizing the total fracture energy (G_F) with the area under the bilinear softening curve given by:

$$\varepsilon_2 = \frac{2}{\Psi_1 f_t l_h}\left[G_F - (1-\Psi_1)G_f\right] \tag{2.14}$$

Following the same approach that results in the bilinear law, a trilinear law for fiber-reinforced cementitious materials can be formulated, such as suggested by Park *et al.* [31] and Evangelista Jr. *et al.* [91]. In this case, the energy dissipation at the nonlinear damage/fracture zone is decoupled into three regions with the corresponding initial (G_f/l_h), and total (G_F/l_h) dissipated energies of bilinear law added to the total fiber (G_{FRC}/l_h) dissipated energies, as can be shown in Figure 2.3a. The correspondent trilinear damage law $D(\varepsilon_{eq})$ is shown in Figure 2.3b.

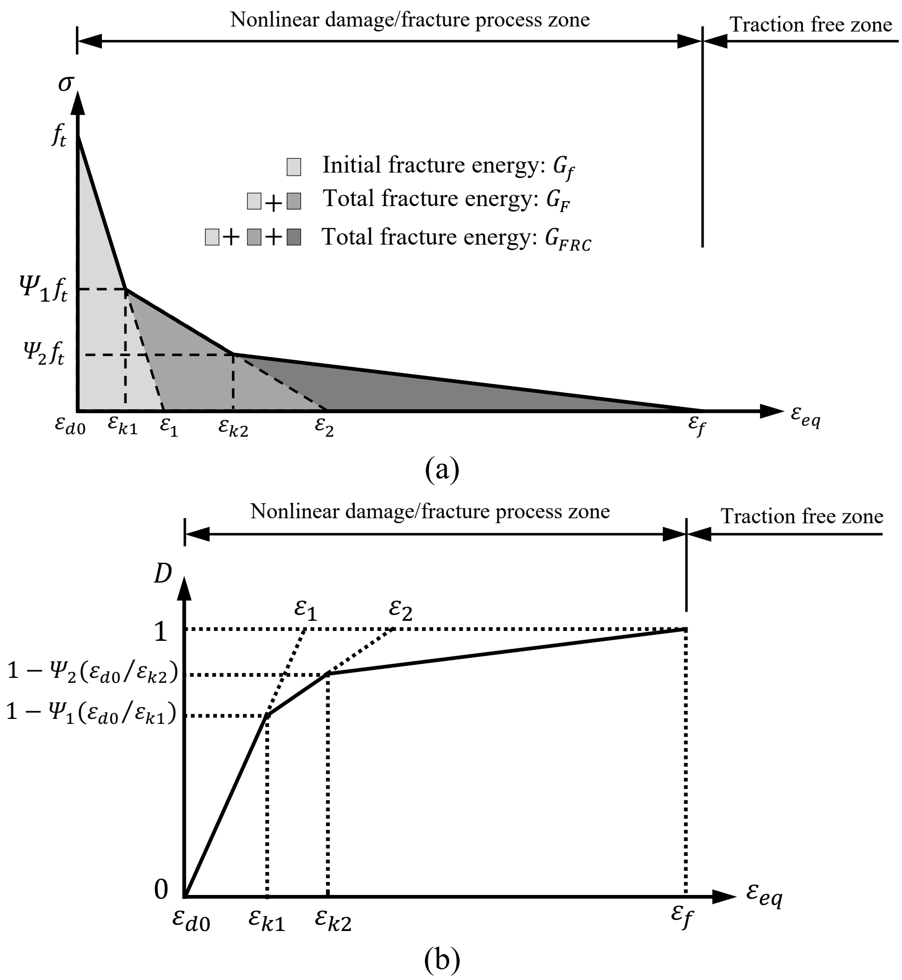

Figure 2.3 – Damage evolution law: (a) trilinear traction-strain (σ-ε_{eq}) curve (adapted from [33]); (b) trilinear damage evolution law

For fiber, an advantage of the trilinear softening model is that several of its parameters are the same as the bilinear softening model up to the first kink point ε_{k1}. The other parameters are based on the total fracture energy G_{FRC} and $\varepsilon_f l_h$ (here assumed to be 50% of the fiber length). Thus:

$$\varepsilon_{k2} = \varepsilon_2 - \frac{\Psi_2}{\Psi_1}(\varepsilon_2 - \varepsilon_{k1}) \tag{2.15}$$

in which the second kink point ratio Ψ_2 is

$$\Psi_2 = \frac{2(G_{FRC} - G_F)}{f_t l_h(\varepsilon_f - \varepsilon_2)} \tag{2.16}$$

The correspondent standard tests to determine the tensile strength and the aforementioned fracture properties are listed in Table 2.1. The fracture parameters for mode I are determined using [92] based on the Two-Parameter Fracture Model (TPFM) proposed in [93], for a Single Edge Notched Beam [SEN(B)] in a Three-Point Bending (TPB) test. The reader can find further details about the use of those tests to determine fracture properties in [92, 94, 95].

Table 2.1 – Standard tests to determine damage parameters.

Properties	**Test description**	**Type of testing**	**Recommended standard**
Damage threshold			
f_t	Tensile strength	Indirect (split) tension	ASTM C496-96 [96]
Mode I fracture			
K_{IC}	Critical stress intensity factor	SEN(B) test	RILEM [92]
$CTOD_C$	Critical crack tip opening displacement	SEN(B) test	RILEM [92]
G_F	Total fracture energy for concrete	SEN(B) test	RILEM [92]
G_{FRC}	Total fracture energy for fiber-reinforced concrete	SEN(B) test	RILEM [92]

2.3.3 Uniaxial testing

Simulations were carried out on a body with unit dimensions to show the damaging behavior in a structure submitted to different loading conditions and to evaluate the consistency of the proposed method. These loading conditions range from uniaxial tension (mode I), through mixed states (mode I+II), to pure shear (mode II). The material parameters used are $E = 32$ GPa, $\upsilon = 0.20$, $f_c = 58.3$ MPa and $f_t = 4.15$ MPa end the fracture parameters are $G_f = 56.6$ N/m, $G_F = 164.0$ N/m and $CTOD_C = 0.0186$ mm. These parameters were obtained from the experimental program of Roesler *et al.* [30]. The simulations considered the plane stress state. Figure 2.4 shows a graphic with a surface response for principal stress σ_n end maximum shear stress τ_{max} for ε_{eq}^{MA} and ε_{eq}^{VM}.

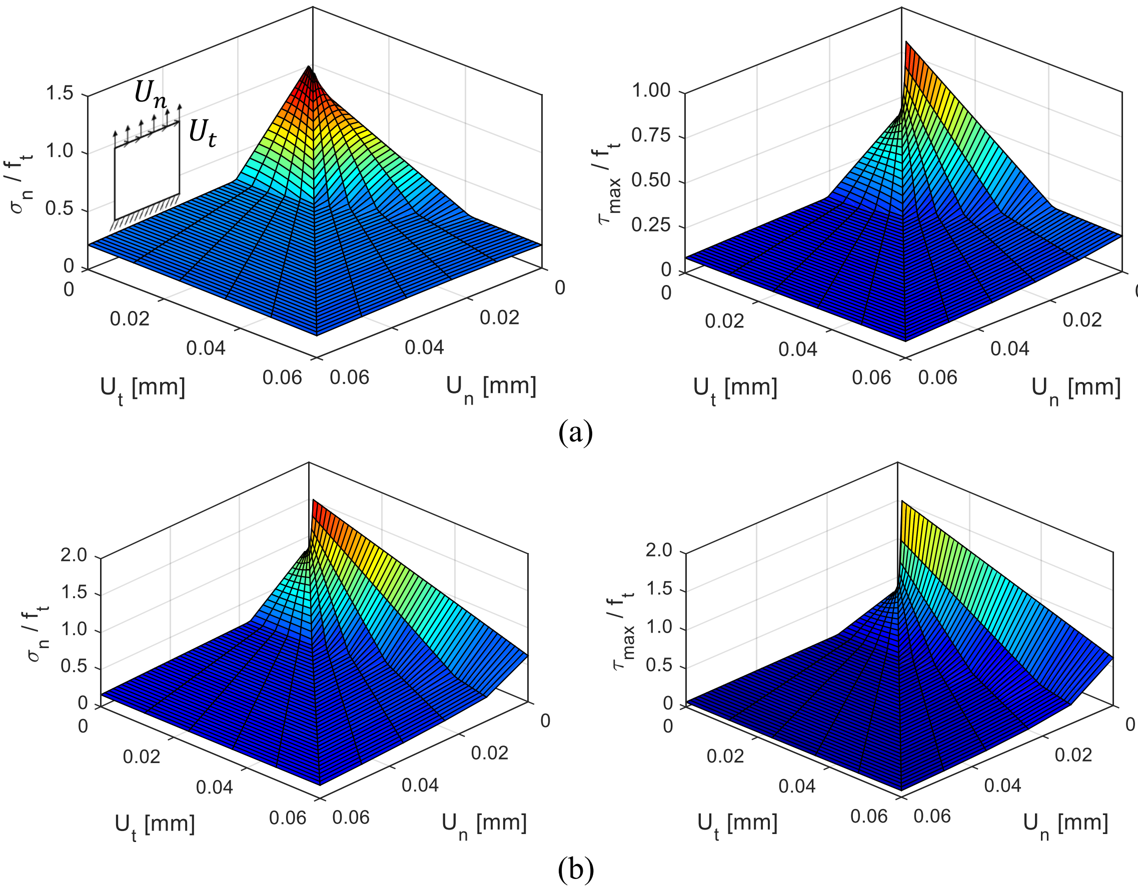

Figure 2.4 – Normalized response surface of σ_n and τ_{max} stress *versus* normal U_n and tangential U_t displacement for (a) ε_{eq}^{MA} and (b) ε_{eq}^{VM}.

As shown in Figure 2.4, for mode I ($U_t = 0$) to pure mixed mode ($U_n = U_t$) of crack opening, both equivalent deformations present results consistent with the proposed approach. Since that region of surface response is completely below f_t, with σ_n close to the value of f_t and then decreasing continuously in bilinear form. Additionally, the τ_{max} value is close to half of σ_n, which is expected by the elasticity theory, which shows that in the transformation from uniaxial stress state to maximum shear state, the maximum shear is equal to half the normal stress. For the region located between the pure mixed mode and mode II ($U_n = 0$), the principal stress results in values greater than f_t when used ε_{eq}^{VM}, what doesn't make sense physically, moreover, the shear stress values contradict the elasticity theory. Therefore, the aspect of the surfaces shows that the damage law proposed here will not be recommended for this range of crack openings.

2.4 NUMERICAL SIMULATIONS

In this section, the proposed damage approach was applied to *quasi*-brittle failure in SEN(B) specimens test, Double-Edge-Notched Tension (DENT) specimen test, and concrete slabs on an elastic soil foundation. The secant method procedure has been used to trace the response in the nonlinear regime, where the adopted residue tolerance for convergence was 10^{-4}. Three-dimensional simulations were carried out using four-node tetrahedral finite elements and the estimated curves were compared with experimental results in all specimen configurations.

2.4.1 Single edge notch beam tests [SEN(B)]

An experimental program was designed by Roesler *et al.* [30] to investigate the concrete monotonic fracture. The experimental program consists of a series of tests using three sizes of SEN(B) in TPB configuration. Table 2.2 lists the dimensions of each beam tested, the test configuration with the geometry and boundary conditions is shown in Figure 2.5a.

Table 2.2 – SEN(B) specimen dimensions (mm).

Depth (H)	Length (L)	Thickness (B)	Notch (a_0)	Span (S)
63	350	80	21	250
150	700	80	50	600
250	1100	80	83	1000

Numerical simulations based on the experimental program of [30] were completed to verify that the proposed approach can predicts the peak load (P_{max}) and softening behavior of concrete for multiple specimen depths. Three simulations per specimen depth were performed adopting different mesh refinements at the central region, all meshes are shown in Figure 2.5. The material and fracture properties provided by [30] were: $E = 32$ GPa, $\upsilon = 0.20$, $f_c = 58.3$ MPa, $f_t = 4.15$ MPa, $G_f = 56.7$ N/m, $CTOD_c = 0.0186$ mm, $G_F = 119$ N/m for specimen depth $H = 63$ mm, $G_F = 164$ N/m for $H = 150$ mm and $G_F = 167$ N/m for specimen depth $H = 250$ mm. The test control is performed through displacement increments at the line load application P, according to the experimental test.

The width of the notch adopted in the meshes was 1 mm for specimen depth H = 63 mm and 2 mm for the other two specimens.

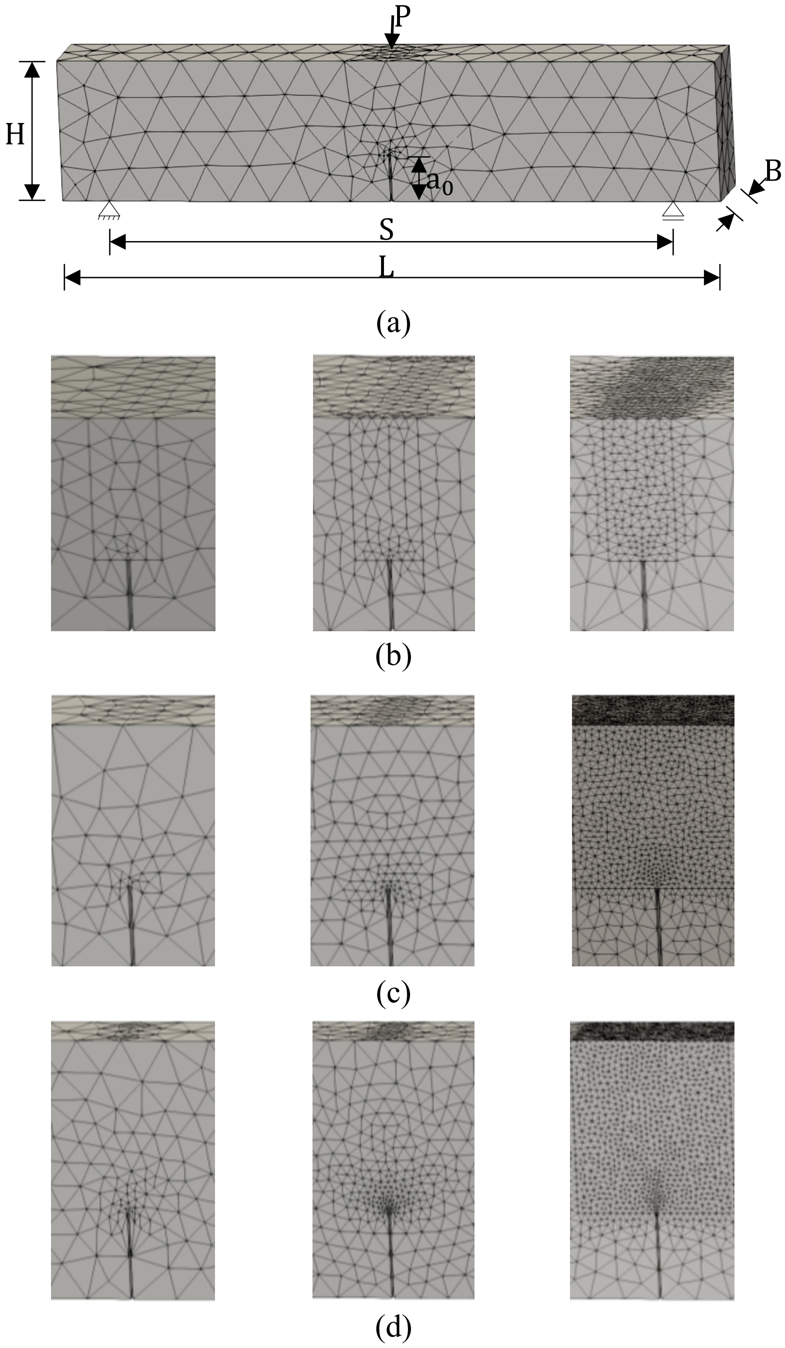

Figure 2.5 – SEN(B) specimen test: (a) geometry and boundary conditions; mesh refinements of the specimen depth (b) H = 63 mm, (c) H = 150 mm, and (d) H = 250 mm.

The numerical P *versus* Crack Mouth Opening Displacement (CMOD) curves were obtained with ε_{eq}^{MA} and ε_{eq}^{VM}, and were compared with the experimental response in Figure 2.6. The determination of the peak load P_{max} and softening curve in the numerical prediction was directly based on the fracture properties and no further steps were needed to fit the numerical simulations with the experimental results. The results show that the proposed approach was able to estimate with good agreement the experimental curves, this is expected because these states are numerically similar. In general, the P_{max} obtained with ε_{eq}^{MA} is larger than ε_{eq}^{VM} and its softening curve is most brittle, this behavior is reported in [55] and is caused to the triaxial tension state at the crack front. It is important to note that although ε_{eq}^{VM} is defined for mixed-mode cases, it was also able to estimate the mode I case.

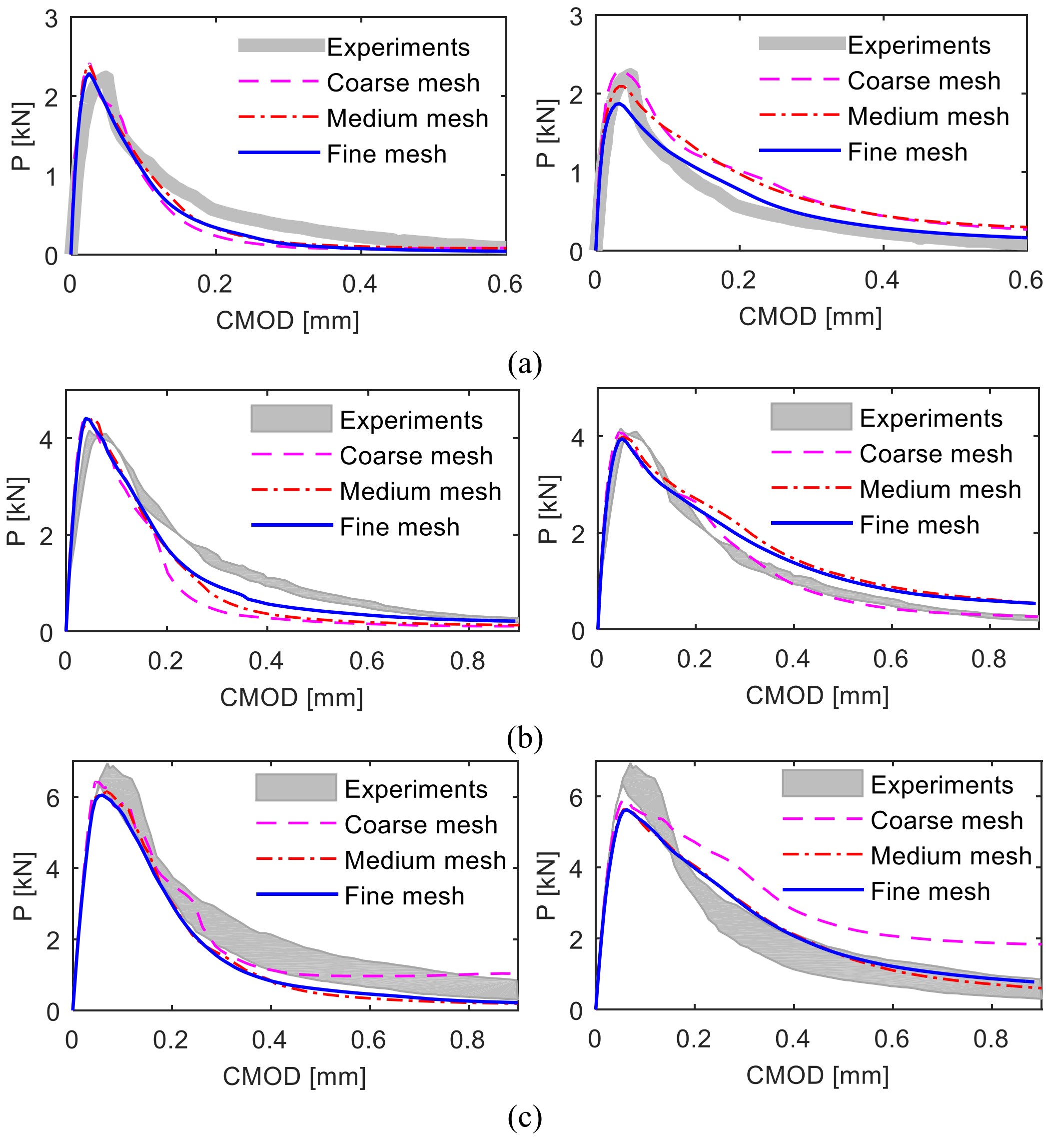

Figure 2.6 – Experimental and predicted P-CMOD curves for the SEN(B) specimen depth (a) H = 63 mm, (b) H = 150 mm, and (c) H = 250 mm. To the left, are the results for ε_{eq}^{MA} and to the right ε_{eq}^{VM}.

The P_{max} values of the experiment, which is essential to determine the concrete fracture properties, were compared to the values obtained from the numerical simulation. For ε_{eq}^{MA}, the P_{max} was under-predicted for the 63 mm and 250 mm beam depth and upper-predicted for the 150 mm beam depth, the relative difference between experimental and numerical was less than 10%, as shown in Table 2.3. For ε_{eq}^{VM}, the P_{max} was under-predicted for all beam depths, with the maximum error being 17.3% for the 63 mm beam depth. All notch initially tested by [30] were cast into the specimen. However, three 63 mm depth beams were cut from the larger beams after failure, and those data were not considered here.

Simulations with three different mesh refinement for each specimen depth were performed to evaluate the mesh objectiveness, the number of elements used in each mesh is shown in Table 2.3. The results show that the proposed approach with regularization adopted, which establishes the dissipation of fracture energy proportional to the characteristic length of the finite element, can produce mesh objectivity. This is emphasized by the convergence of both P_{max} and softening curves for the coarse, medium, and fine meshes. With the proposed regularization, we noticed that even the results of coarse meshes are similar to the more accurate results provided by the refinement of the mesh for both P_{max} and softening curves. The exception is the 63 mm specimen depth simulated with ε_{eq}^{VM}, which presented a greater variation of P_{max} than the other simulations groups, however, a greater variation of P_{max} also is observed for experiments of [30].

Table 2.3 – Comparison of the P_{max} with experimental data for SEN(B) cast specimen; and the number of elements in the meshes.

Specimen depth (H) [mm]	Experimental data mean (range) [kN]	$\mathbf{P_{max}}$ [kN] ε_{eq}^{MA}	ε_{eq}^{VM}	Rel. Diff. [%] ε_{eq}^{MA}	ε_{eq}^{VM}	$\mathbf{N_{elem}}$
63	2.26	2.41	2.29	6.64	1.32	1,786
		2.39	2.09	5.75	7.52	4,593
		2.29	1.87	1.33	17.3	19,918
150	4.12 (4.09– 4.16)	4.38	4.08	6.31	0.98	2,455
		4.42	3.99	7.28	3.16	7,609
		4.41	3.95	7.04	4.13	37,583
250	6.61 (6.30– 6.93)	6.41	5.94	3.03	10.1	4,859
		6.14	5.64	7.11	14.7	10,045
		6.04	5.62	8.62	15.0	43,001

The damage distribution for the specimen depth H = 150 mm is shown in Figure 2.7, the other specimen depths presented a similar damage distribution. The damaging zone for ε_{eq}^{VM} is more spread out than for ε_{eq}^{MA}, the difference was around 2.5% for SEN(B) simulations. This behavior is likely due to the calculation of ε_{eq}^{VM} that is done using the strain tensor, which considers the shear stress, therefore the deformation criterion is reached in elements that would not be affected by the ε_{eq}^{MA}. It should be noted that although the damage distribution presents different, the overall response of the structure is the same in mode I.

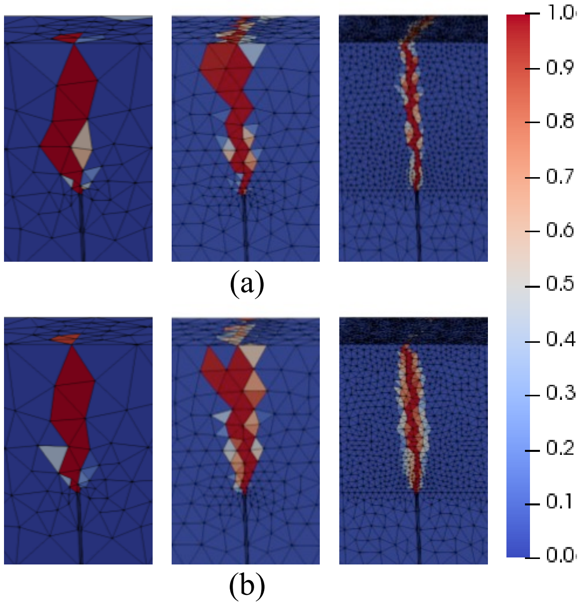

Figure 2.7 – Damage distribution for the coarse, medium, and fine mesh of the SEN(B) specimen depth H = 150 mm: (a) ε_{eq}^{MA} and (b) ε_{eq}^{VM}.

2.4.2 Size effect modeling for SEN(B) with different structural sizes

The size effect method allows graphing different specimens of different depths and P_{max} on the same figure. For this, Bažant and Planas [17] defined a nominal strength (σ_N) as a function of the P_{max}, the beam depth, and width and a coefficient representing different types of structures. The σ_N can be interpreted as the maximum nominal strength induced in a structure with a pre-existing crack to cause its unstable propagation. The P_{max} results of the simulations carried out with the SEN(B) were used to test the ability of the proposed approach to predict the size effect of structures. The methodology adopted is fllowing the size effect method of [17, 97] and the procedure can be found in [30]. A graphic comparing the influence of the structural size H on σ_N for numerical results and experimental tests is plotted in Figure 2.8. The experimental curves on the graphic represent the highest and lowest values of P_{max} for the three specimens' depth of SEN(B).

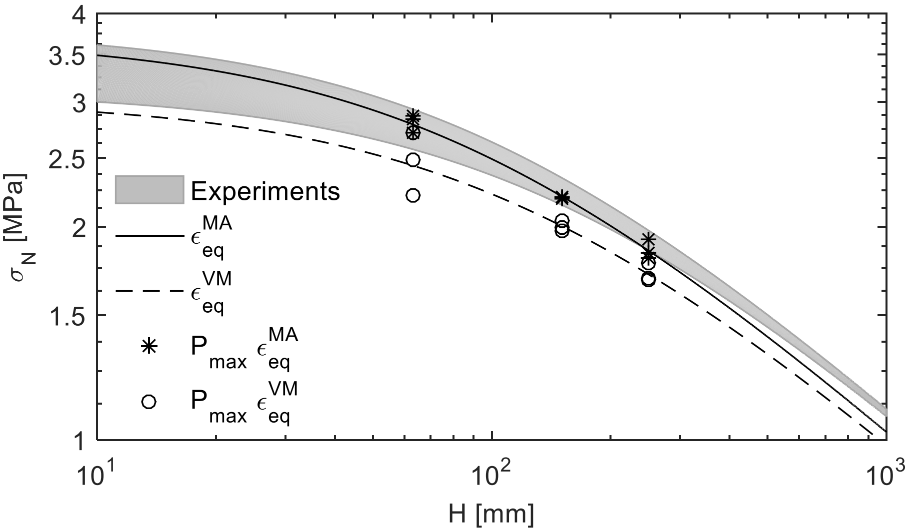

Figure 2.8 – Geometry specimen size effect for the SEN(B) specimen test with notch depth ratio of 0.33 and span depth ratio of 4.0.

Figure 2.8 shows that the proposed approach reasonably predicted the size effect of the nominal strength of the beams. The curves obtained with the simulated $\mathrm{P_{max}}$, for both $\varepsilon_{\mathrm{eq}}^{\mathrm{MA}}$ and $\varepsilon_{\mathrm{eq}}^{\mathrm{VM}}$, are within the region delimited by the curves based on experimental values. Some slight differences can be attributed to the statistical scatter of material properties, experimental results, and regression model errors [98].

2.4.3 SEN(B) simulations with the trilinear damage model

To verify the trilinear damage model, a structure made from recycled concrete aggregate with reinforced fibers presented by Evangelista Jr. *et al.* [94] was carried out. The test configuration, geometry, and boundary conditions are the same as presented in the previous section for the specimen depth $\mathrm{H} = 150$ mm. The simulations were performed with the trilinear damage model using $\varepsilon_{\mathrm{eq}}^{\mathrm{MA}}$ and $\varepsilon_{\mathrm{eq}}^{\mathrm{VM}}$ with the medium mesh. The fracture parameters adopted are $\mathrm{G_{FRC}} = 2172.0\ \mathrm{N/m}$, $\mathrm{G_F} = 78.0\ \mathrm{N/m}$,$\mathrm{G_f} = 36.0\ \mathrm{N/m}$, $\mathrm{CTOD_c} = 0.016$ mm and fiber length $\mathrm{l_b} = 40\mathrm{mm}$. The parameters related to the material are $\mathrm{E} = 28$ GPa, $\upsilon = 0{,}19$, $\mathrm{f_t} = 4.22\ \mathrm{MPa}$ and $\mathrm{K} = 10$. The author presented experimental results for the P-CMOD curves, Figure 2.9 compare them with the results obtained from the simulations.

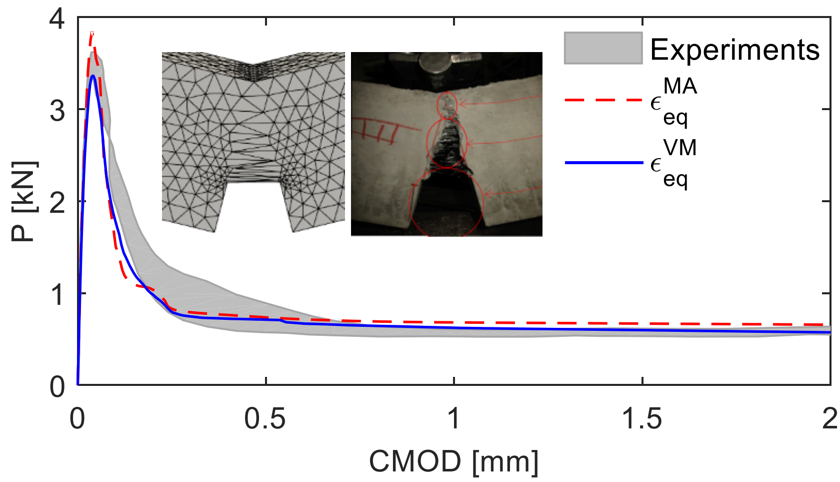

Figure 2.9 – Experimental and predicted P-CMOD curves for the SEN(B) with $\mathrm{H} = 150$ mm and the medium mesh considering the trilinear law with ε_{eq}^{MA} and ε_{eq}^{VM}.

According to the experimental results, a residual loading occurs around 15% of the P_{max} value, the figure shows that the model can capture this residual load level as well as the P_{max} for both ε_{eq}. One advantage of this model is the capacity to simulate different concrete mixtures, *i.e.*, not only plain concrete mixture with virgin aggregate (Section 2.4.1), but also recycled concrete aggregate with fiber.

2.4.4 Double-Edge-Notched Tension (DENT)

The DENT concrete specimen experimentally tested by Nooru-Mohamed [99] has been chosen to validate various techniques for fracture simulations in *quasi*-brittle materials [56, 100-102]. Numerical simulations of the DENT specimen were performed to demonstrate the capability of the proposed approach to simulate mixed-mode fracture problems. Figure 2.10 shows the geometry, boundary conditions, and the meshes used, where the geometric data are $\mathrm{L} = 200$ mm, $\mathrm{S} = 150$ mm, $\mathrm{a} = 25$ mm, $\mathrm{h} = 5$ mm, and out-of-plane thickness equal 50 mm. The test setup consists of a horizontal shear force $P_s = 10\mathrm{kN}$ that remains constant while a vertical tensile displacement δ_n is applied incrementally. The boundary and loading conditions are applied by the stiff plates attached to the four sides of the specimen (darkest mesh). Part of the material and fracture properties adopted are reported in [103]: $\mathrm{E} = 30$ GPa, $\upsilon = 0.20$, $f_t = 3.0\mathrm{MPa}$ and $G_F = 110\ \mathrm{N/m}$. The remaining properties were estimated based on monitored DENT results for vertical load and CTOD in mode I presented by [99]: $\mathrm{K} = 10$, $G_f = 40\ \mathrm{N/m}$, and $\mathrm{CTOD_C} = 0.012\mathrm{mm}$. To evaluate the convergence and mesh objectivity, the analyses are performed using a coarse, medium and fine mesh, the number of elements of each one is shown in Table 2.4. All simulations considered only the ε_{eq}^{VM}.

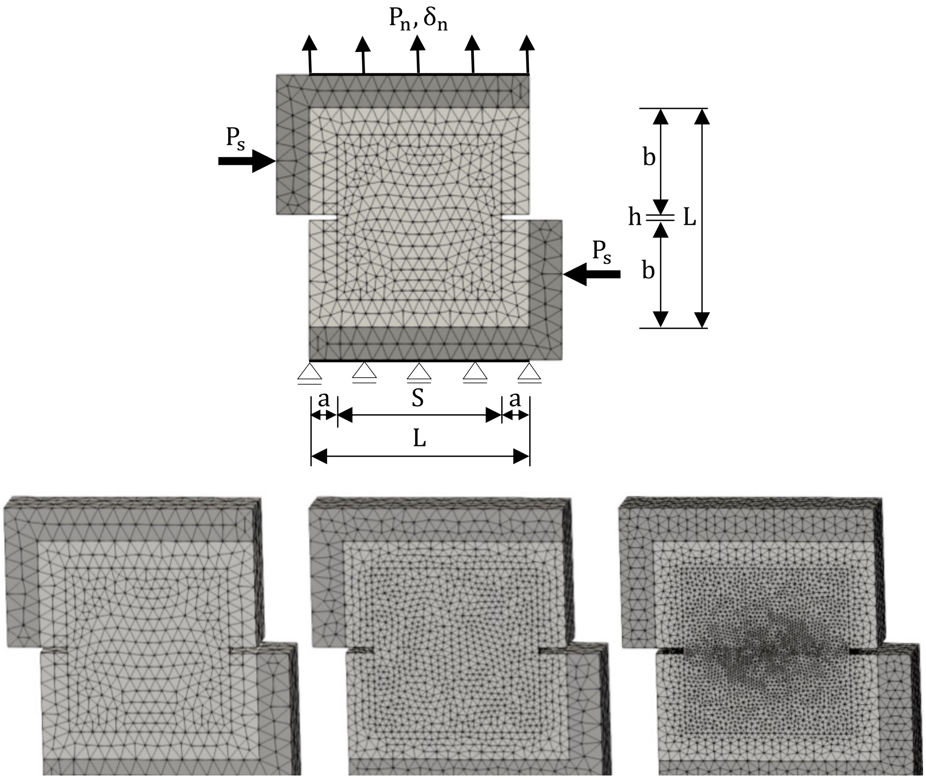

Figure 2.10 – DENT specimen: geometry, boundary conditions, and the three mesh refinements used.

Figure 2.11 show the curves obtained for vertical force P_n *versus* vertical tensile displacement δ_n: Figure 2.11a compare the numerical curves with experimental ones and with simulations from the literature; and Figure 2.11b shows that the $CTOD_C$ parameter only affects the softening part of the curves. The results have shown an overestimation of the response for P_{max} and softening, this overestimation is reported in the literature for the set of properties adopted (see the XFEM reference curve provided by [103]). Three-dimensional simulations from the literature were chosen to show the ability of the proposed approach to return good results for mixed-mode conditions with few elements in the mesh. The papers of Manzoli *et al*. [100] and Kurumatani *et al*. [56] simulated the DENT specimen in the 3D domain, the curves shown in Figure 2.11a refer to the most refined meshes used by the authors. The selected papers present similar or inferior agreement with the experimental results. The reader is encouraged to see the comparison in the respective papers of the literature.

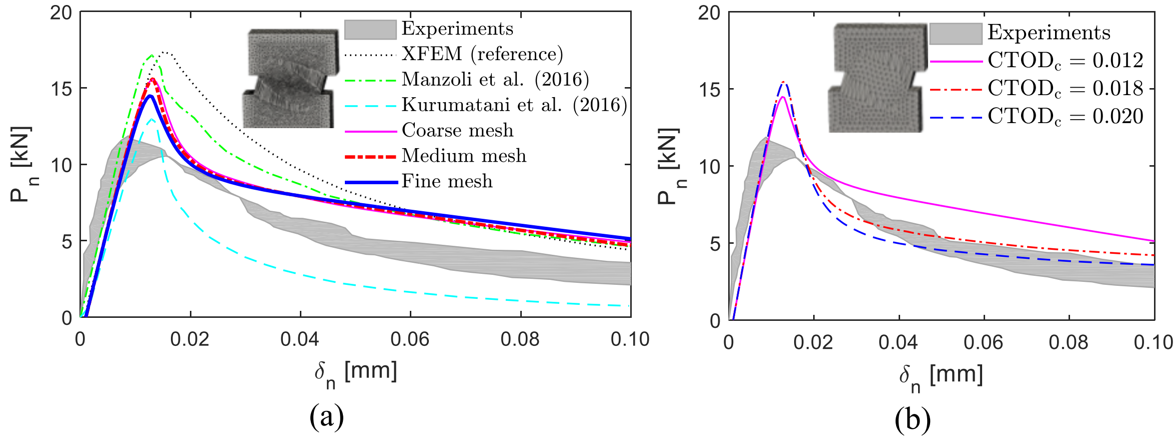

Figure 2.11 – Load *versus* displacement curve of the mixed mode DENT: (a) comparison with experimental and simulations from the literature; (b) the effect of $CTOD_C$ on the curves for the coarse mesh.

Table 2.4 compares the number of elements of the finite element mesh of the proposed strategy with the results of papers from the literature. The table shows the number of elements for 3D and different mesh strategies (coarse, medium, and fine meshes) each paper employed. Note that the proposed strategy was able to simulate the mixed-mode conditions with much fewer nodes for both coarse and fine mesh strategies even using the linear elements (4-node tetrahedron). The proposed approach does not require the insertion of special elements along the boundary of bulk elements [100] and when compared to the local continuum damage approach in [56], it uses approximately 10 times fewer elements for the coarsest meshes.

Table 2.4 – Comparison of the number of elements with other recent simulations from literature for the DENT specimen.

Reference	**coarse**	**medium**	**fine**	**model**
Manzoli *et al.* [100]	12,215^a	22,721^a	43,398^a	high aspect ratio interface element
Kurumatani *et al.* [56]	60,360^b	n/a	625,252^a	local continuum damage
Proposed strategy	5,845^a	23,167^a	75,657^a	local continuum damage

Type of element: ^{a}: tetrahedron (T4); ^{b}: hexahedron (Q8); n/a: not applicable.

The damage distribution is compared to the predicted crack propagation following a curved trajectory of the experimental crack patterns in Figure 2.12 and is in good agreement with the experimental crack patterns region. For this test, the proposed approach was able to predict the structural response of the experimental tests independently of the mesh refinement.

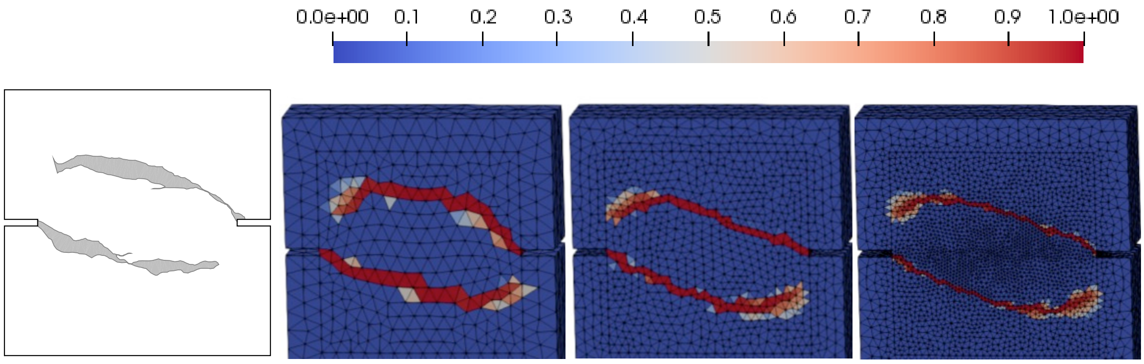

Figure 2.12 – Experimental crack patterns (adapted from [34]) and damage distribution for coarse, medium, and fine mesh.

2.4.5 Concrete slabs specimen test

Investigations of the size effect on concrete slab fatigue and overloads were performed by Roesler *et al.* [104]. The authors carried out experimental tests and presented monotonic load-displacement results for several plain concrete slabs tested on a soil foundation under mode I loading. One type of that slab ($1.80\ x\ 1.80\ x\ 0.15\ m^3$) was simulated to validate the proposed damage approach. The material and fracture properties can be found in the paper of Evangelista Jr. *et al.* [33]. The concrete fracture properties were obtained from a Disk-shaped Compact Tension (DCT) test (ASTM D7313 [105]) whose specimen was extracted from the slab itself, their values are $\mathrm{G_F} = 162\ \mathrm{N/m}$, $\mathrm{G_f} = 81\ \mathrm{N/m}$, and $\mathrm{CTOD_c} = 0.011\ \mathrm{mm}$. The concrete properties are $\mathrm{E} = 32\ \mathrm{GPa}$, $\upsilon = 0.18$, $\mathrm{f_t} = 4.95\ \mathrm{MPa}$ and $\mathrm{K} = 10$. The soil foundation was modeled as a linear elastic material under the bottom of the slab with $\mathrm{E} = 1.0\ \mathrm{MPa}$ and $\upsilon = 0.35$, these values were adopted to ensure that the numerical P-deflections curves have the same slope as the experimental ones in the pre-peak region. The loading is applied through increments of displacements at the mid-slab edge through a $0.20\ \mathrm{x}\ 0.20\ \mathrm{m^2}$ steel plate. Figure 2.13 shows the test setup indicating the materials and boundary conditions and the coarse, medium, and fine mesh refinement used to discretize the concrete slab, the number of elements is shown in Table 2.5. Simulations were performed using the equivalent strains of ε_{eq}^{MA} and ε_{eq}^{VM} for each mesh.

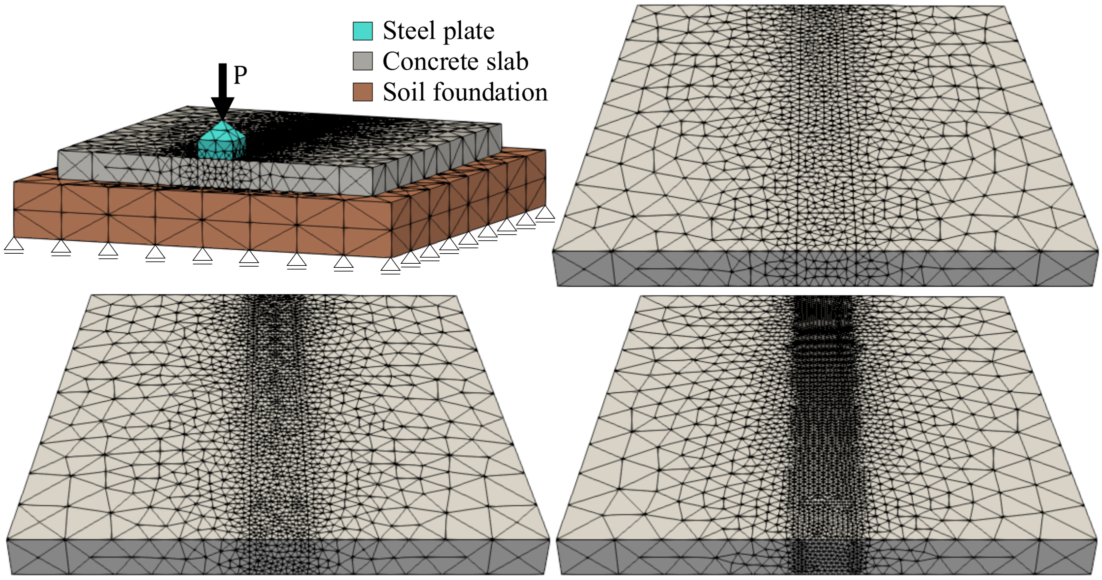

Figure 2.13 – Concrete slab specimen test setup: boundary conditions and the three mesh refinements used.

The focus is on the flexural capacity and the ability of the proposed approach to estimate this parameter for a concrete slab with mesh objectivity. Table 2.5 shows the P_{max} values from the simulations and compare them with the mean value of the experimental range and numerical results of [33]. When the ε_{eq}^{MA} was used, the relative difference was less than 7%, with P_{max} below the mean and within the experimental range. For ε_{eq}^{VM}, the coarse mesh presented an overestimation of the P_{max}, which is improved with the most refined meshes. The results presented in Table 2.5 demonstrate the advantages observed in the case of the DENT specimen: the proposed approach presents mesh objectivity and good results with few elements in the mesh and does not require the insertion of special elements along the boundary of bulk elements, when compared to the simulations of [33], approximately 26 times fewer elements were needed for the coarser mesh to provide similar accuracy.

Table 2.5 – Comparison of the P_{max} and the number of elements with experimental and simulation from the literature for concrete slab specimens.

Reference	P_{max} [kN]		Rel. Diff. [%]		N_{elem}	Model
Experiments [104]	mean (range) 110 (103–122)		n/a		n/a	n/a
Abaqus [33]	126		14.5		363,931[a]	C3D8R interface element
Evangelista Jr. et al. [33]	109		0.90		363,931[a]	cohesive interface element
Proposed	ε_{eq}^{MA}	ε_{eq}^{VM}	ε_{eq}^{MA}	ε_{eq}^{VM}		
Coarse mesh	108	138	1.82	25.4	14,115[a]	local continuum damage
Medium mesh	104	122	5.45	10.9	28,225[a]	
Fine mesh	103	121	6.36	10.0	62,365[a]	

Type of element: [a]: tetrahedron (T4); n/a: not applicable.

The load-deflection *versus* vertical slab displacement curves were obtained with ε_{eq}^{MA} and ε_{eq}^{VM}, and are compared to experimental results in Figure 2.14, which also shows the simulations result of [33]. The experimental curves revealed some stages of the slab response: an initial linear elastic response; a nonlinear behavior until peak load; a specimen softening due to final crack growth until a local minimum was reached; and an increase in the load capacity due to the soil's linear elastic response. The test setup and the strategy adopted to solve the nonlinear equation system (*i.e.*, the secant method) were able to represent the first two stages but did not completely represent the increase after the great loss of load capacity. It is important to point out that these limitations are not directly associated with the damage approach, but rather with the secant method and the fact that the soil foundation was discretized under the bottom of the slab, while in [33] it was modeled with linear springs distributed under the bottom of the slab. Authors like [95, 106] have reported the occurrence of phenomena such as lack of convergence, instability problems, and snap-backs, even with the use of more powerful tools for solving nonlinear problems. All simulations were stopped due to one of these phenomena, *i.e.*, the lack of convergence.

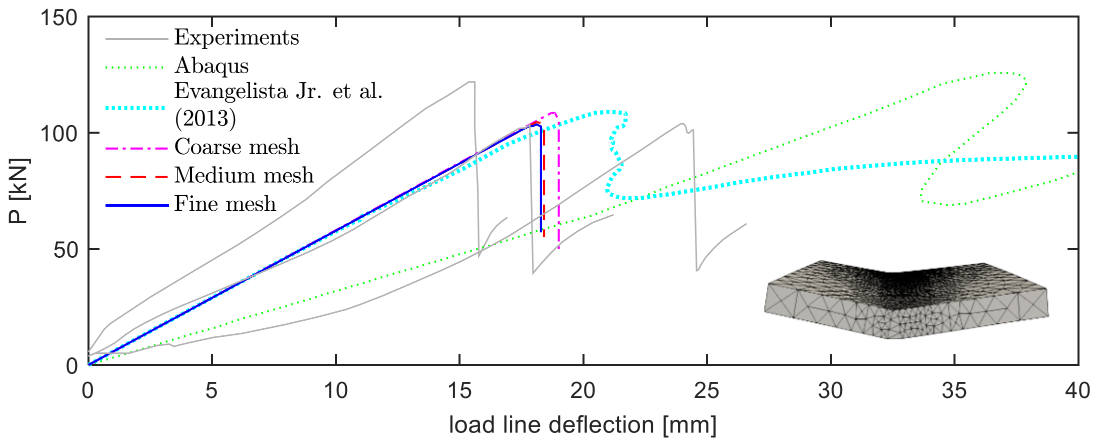

(a)

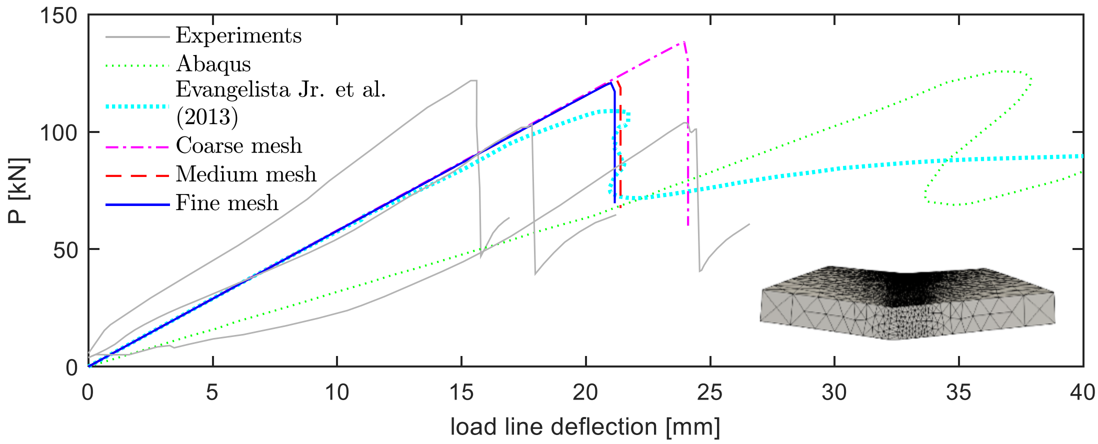

(b)

Figure 2.14 – Load *versus* deflection curves of the concrete slab specimen: (a) ε_{eq}^{MA} and (b) ε_{eq}^{VM}. Comparison with experimental and simulations from the literature.

The slab damage contour was plotted in Figure 2.15 for different stages on the load *versus* displacement curve, the damage is concentrated on the ligament area at the center of the slab. The points of interest were chosen to represent different stages of the load/displacement response: at stage (i) the loading is around 90% of the P_{max} in the pre-peak region and shows the first damaged elements; at stage (ii) the P_{max} is achieved, but less than 50% of the ligament area is damaged; damage propagation in the remaining ligament area increases dramatically during the softening curve until the load reaches stage (iii) at the post P_{max}; from this stage onwards the load increases again being absorbed by the soil, which deforms vertically (not shown in the graphic). For each stage, the damaged region was similar in all meshes, but with the ε_{eq}^{VM} more elements were damaged, a fact also observed in the case of SEN(B). As expected, the damage propagation is similar to the crack propagation, with a simultaneous progression across and up through the slab depth with increasing load/displacement level.

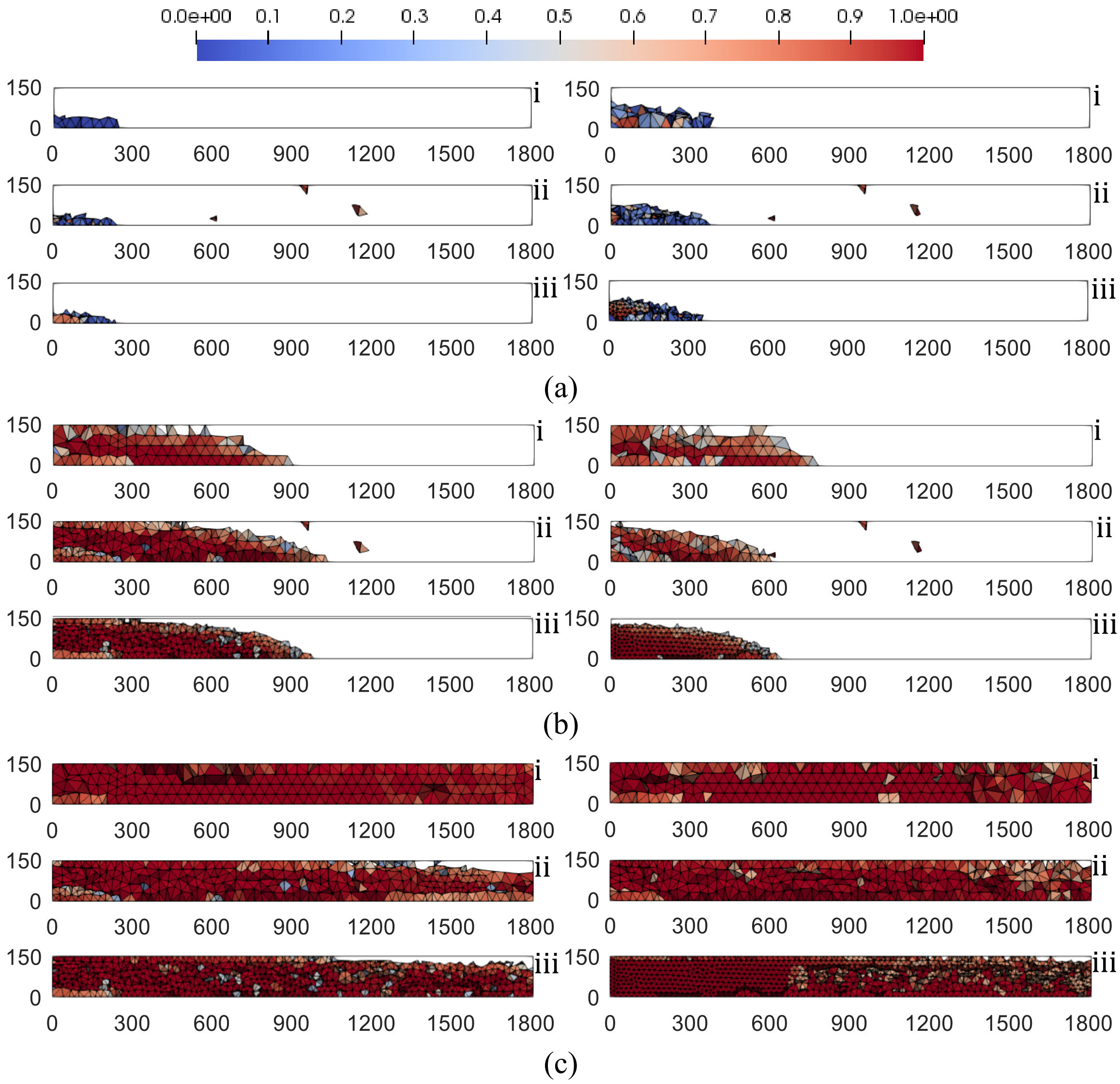

Figure 2.15 – Damage distribution of the concrete slab specimen for coarse (i), medium (ii), and fine (iii) mesh at the points of interest: (a) 90% of P_{max}, (b) P_{max} and (c) post P_{max}. To the left ε_{eq}^{MA} and to the right ε_{eq}^{VM}. The damage is located in the center of the slab.

2.4.6 Real scale problem: Koyna dam

The Koyna dam in India is a reference structure for static fracture simulation with mixed mode propagation. In this structure, a notch is created from which a crack propagates due to the overflow of water at the crest of the dam. Its static analysis was studied by several researchers with the application of different methods for crack/damage propagation through the overflow. Gioia *et al.* [107] performed numerical studies using linear fracture mechanics and plasticity models. Roth *et al.* [74] combined an anisotropic continuous damage model with the G/XFEM. Wu *et al.* [108] developed a phase-field regularized cohesive zone model for modeling localized cracks. None of these works simulated the dam by a damage model with bilinear softening law and local energy dissipation controlled by the regularization of fracture energy and element length.

Figure 2.16 shows the geometry, boundary conditions, and the meshes used, where the geometric data are $L = 70$ m, $h = 103$ m, $d = 36.5$ mm, $b = 19.3$ m, $a = 14.8$ m, and thickness of 1.0 m. The notch has a length of 1.93 m and is located on upstream of the dam, equivalent to 10% of the width b in the direction of the kink point on downstream of the dam. According to [107], the crack located at this point results in the most critical behavior. The body forces and hydrostatic pressure of the filled reservoir are fully applied and the overflow load is applied incrementally, through a constant pressure, with the water pressure inside the crack neglected. The material and fracture parameters for carrying out the simulations were taken from [74, 108]: $E = 32$ GPa, $\nu = 0{,}2$, $f_t = 1$ MPa, $f_c = 10$ MPa $G_f = 35$ N/m, $G_F = 100$ N/m. No data related to $CTOD_c$ was found in any of the referenced papers, so the adopted value was 0.0525mm, which results in a kink point $\Psi_1 = 0.25$. The properties related to external loads are the mass density of concrete $\rho_c = 2450\ \mathrm{kgf/m^3}$, mass density of water $\rho_a = 1000\ \mathrm{kgf/m^3}$ and gravity acceleration $g = 9.81\ \mathrm{m/s^2}$. Simulations were carried out in the plane strain state for two mesh refinements of triangular (T3) elements using the ε_{eq}^{VM}. Figure 2.16 shows the coarse mesh with 844 elements and the fine mesh with 8474 elements.

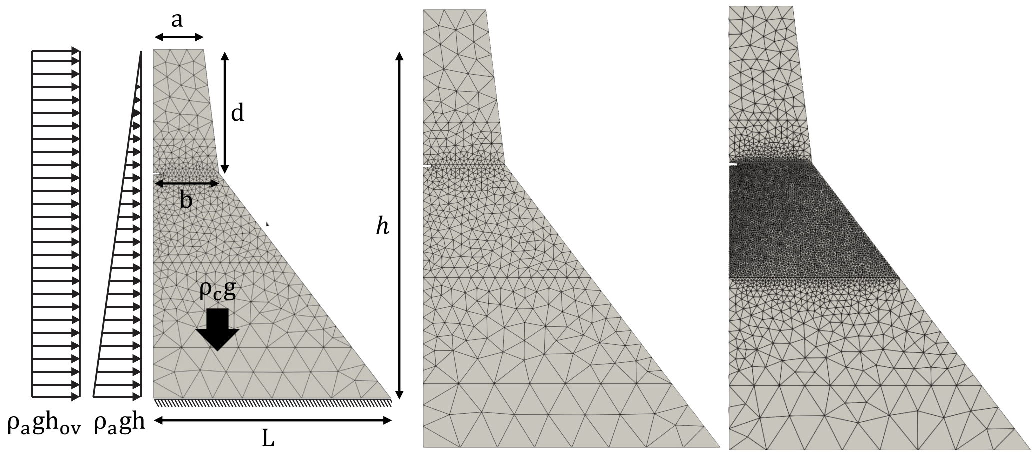

Figure 2.16 – Geometry, loading, and boundary conditions of the Koyna dam and the two mesh refinements used.

The numerical curves of overflow height (h_{ov}) *versus* crest horizontal (δ_{hc}) displacement of the dam structure obtained from the proposed damage strategy are shown in Figure 2.17. Furthermore, simulated curves from the work of Gioia *et al.* [107], which used a finite element mesh with 224 quadrilateral elements (Q8), Roth *et al.* [74], who used a mesh with

4320 quadrilateral elements (Q4), and Wu *et al.* [108], that did not inform the quantities or the type of finite element used in their meshes. As can be seen, the graph shows that the simulations with the proposed model resulted in curves similar to those found in the literature, although with greater rigidity, and that there is no significant difference between the curves for the coarse and refined mesh, which confirms the objectivity of the mesh.

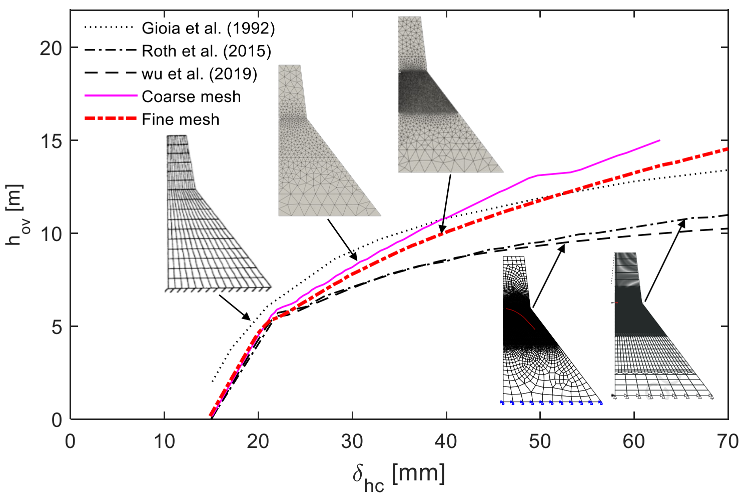

Figure 2.17 – Numerical curves of h_{ov} versus δ_{hc} of the concrete Koyna dam. Comparison with simulation from the literature.

Damage distributions of the Koyna dam simulations are shown in the figure below for coarse and fine mesh and are compared with the results from [108]. From the figure it is possible to observe that the proposed damage strategy was able to reproduce the crack branching due to the complex stresses around the intersecting point where the downstream face changes its slope, this crack pattern is fairly close to that found in the literature in the work of [108].

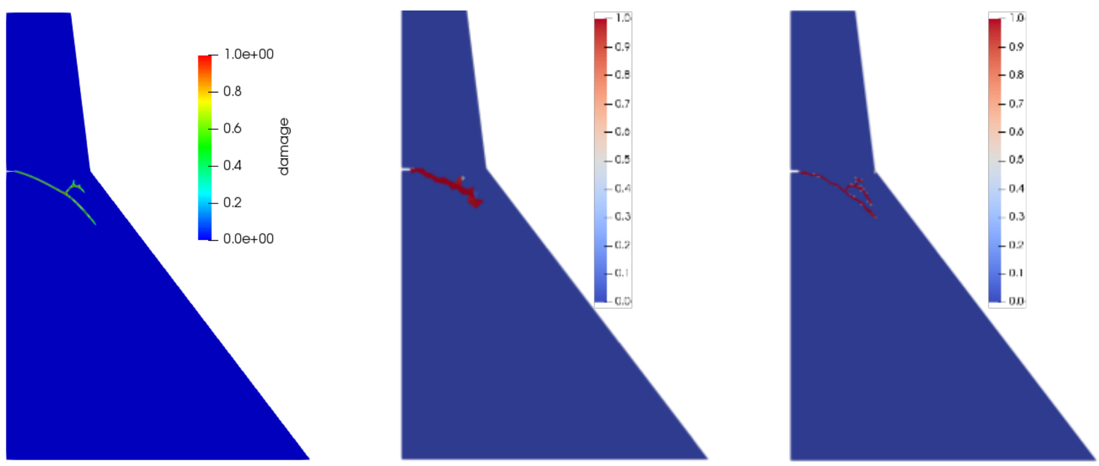

(a) (b) (c)

Figure 2.18 – Damage distribution for the concrete Koyna dam of (a) Wu *et al.* [108]; (b) coarse mesh and (c) fine mesh.

2.5 PARTIAL CONCLUSIONS

This chapter has formulated and implemented through the thermodynamics of irreversible processes framework a novel three-dimensional damage approach based on damage mechanics and fracture laws for damage evolution for modes I and mixed (I+II) conditions able to predict failures in structures of *quasi*-brittle materials. The damage evolution law is based only on strength (tensile strength) and fracture properties (critical energy release rate, total fracture energy, and critical crack tip displacement) commonly determined in standard fracture tests. No further calibration of material or analysis parameters needed to be performed. The approach was validated by comparison with experimental and numerical results for several types of tests and failure modes: three-point bending in a single-edge notch beam, double-edge-notched tension specimen, and a concrete slab on a soil foundation. The damage model was demonstrated to be mesh-objective and mesh-independent, and the comparison with the experimental results demonstrated the capabilities of the model in predicting the behavior of rupture of structure submitted to failures in mode I and mixed mode, failures of different structural sizes to predict the size effect of geometrically similar structures and failure of a smooth surface (unnotched specimens).

In all numerical simulations, the proposed damage model was able to reproduce/predict, with good agreement, the maximum load P_{max} and the entire softening behavior observed in the experimental tests. The proposed strategy for the local energy dissipation controlled by the regularization of fracture energy and element length ensured that different mesh densities dissipated the same specific energy during the damage evolution. Regarding the different equivalent deformations, the mode I predict of P_{max} and the softening behavior using the ε_{eq}^{VM} were as good as the predictions with the ε_{eq}^{MA} that is idealized specifically for this failure mode. This shows that ε_{eq}^{VM} can be used for problems in pure mode I and mixed. Especially in the mixed mode simulations, ε_{eq}^{VM} proved to be quite efficient in predicting the distribution of the damage in regions equivalent to the location of cracks in experimental tests.

The proposed approach outperformed recent results from the literature, especially for the concrete slab specimen, which obtained a good agreement with the experimental curves with relatively coarse meshes than other models of literature. Therefore, it confirmed the efficiency of the proposed model to reduce the computational cost with relative coarse meshes and no expensive non-local algorithm.

3 IMPLEMENTATION OF THE PPR COHESIVE ZONE MODEL IN THE GENERALIZED FINITE ELEMENT METHOD FRAMEWORK

In this chapter, it was implemented the cohesive law of Park-Paulino-Roesler (PPR) [109], and the bilinear [87] and exponential [13] laws into the Generalized/eXtended Finite Element Method (G/XFEM) framework to predict the mode I and mixed (I+II) mode of fracture behavior in structures of *quasi*-brittle materials. The implementation was done for two and three-dimensional domains. The originality lies in the fact that no paper has combined the advantages of G/XFEM with the PPR law from the Cohesive Zone Model (CZM) to simulate mixed-mode fracture problems. Benchmark problems from the literature are used to test the efficiency and accuracy of the strategy of allying the cohesive laws with the G/XFEM. An unnotched beam in a three-point bending (mode I) and a mixed mode delamination test with an analytical solution are carried out to validate the implementation. The efficiency and accuracy are tested for a coarse and a fine mesh with the splitting tensile strength specimen (mode I), a single edge notch beam in a three-point bending (mode I), and a single edge notch beam in a four-point shear (mixed mode). The strategy has proved to be able to numerically simulate the strength and softening behavior of structural members under various modes of failure in an efficient manner for two and three-dimensional domains. The good agreement of the results obtained in comparison with experimental curves, analytical solutions, and numerical results of benchmark paper found in the literature demonstrates the efficiency and accuracy of the strategy.

3.1 INTRODUCTION

The nonlinear behavior of *quasi*-brittle materials such as concrete has been the focus of many researchers. This nonlinear behavior is linked to a Fracture Process Zone (FPZ) ahead of the crack tip where the energy dissipation takes place. In *quasi*-brittle materials, the FPZ size is large compared to the crack length and characteristic size of the structure, its characteristics have been widely studied in the literature using fracture mechanics. The fracture mechanics deal with discontinuities caused by the formation and growth of a macro-crack, a very useful idealization to modeling discrete crack propagation in *quasi*-brittle materials is the CZM, initially introduced by Barenblatt [4, 5] and Dugdale [6], to address the crack tip singularities. In the CZM, all nonlinearities are located in a cohesive zone ahead of the crack tip that relates to the fracture process zone, *i.e.*, to the region where the energy dissipation occurs during the fracture process. The pioneering work of Hillerborg *et al.* [13] applied the CZM concepts to overcome some limitations of the elastic linear fracture mechanics using the finite element method to investigate the fracture behavior in the concrete, his model is known as the fictitious crack model. In the following years, this methodology was widely used for concrete crack simulation [17, 27-29].

In CZM, the fracture behavior can be characterized as either nonpotential-based models or potential-based models to obtain the traction-separation relationship over the fracture. In the case of potential-based models, cohesive tractions can be deduced from the first derivative of the potential concerning the crack opening displacement and the second derivative provides the tangent modulus of the material. In the literature, several CZMs are defined based on a potential function, such as those found by [110-112]. Xu and Needleman [113] proposed a potential in which the normal and tangential separation is described through exponential functions. In the paper of Park and Paulino [114], the authors present a critical review of the traction-separation relationships in the field of the CZM, especially in cases formulated by a potential-based model.

Roesler *et al.* [87] and Park *et al.* [32] respectively proposed a nonpotential-based CZM with a bilinear softening curve for plain concrete and a trilinear softening curve for fiber-reinforced concrete, later Park *et al.* [31] related the first kink point of the curve with the critical Crack Tip Opening Displacement (CTODc). The main advantage of these bilinear and trilinear models is that the entire softening curve is physically defined by properties determined from standard fracture specimens and no curve fitting is needed to define the specimen response curve. Both models have been successfully used for fracture prediction in concrete materials with different boundary conditions by the use of a cohesive inserted in the finite element mesh [33, 95, 106, 115-117]. Here, the bilinear law of [87] is used to simulate problems in mode I of fracture and compared to the results of other cohesive models.

Park *et al.* [109] proposed a constitutive CZM by a polynomial potential-based that can be applied to mode I and mixed mode (I + II) of fracture, the authors named it the PPR model and presented it in both extrinsic and intrinsic versions. The potential is defined by physical parameters such as fracture energy, resistance parameters (tensile strength, yield stress), and shape parameters that characterize the softening response of the material. The intrinsic version still requires initial slope indicators to control elastic behavior and this renders the extrinsic version more advantageous. The model was first implemented by Park *et al.* [118] in a finite element framework by the insertion of a two-dimensional linear cohesive element into a regular mesh and [119, 120] generalized it to three dimensions in the same bases of [118]. Simulations performed showed a good agreement with analytical solutions and can count the nucleation and propagation in adhesives, composites, line pipe steel, and microstructures analyses.

Cohesive elements governed by the PPR traction separation law were used to investigate the influence of interphases on the large deformation response of particle-reinforced composites [121]. In the paper [122], the authors demonstrated that the PPR model is not thermodynamically consistent for various unloading/reloading relations which have been proposed for use with the model, and in [123] the combination of a linear unloading/reloading relationship with the PPR model showed a strong dependence on the path followed during unloading. Recent publishers employed the PPR model to model the propagation of hydraulically induced fracture by a pore pressure cohesive element [124] and a FEM-LB coupling applied to geomaterials of complex geometries [125], their simulations with a series of single-element tests showed good compliance with the experimental results and analytical curves solution.

The main feature of the CZM model cited above is that they simulate the crack by using interface elements inserted in between the bulk elements. This approach enables explicit crack modeling and avoids spurious stress transfer between the crack faces. One disadvantage is the cohesive crack element must be inserted along the crack surface for both intrinsic and extrinsic approaches. Furthermore, significant mesh refinement is required at critical regions (stress concentration zones) to have model convergence and experimental agreement. To overcome this advantage, there are several numerical methods developed in the literature to model fracture problems using the CZM, including the boundary element method, the meshless method, and the G/XFEM. This last one takes advantage of the partition of unity methods where the standard approximation basis of the finite element method can be locally enriched with special functions that can approximate discontinuous or singular fields. These new numerical methods can simulate arbitrary crack surfaces without the requirement to propagate cracks along pre-defined or element boundaries.

GFEM has its origins in Babuška *et al* [126], Duarte and Oden [127], Duarte [128], Duarte and Oden [129], and Melenk and Babuška [130]. Babuška *et al.* referred to the method as the "special finite element method, generalized finite element method" and "finite element partition of unity". In Duarte and Oden's work the method is called the "hp-clouds and cloud-based hp finite element method". On the other hand, the term eXtended Finite Element Method (XFEM) was introduced by Belytschko and colleagues [131-137]. The first paper to treat the CZM in the G/XFEM framework was that of Wells and Sluys [138]. The authors represented the displacement jump through the entire crack including the crack tip by the Heaviside function alone and the traction-separation relationship adopted was the exponential discrete constitutive model. Since then, various applications of cohesive crack have been proposed in the literature. One can cite the simulation of *quasi*-static cohesive crack propagation in *quasi*-brittle materials performed by [139]. One can also mention the modeling of cohesive crack growth in concrete structures that use an adaptive crack growth algorithm [140], energy-based modeling of cohesive and cohesionless cracks [141], analytical enrichment [142], and higher-order enrichment [143]. All are applied to the two-dimensional analysis. In the literature, there are some papers dealing with cohesive crack modeling with G/XFEM in a three-dimensional domain [144-147].

The PPR model has been rarely used to simulate cohesive problems of crack growth, the works mentioned above are the only ones and have no work that simulates benchmark experimental tests of a mixed mode of fracture with this model. Kim and Duarte's [146] paper is the only one so far that combines the advantages of G/XFEM with the PPR law to simulate crack growth, however, the authors performed no benchmark problems in mixed modes failure. Simulation of such problems with the PPR model has been difficult because the tangential parameters are generally not available in the literature. Therefore, in this work was implemented the extrinsic PPR cohesive model into the G/XFEM framework in a two-dimensional domain. Exponential and bilinear cohesive laws are also implemented to compare with PPR for mode I. Crack tip enrichment by a branch function is adopted to improve the response of coarse meshes. The main objective is to test the PPR model in mixed mode benchmark problems by adopting various combinations of the tangential parameter as a function of resistance and fracture properties to detect the one that best describes physically the *quasi*-brittle fracture. In addition, mesh size independence is verified and the interference of the branch function exponent is investigated in the global response of the tests.

An outline of the rest of the chapter is as follows. Section 3.2 presents in a simplified way the G/XFEM methodology and how cohesive models are incorporated into it. This section further describes details about crack tip enrichment. Section 3.3 describes the cohesive constitutive PPR law, as well as exponential and bilinear laws implemented to characterize the softening behavior of *quasi*-brittle materials. In Section 3.4, numerical implementation issues such as the node enrichment process and the integration procedure for the elements crossed by crack and/or enriched with the branch function are addressed. Sections 3.5 and 3.6 are showed the results of the numerical simulations for mode I and mixed, respectively. The tests in mode I are used to validate the implementation of the PPR model by comparing their response with the exponential and bilinear laws.

3.2 GENERALIZED/EXTENDED FINITE ELEMENT METHOD (G/XFEM)

The G/XFEM is based on the principle of Partition of Unity and consists in enhance the traditional shape functions of finite elements with other so-called enrichment functions that represent the local behavior of the solution. For the case of discontinuity, the enrichment function can be found from the kinematics of the displacement jump [138, 148] and the method is usually called eXtended Finite Element Method (XFEM). The displacement field $\boldsymbol{u}$ for an element can be interpolated by Equation (3.11a), with $\boldsymbol{\mathcal{H}}_{\Gamma_d}$ being the Heaviside function centered at discontinuity Γ_d and the displacement jump $[\![\boldsymbol{u}]\!]$ in Γ_d given by Equation (3.1b).

$$\begin{aligned} \mathbf{u} &= \mathbf{Na} + \boldsymbol{\mathcal{H}}_{\Gamma_\mathrm{d}}\mathbf{Nb} \\ [\![\mathbf{u}]\!] &= \mathbf{Nb}|_{\Gamma_\mathrm{d}} \end{aligned} \tag{3.1a,b}$$

in which $\mathbf{a}$ and $\mathbf{b}$ are the regular and enhanced degrees of freedom, respectively. The construction of the G/XFEM shape function for this case is shown in Figure 3.1, where x is a node shared by four rectangular elements as illustrated at the bottom of the figure. The function at the top is a standard linear finite element shape function $\mathbf{N}$, in the middle is shown the discontinuous enrichment functions $\boldsymbol{\mathcal{H}}\mathbf{N}$, and at the bottom is shown the resulting generalized finite element shape function $\boldsymbol{\phi}$.

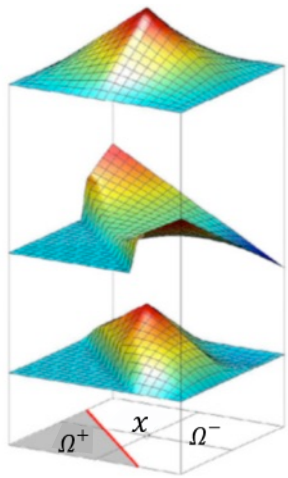

Figure 3.1 – G/XFEM shape function construction for discontinuous high-order enrichments (adapted from Evangelista Jr. *et al*. [149])

The equilibrium equations for a body Ω (Figure 3.2) crossed by a discontinuity Γ_d, disregarding body forces, can be summarized in Equation (3.2a-c), and the essential boundary conditions are given by Equation (3.2d)

$$\begin{aligned}
\nabla\boldsymbol{\sigma} &= 0 \text{ in } \Omega \\
\boldsymbol{\sigma}\mathbf{n} &= \bar{\mathbf{t}} \text{ in } \Gamma_\mathrm{t} \\
\boldsymbol{\sigma}\mathbf{n}_\mathbf{d} &= \mathbf{t} \text{ in } \Gamma_\mathrm{d} \\
\mathbf{u} &= \bar{\mathbf{u}} \text{ in } \Gamma_\mathrm{u}
\end{aligned} \tag{3.2a-d}$$

in which $\boldsymbol{\sigma}$ is the Cauchy stress tensor, $\mathbf{n}$ is the unit normal vector to the surface of Ω, $\bar{\mathbf{t}}$ is the tractions prescribed on Γ_t, $\mathbf{t}$ is the tractions acting at Γ_d, $\bar{\mathbf{u}}$ is a prescribed displacement on Γ_u and $\mathbf{n}_\mathbf{d}$ is the unit normal vector to the discontinuity (pointing to $+\,\Omega$).

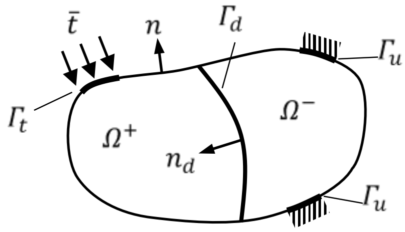

Figure 3.2 – Body Ω crossed by a discontinuity Γ_d.

For the constitutive relations, the tractions for the continuum domain are expressed in terms of the nodal displacements, and the discontinuity stresses are expressed in terms of the additional nodal displacements, according to:

$$\begin{aligned}\boldsymbol{\sigma} &= \mathbf{D}_0\boldsymbol{\varepsilon} = \mathbf{D}_0(\mathbf{Ba} + \mathcal{H}\mathbf{Bb}) \\ \mathbf{t} &= \mathbf{T}[\![\mathbf{u}]\!] = \mathbf{TNb}\end{aligned} \tag{3.3a,b}$$

in which $\mathbf{D}_0$ is the finite element constitutive matrix for the undamaged state, $\mathbf{T}$ relates traction and displacement rates at the crack and $\mathbf{B}$ is a matrix containing derivatives of shape functions. In cohesive zone models, the relation $\mathbf{T}[\![\mathbf{u}]\!]$ is described by a constitutive model expressed in traction versus crack opening curve that allows the simulation of the process zone by applying tractions to the opening plane depending on the crack opening value. In 2D simulations, the matrix $\mathbf{T}[\![\mathbf{u}]\!]$ has two terms in their main diagonal, the first term is the normal traction-displacements ($\mathrm{T_n}$) and the second term is the tangential traction-displacements ($\mathrm{T_t}$). The secondary diagonal is set to zero. The constitutive model implemented in this work is detailed in the cohesive zone model section.

The linearized weak form of the governing equations reads

$$\begin{bmatrix}\mathbf{K_{aa}} & \mathbf{K_{ab}} \\ \mathbf{K_{ba}} & \mathbf{K_{bb}}\end{bmatrix}\begin{bmatrix}\boldsymbol{\delta}_\mathbf{a} \\ \boldsymbol{\delta}_\mathbf{b}\end{bmatrix} = \begin{bmatrix}\mathbf{f_{ext,a}} \\ 0\end{bmatrix} - \begin{bmatrix}\mathbf{f_{int,a}} \\ \mathbf{f_{int,b}}\end{bmatrix} \tag{3.4}$$

in which:

$$\begin{aligned}
\mathbf{K_{aa}} &= \int_\Omega \mathbf{B^T D_0 B}\,d\Omega \\
\mathbf{K_{ab}} &= \int_{\Omega^+} \mathbf{B^T D_0 B}\,d\Omega \\
\mathbf{K_{ba}} &= \mathbf{K_{ab}}^\mathbf{T} = \int_{\Omega^+} \mathbf{B^T D_0 B}\,d\Omega \\
\mathbf{K_{bb}} &= \int_{\Omega^+} \mathbf{B^T D_0 B}\,d\Omega + \int_{\Gamma_d} \mathbf{N^T T N}\,d\Gamma \\
\mathbf{f_{int,a}} &= \int_\Omega \mathbf{B^T}\boldsymbol{\sigma}\,d\Omega \text{ and } \mathbf{f_{ext,a}} = \int_{\Gamma_t} \mathbf{N^T}\bar{\mathbf{t}}\,d\Gamma \\
\mathbf{f_{int,b}} &= \int_{\Omega^+} \mathbf{B^T}\boldsymbol{\sigma}\,d\Omega + \int_{\Gamma_d} \mathbf{N^T t}\,d\Gamma
\end{aligned} \tag{3.5a-f}$$

in which $\boldsymbol{\delta}_\mathbf{a}$ and $\boldsymbol{\delta}_\mathbf{b}$ are the standard and enriched degree of freedom of the G/XFEM framework, respectively.

For the cohesive fracture problems described only with the enrichment across a crack surface, it is usually necessary to a mesh with a large number of finite elements in the fracture process zone to return satisfactory results for a mixed mode of fracture. This is caused by a lack of precision in the crack tip fields, which compromises the crack propagation. To improve these crack tip fields and consequently the global response of cohesive fracture problems in which the computational discretization is performed with a coarse mesh, a branch enrichment function is used to model the crack front. This function is necessary to guarantee that the stress at the tip does not become singular. As proposed by Belytschko *et al.* [134] and Moës and Belytschko [75] to simulate cohesive crack growth, the following branch function is used to enrich around the crack tip:

$$F_{tip}(r, \theta) = r^{k} \sin\frac{\theta}{2} \tag{3.6}$$

with k being either 1.0, 1.5, or 2.0. But in this work, the simulation was carried out with k being 0.5, 1.0, and 1.5 to test the case where k causes a singularity. With the crack tip enrichment by the branch function in the previous equation, the complete displacement field is expressed according to Moës *et al.* [131]:

$$\mathbf{u} = \mathbf{Na} + \boldsymbol{\mathcal{H}}_{\Gamma_d}\mathbf{Nb} + F_{tip}\mathbf{Nc} \tag{3.7}$$

in which $\mathbf{c}$ is a vector containing the extra degree of freedom related to crack tip enrichment.

3.3 COHESIVE ZONE MODEL (CZM)

The CZM is one of the first methods to deal with discrete crack propagation in several types of materials. To characterize the CZM, it is necessary to define a cohesive constitutive model expressed in traction *versus* crack opening curve that describes the shape of the softening curve of the material. This concept is based on the fictitious crack model of Hillerborg *et al.* [13], in which the inelastic tensions that occur in the fracture process zone ahead of the traction-free macrocrack are idealized as a line (in the case of a 2D analysis) or a surface (in 3D case). In the G/XFEM approach, the cohesive constitutive model of an element crossed by a crack is defined onto an orthogonal local coordinate system, where the normal and tangential direction to the discontinuity is represented by the vectors $\mathbf{n}$ and $\mathbf{t}$, respectively. In the rest of the non-cracked domain, the material is considered as linear elastic. In this section, three cohesive constitutive laws were described: the exponential law and bilinear law for mode I of fracture, and the latest extrinsic Park-Paulino-Roesler law for modes I and mixed cases.

3.3.1 Exponential law

The exponential cohesive constitutive model was successfully implemented in the G/XFEM framework by [138, 144, 148, 150]. The model implemented here considers that the damage in the fracture zone only evolves in mode I of fracture. Then, only the normal traction-separation law (t_n) at the crack is necessary to describe the traction-separation relationship. Such relation is defined as an exponential decrease in the function of a history parameter of the crack separation:

$$t_n = f_t \exp\left(-\frac{f_t}{G_F}[\![\Delta]\!]_n\right) \tag{3.8}$$

in which f_t is the tensile strength, G_F is the fracture energy and $[\![\Delta]\!]_n$ is the largest value of the normal separation reached at the interface. The tangential traction-separation (t_t) is set to be zero (there is no tangential traction in mode I of fracture).

Because of the applied constitutive law at discontinuity, the system of equations becomes nonlinear and has to be solved iteratively. The secant iterative procedure is adopted to capture the nonlinear behavior. The normal traction-displacements part of matrix **T** of the Equation (3.3b) is defined as:

$$T_n = \frac{f_t}{[\![\Delta]\!]_n} \exp\left(-\frac{f_t}{G_F}[\![\Delta]\!]_n\right) \tag{3.9}$$

3.3.2 Bilinear law

The bilinear model implemented here was proposed in the papers of Roesler *et al.* [87] and Park *et al.* [109] for plain concrete. The advantage of this model is that the entire softening curve is physically defined by properties determined from standard fracture specimens and no curve fitting is needed to define the specimen response curve. To determine the softening curve of the bilinear model it is necessary to define the constants δ_1, ψ and δ_f, see Figure 3.3. These constants are obtained through resistance and fracture parameters: the tensile strength (f_t), Crack Tip Opening Displacement ($CTOD_C$), initial fracture energy (G_f), and total fracture energy (G_F). The normal tractiondisplacement (δ_1) is obtained by making the G_f equal to the area within the triangle formed by the coordinate axes and the first descending straight of the softening curve (darker area in Figure 3.3). The ordinate of the kink point (ψ)

is calculated according to Park et al. [31]. The maximum opening displacement (δ_f) is obtained by equalizing the G_F with the area under the bilinear softening curve.

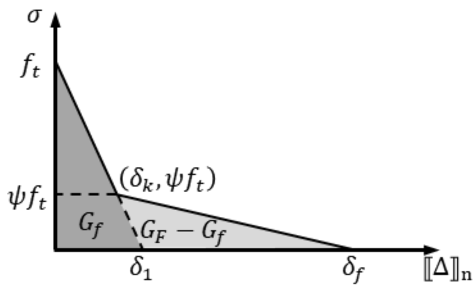

Figure 3.3 – Bilinear model: Traction-displacement curve.

Thus, the normal traction-separation relationship in the function of the history parameter of the normal crack separation ($[\![\Delta]\!]_n$) for the bilinear model is defined as:

$$t_n = \begin{cases} -\dfrac{f_t}{\Delta_1}([\![\Delta]\!]_n - \delta_1) & \text{if } (0 < [\![\Delta]\!]_n < \delta_k) \\ -\dfrac{\psi f_t}{\delta_f - \delta_k}([\![\Delta]\!]_n - \delta_f) & \text{if } (\delta_k \le [\![\Delta]\!]_n < \delta_f) \\ 0 & \text{if } ([\![\Delta]\!]_n \ge \delta_f) \end{cases} \tag{3.10}$$

Again, the tangential part of the traction-separation relationship is set to zero because no mixed modes of fracture are simulated here with the bilinear model. Finally, the normal term T_n of the matrix **T** is obtained by dividing t_n in the Equation (3.10) by $[\![\Delta]\!]_n$.

3.3.3 Park–Paulino–Roesler (PPR) law

Park *et al.* [109] proposed a potential-based model for a mixed mode of fracture named by the authors of PPR (Park–Paulino–Roesler). The PPR model is presented in a potential form (Ψ) and is based, in its extrinsic form, on the physical parameters of resistance: normal cohesive strength (σ_{max}) and the tangential cohesive strength (τ_{max}); on the physical parameters of fracture: normal fracture energy ($\emptyset_n$) and tangential fracture energy ($\emptyset_t$); and on the shape parameters α and β. The shape parameter characterizes the softening response of the material: a value less than 2 causes plateau-type behavior, whereas a value greater than 2 yields behavior indicative of *quasi*-brittle materials. In the simulations carried out here, the resistance parameter σ_{max} is taken to be the tensile strength (f_t) of the material, the fracture parameter $\emptyset_n$ is taken to be the fracture energy (G_F).and their respective properties in tangential direction are taken in the function of the normal parameter for mixed-mode cases. The potential is expressed by:

$$\begin{aligned}\Psi(\llbracket\Delta\rrbracket_n, \llbracket\Delta\rrbracket_t) = \min(\emptyset_n, \emptyset_t) \\ + \left[\Gamma_n\left(1-\frac{\llbracket\Delta\rrbracket_n}{\delta_n}\right)^{\alpha} + \langle\phi_n - \phi_t\rangle\right]\left[\Gamma_t\left(1-\frac{|\llbracket\Delta\rrbracket_t|}{\delta_t}\right)^{\beta}\right. \\ \left. + \langle\emptyset_t - \emptyset_n\rangle\right]\end{aligned} \tag{3.11}$$

in which $\llbracket\Delta\rrbracket_n$ and $\llbracket\Delta\rrbracket_t$ are the normal and tangential separations over the fractured surface. The normal (t_n) and tangential (t_t) cohesive tractions can be obtained through the gradient of the potential concerning $\llbracket\Delta\rrbracket_n$ and $\llbracket\Delta\rrbracket_n$, respectively:

$$\begin{aligned}t_n(\llbracket\Delta\rrbracket_n, \llbracket\Delta\rrbracket_t) &= \frac{\partial\Psi}{\partial\llbracket\Delta\rrbracket_n} \\ &= -\alpha\frac{\Lambda_n}{\delta_n}\left(1-\frac{\llbracket\Delta\rrbracket_n}{\delta_n}\right)^{\alpha-1}\left[\Gamma_t\left(1-\frac{|\llbracket\Delta\rrbracket_t|}{\delta_t}\right)^{\beta}\right. \\ &\quad\left. + \langle\emptyset_t - \emptyset_n\rangle\right] \\ t_t(\llbracket\Delta\rrbracket_n, \llbracket\Delta\rrbracket_t) &= \frac{\partial\Psi}{\partial\llbracket\Delta\rrbracket_t} \\ &= -\beta\frac{\Lambda_t}{\delta_t}\left(1-\frac{|\llbracket\Delta\rrbracket_t|}{\delta_t}\right)^{\beta-1}\left[\Gamma_n\left(1-\frac{\llbracket\Delta\rrbracket_n}{\delta_n}\right)^{\alpha}\right. \\ &\quad\left. + \langle\emptyset_n - \emptyset_t\rangle\right]\frac{\llbracket\Delta\rrbracket_t}{|\llbracket\Delta\rrbracket_t|}\end{aligned} \tag{3.12}$$

in which the term $\langle\cdot\rangle$ is the Macaulay bracket, i.e., $\langle x\rangle = (x + |x|)/2$.

The final crack opening widths δ_n and δ_t are given by:

$$\delta_n = \frac{\alpha\emptyset_n}{\sigma_{max}}, \qquad \delta_t = \frac{\beta\emptyset_t}{\tau_{max}}, \tag{3.13}$$

the energy constants Λ_n and Λ_t, are given by:

$$\Lambda_n = (-\emptyset_n)^{\langle \emptyset_n - \emptyset_t \rangle / (\emptyset_n - \emptyset_t)}, \qquad \Lambda_t = (-\emptyset_t)^{\langle \emptyset_t - \emptyset_n \rangle / (\emptyset_t - \emptyset_n)} \tag{3.14}$$

if $\phi_n \neq \phi_t$. If the fracture energies, then Λ_n and Λ_t are:

$$\Gamma_n = -\emptyset_n, \qquad \Gamma_t = 1 \tag{3.15}$$

Figure 3.4 shows the cohesive tractions surface t_n and t_t for the case where the resistance, fracture, and shape parameters are: $\phi_n = 100\ \text{N/m}$, $\phi_t = 200\ \text{N/m}$, $\sigma_{max} = 40\ \text{MPa}$, $\tau_{max} = 30\ \text{MPa}$, $\alpha = 5$ and $\beta = 1.3$. One can see *quasi*-brittle behavior for the normal traction-displacement surface ($\alpha > 2$) and a plateau-type behavior for the tangential traction-displacement ($\beta < 2$). These surfaces are presented in [109].

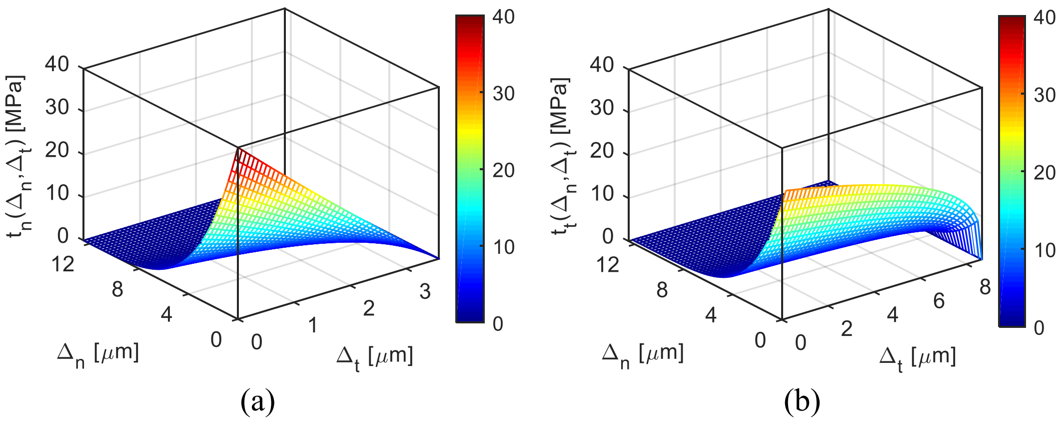

Figure 3.4 – Gradients (cohesive tractions surface) for the extrinsic PPR cohesive model: (a) normal traction displacement and (b) tangential traction displacement.

The surfaces of Figure 3.4 show the same aspect observed in the surfaces of Figure 2.4 relating to the value observed for the maximum shear stress, i.e., the maximum shear stress assumes a value close to half σ_{max}. In the numerical problems tested in this research, the literature does not provide the τ_{max} property, and by observation of the surfaces cited, this property was taken as half of σ_{max}.

The secant iterative procedure requires that the matrix **T** of the Equation (3.3b) becomes:

$$\mathbf{T} = \begin{bmatrix} t_n([\![\Delta]\!]_n, [\![\Delta]\!]_t)/[\![\Delta]\!]_n & 0 \\ 0 & t_t([\![\Delta]\!]_n, [\![\Delta]\!]_t)/[\![\Delta]\!]_t \end{bmatrix} \tag{3.16}$$

3.4 NUMERICAL IMPLEMENTATION

In the G/XFEM strategy, three types of elements can be identified concerning the enrichment. Some elements do not present enrichment at any node and are treated in the standard formulation of finite elements, there are elements crossed by the discontinuity and present enrichment in all its nodes; and also have the so-called blending elements, which present enrichment only in the nodes that also belong to the elements crossed by the discontinuity. In the crack propagation process, when an element is cut by a crack, nodes are then enriched. However, since there is the condition that the displacement jump at the crack tip must be zero, the nodes belonging to the element ahead of the crack tip are not enriched, even if their nodes belong to other elements that are crossed by the discontinuity. This strategy was successfully adopted by Wells and Sluys [138] and Simone [148]. However, when the crack tip enrichment is used, the nodes belonging to the element ahead of the crack tip are enriched with the branch function, the node enrichment process considering this case is shown in Figure 3.5a for the 2D domain.

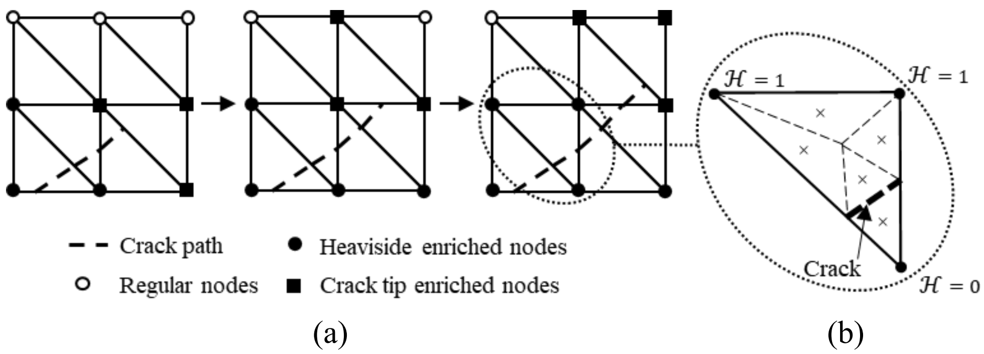

Figure 3.5 – G/XFEM strategy for crack propagation with (a) node enrichment process and (b) integration scheme of an element crossed by a discontinuity.

The propagation criterion is based on the value of the maximum principal tensile stress at all integration points of the element ahead of the crack tip, so that at the end of a displacement increment, a discontinuity is inserted when the value of the maximum principal tensile stress at any integration point is greater than the tensile strength of the material f_t. The discontinuity is introduced through the entire element as a straight line for the 2D domain and a plane surface for the 3D domain, *i.e.*, the normal vector to the discontinuity is constant within the element. The crack is initiated by passing through the integration point of the first element that reaches the propagation criterion.

Finally, in the discrete equation system of G/XFEM, the integration of some terms of stiffness matrix and force vector occurs only on a part of the element domain. A special integration scheme is required to ensure that shape functions remain linearly independent. In the paper of Moës *et al.* [131], Wells and Sluys [138], and Pereira *et al.* [151] it is proposed that the elements crossed by a discontinuity have their domains Ω^+ and Ω^- divided into subdomains, see the Figure 3.5b, this idea is extended to the tetrahedral element, in 3D simulations. In each subdomain, the Gauss quadrature belonging to the adopted element is applied. In the elements that have some of their nodes enriched with the branch function, a greater number of Gauss points is required to perform numerical integration with precision. in this work, a quadrature with 175 integration points of the three-node triangular finite elements is used. Despite this extra computational cost, the number of elements that receive this quadrature is small compared to the total number of elements in the mesh. It is important to point out that for 3D simulation, the enrichment of the crack tip element with the branch functions was not implemented. So, the nodes belonging to the element ahead of the crack tip are not enriched.

For the propagation direction, the maximum accumulation direction of the non-local maximum principal tensile stress (σ_i) in a V-shaped window (the darker region in Figure 3.6) ahead of the crack tip is used, similar to that proposed by Simone *et al.* [40]. This V-shaped window spans a sector with $\theta = 90°$ and is placed with symmetry to the direction of the crack segment that passes through the last crossed element.

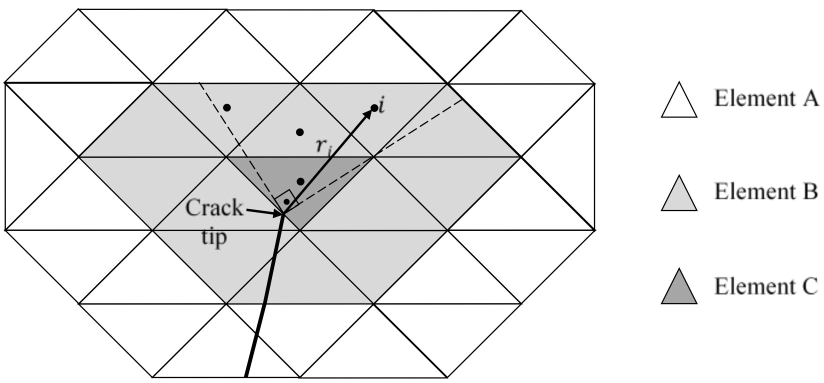

Figure 3.6 – Depiction of the determination of crack propagation direction within a finite element mesh with triangular elements. Element C is directly ahead of the crack tip; elements B share at least one node with element C; and elements A are not considered at crack propagation. The black points within the V-shaped represent Gauss points i.

The vector $\mathbf{r}_{\Gamma_\mathbf{d}}$ in the perpendicular direction of the crack propagation is calculated by:

$$\mathbf{r}_{\Gamma_d} = \sum_{i \in S} \sigma_i \eta_i \frac{\mathbf{r}_i}{\|\mathbf{r}_i\|} \tag{3.17}$$

in which S is the set of integration points i located within the region limited by the V-shaped. The border of the V-shaped window is primarily the crack tip element only, but in the cases that this window does not capture any integration points, then it is extended to the elements sharing at least one node with the crack tip element. The vector $\mathbf{n}_i$ is the principal direction related to σ_i and η_i is a weight associated with the point i calculated using the following Gaussian function:

$$\eta_i = \frac{1}{(2\pi)^{3/2} l^3} \exp\left(-\frac{\|\mathbf{r}_i\|^2}{2l^2}\right) \tag{3.18}$$

in which $\mathbf{r}_i$ is the position vector in the direction of point i for the 2D domain and, for the 3D domain, $\mathbf{r}_i$ is the vector resulting from the shortest distance from point i to the line that characterizes the crack front. l is the rate of decay of the weight function from the discontinuity tip and is taken as approximately three times the typical element size.

The approach used to implement the G/XFEM and the cohesive lows in the 2D domain can be easily generalized for the 3D, but the numerical implementation issues previously described have to be adapted. In a summarized way, for the integration scheme of an element crossed by a fracture, the integration over the Ω^+ is performed by dividing this volumetric region into tetrahedral elements where the correspondent quadrature is applied. The propagation criterion does not change and, for the propagation direction, the V-shaped window presents a depth on each element whose value is equal to the size of the crack edge on that element.

In the 3D domain, the fracture is represented as a surface that cut the element. For the four-node linear tetrahedral finite element, the shape of this surface can only have a quadrilateral or triangular intersection, as can be observed in Figure 3.7. When the intersection is a quadrilateral, the tetrahedron is subdivided into 6 tetrahedral sub-elements and, in case the intersection is a triangle, the tetrahedron is subdivided into 4 sub-elements. As demonstrated by Areias and Belytschko [152], the propagation direction of a plane crack through a tetrahedral element requires a direction criterion only when the crack is initiated or when the crack tip reaches an element by only one of its faces. When the crack tip reaches the tetrahedron on two or more of its faces, its direction is defined by the plane formed by the points that intersect the edges of the tetrahedron.

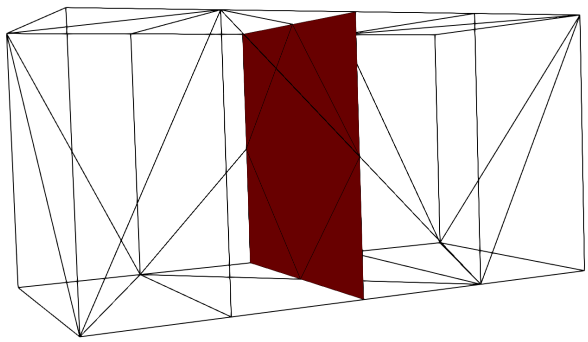

Figure 3.7 – 3D bar modeled with four-node linear tetrahedral finite elements and cut by a fracture represented by the surface in the format of quadrilateral and triangular elements.

3.5 MODE I SIMULATIONS

In this section, the implementation of the exponential, bilinear, and PPR cohesive laws in the G/XFEM framework are tested for mode I crack open using problems from the literature review. In all numerical examples, the simulations are performed using a fine and coarse three-node triangular finite element mesh for 2D analyses and a four-node tetrahedron finite element for 3D, the refinement occurs only in the potential fracture zone. The number of elements (M) is informed below each mesh. The secant method procedure has been used to trace the response in the nonlinear regime. All 2D simulations considered the plane stress state, except for the Koyna dam, which considered the plane strain state. For the PPR law, the fracture and shape parameter related to two tangential tension is set to zero. The crack tip enrichment is tested only for coarse meshes since a fine mesh can generally provide good results.

3.5.1 Unnotched Three-Point Bending (TPB) beam simulations

The proposed implementation is validated for mode I crack open through the unnotched TPB beam presented in Wells and Sluys [138] and de Borst [150], where the authors performed simulations for this test using the same exponential cohesive law implemented here. The geometry and boundary conditions are shown in Figure 3.8, with $\mathrm{L} = 10$ mm, $\mathrm{H} = 3$ mm, and $\mathrm{B} = 1$ mm, the figure also shows the meshes used in this work. The validation is verified by comparing the obtained load-displacement (P-δ) curves for the three cohesive laws implemented (exponential, bilinear, and PPR) with a numerical response of [138].

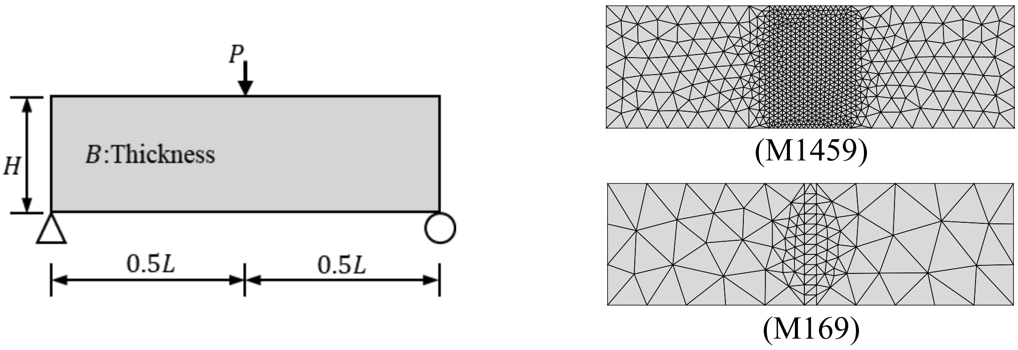

Figure 3.8 – Unnotched Three-Point Bending (TPB) test: geometry, boundary conditions, and finite element meshes.

The material properties and normal fracture and shape parameters used in the simulations are Young's modulus $\mathrm{E} = 100\ \mathrm{MPa}$, Poisson's ratio $\upsilon = 0.0$, cohesive strength $\sigma_{\mathrm{max}} = 1.0\ \mathrm{MPa}$, fracture energy $\emptyset_{\mathrm{n}} = 100\ \mathrm{N/m}$ and $\alpha = 5.0$, for the bilinear law the extra properties initial fracture energy $\mathrm{G_f} = 40\ \mathrm{N/m}$ and kink point $\Psi_1 = 0{,}25$ are adopted. The simulations were first performed using the fine mesh. Figure 3.9 shows the P-δ curves for the three cohesive laws implemented, the curves obtained with exponential and PPR cohesive laws are in very good agreement with the result of [138]. The slightest differences are caused by the use of a different mesh and by the crack propagation not being perfectly straight (see the crack propagation to the right of the graph). Moreover, the shape of the curve is similar to its cohesive law, which causes the difference between the bilinear curve and the others.

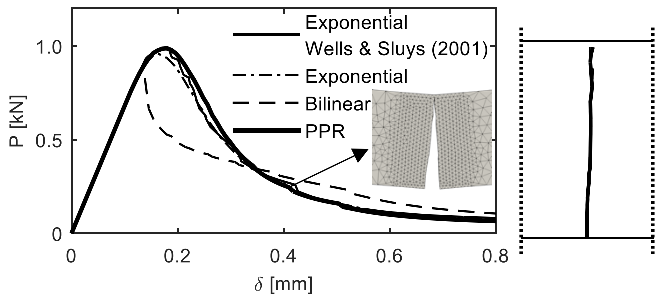

Figure 3.9 – Load-displacement (P-δ) curves for the unnotched TPB beam using the fine mesh: comparison with the numerical response of [138] and crack paths.

Once the proposed implementation has been validated for mode I, its ability to produce good results for coarse meshes is tested next. Figure 3.10 shows the P-δ curves and the crack paths for the three cohesive laws simulated with the coarse mesh and compares them with the result of [138]. To the left are shown the curves only with the Heaviside enrichment function, and to the right with the Heaviside and crack tip (CT) enrichment functions. The results show that even for the coarse mesh, the curves present a good approximation with those for the refined mesh and when the CT enrichment is used the differences practically disappear, *i.e.*, the peak load and softening are roughly the same for the two mesh sizes. In general, the crack has difficulties propagating properly in mesh with large element size; however, the propagation in this test occurred in a region close to the expected, mainly for the simulations with CT enrichment.

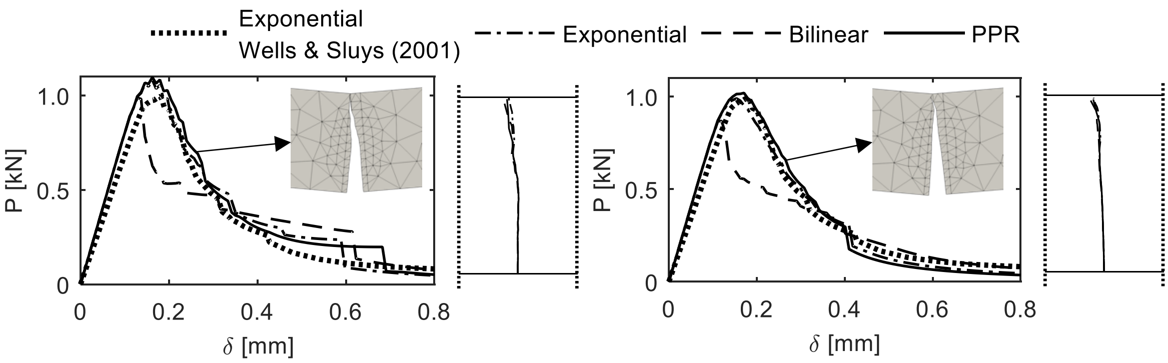

No CT enrichment CT enrichment ($k = 1.0$)

Figure 3.10 – P-δ curves for the unnotched TPB beam using the coarse mesh: comparison with numerical response of [138] and crack paths.

The last analysis with this test setup is intended to show the influence of the parameter k of the CT enrichment function in the P-δ curves. For this, simulations with the coarse mesh are carried out with the PPR cohesive law for different values of k, the results are shown in Figure 3.11. As can be seen, the numerical response is practically the same for the three values of k tested, this result initially indicates that such a parameter does not affect the response, but throughout this paper, other tests are performed to verify this.

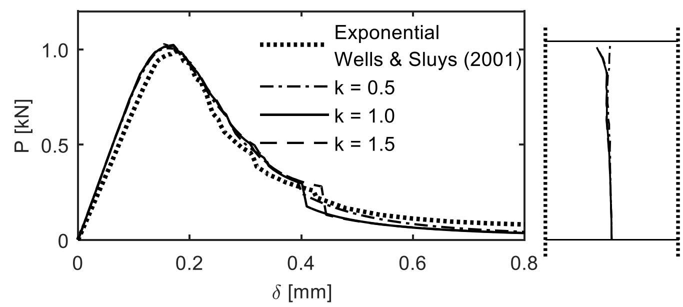

Figure 3.11 – P-δ curves for the unnotched TPB beam using the coarse mesh for different values of k: comparison with numerical response of [138] and crack paths.

3.5.2 Splitting tensile strength simulations

The tensile strength of concrete and rocks can be obtained by a laboratory test with a cylindrical specimen in diametral compression called the ‘splitting tensile strength test’, the procedure is based on [153]. The tensile strength (σ_{st}) is given by

$$\sigma_{st} = \frac{2F}{\pi \, d \, L_{st}} \tag{3.1}$$

in which d is the cylinder diameter, L_{st} is the cylinder length, and F is the peak load obtained in the test. The numerical simulations performed here have the objective to show that the strategy of combining the G/XFEM and the extrinsic PPR cohesive law, as well as the other two cohesive laws, can predict the load F expected for a splitting tensile strength test, through the Equation (3.1), knowing the material properties and fracture parameters. Figure 3.12 show the geometry and boundary conditions of the test, the geometric data are $d = 100$ mm and $L = 200$ mm. The symmetry of the problem is harnessed and only half of the specimen is modeled, the crack propagates from a very small notch placed in the center of the cylinder. The fine and coarse finite element meshes used in the simulations are shown in Figure 3.12.

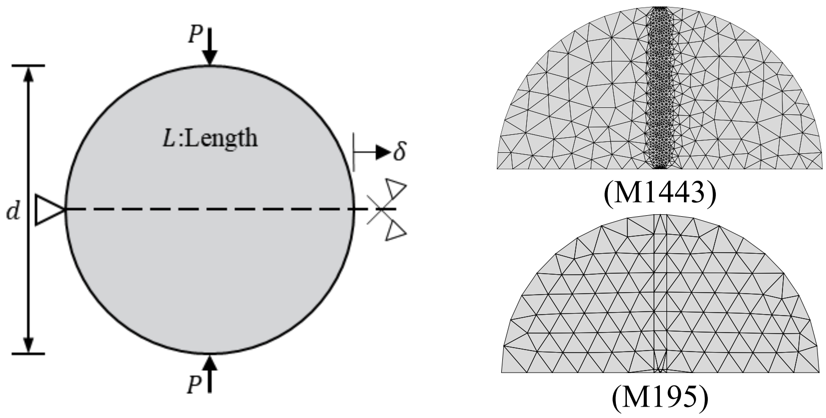

Figure 3.12 – Splitting tensile strength test: geometry, boundary conditions, and finite element meshes.

The concrete material data and fracture parameters are taken from the splitting tensile strength test performed by [154], their values are Young's modulus $E = 39.399$ MPa, Poisson's ratio $\upsilon = 0.20$, normal cohesive strength $\sigma_{max} = 6.077$ MPa, normal fracture energy $\emptyset_n = 113.95$ N/m, normal shape parameter $\alpha = 5.0$, initial fracture energy $G_f = 49.4815$ N/m and $CTOD_c = 0.0121355$ mm. The normalized load (P/F) versus displacement (δ) curves obtained with the three cohesive laws implemented are compared in Figure 3.13 for the fine and the coarse mesh, the load P is presented normalized by F. From Equation (3.1), is calculated considering $\sigma_{st} = \sigma_{max}$. The result shows that the strategy was able to return P_{max} close to F for the three implemented laws independent of the mesh size and that the crack propagation is in good agreement with the expected. Note that although the CT enrichment was not used in the simulations with the coarse mesh, their peak load is practically the same as the fine mesh, because of this, the results with such an enrichment function were not shown.

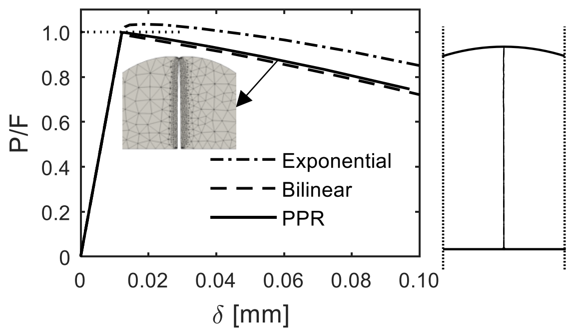

(a) fine mesh

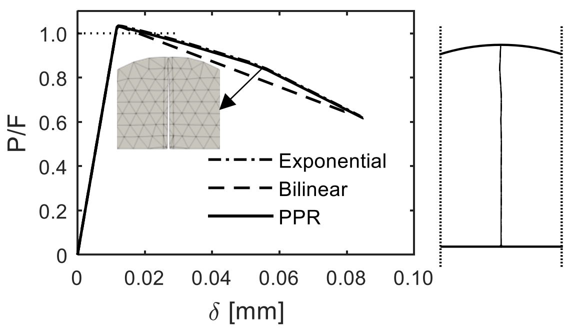

(b) coarse mesh

Figure 3.13 – Normalized load-displacement response and crack paths for the splitting tensile strength simulations. The displacement (δ) is measured in the horizontal direction at the rightmost node in the mesh, as shown in Figure 3.12.

3.5.3 TPB in a single edge notch beam (SEN(B)) simulation

The proposed strategy is tested with the experimental program of Roesler *et al.* [87], where the authors performed a series of three-point bending (TPB) tests with three sizes of a single edge notch beam SEN(B). Figure 3.14 show the geometry and boundary conditions of the test setup and Table 3.1 lists the dimensions of each beam size tested. The width of the notch adopted was 1 mm for specimen depth $\mathrm{H} = 63$ mm and 2 mm for the other two specimens.

Table 3.1 – Single edge notch beam dimensions in mm of Roesler *et al.* [87].

Depth (H)	Length	Thickness	Notch	Span
63	350	80	21	250
150	700	80	50	600
250	1100	80	83	1000

Here, numerical simulations were performed to verify the capacity of the three cohesive laws implemented in the G/XFEM framework to predict the monotonic load (P) versus Crack Mouth Opening Displacement (CMOD) curve of geometrically similar notched concrete beams with different sizes and test the mesh objectivity of this strategy. To achieve this objective, simulations are performed with a fine mesh and a coarse mesh for each specimen depth (H), the meshes can be accessed in Figure 3.14. For the fine mesh, only the Heaviside enrichment function is used, while for the coarse mesh, the crack tip (CT) enrichment function is also used to return better results. The material properties and fracture parameters provided by Roesler *et al.* [87] are adopted, their values are: Young's modulus $\mathrm{E} = 32$ MPa, Poisson's ratio $\upsilon = 0.2$, initial fracture energy $\mathrm{G_f} = 56.7\ \mathrm{N/m}$, $\mathrm{CTOD_c} = 0.0186\ \mathrm{mm}$, normal shape parameter $\alpha = 5.0$, normal cohesive strength $\sigma_{max} = 4.15$ MPa and normal fracture energy $\emptyset_n = 119$ N/m for beam with H = 63 mm, $\emptyset_n = 164$ N/m for beam with H = 150 mm and $\emptyset_n = 167$ N/m for beam with H = 250 mm.

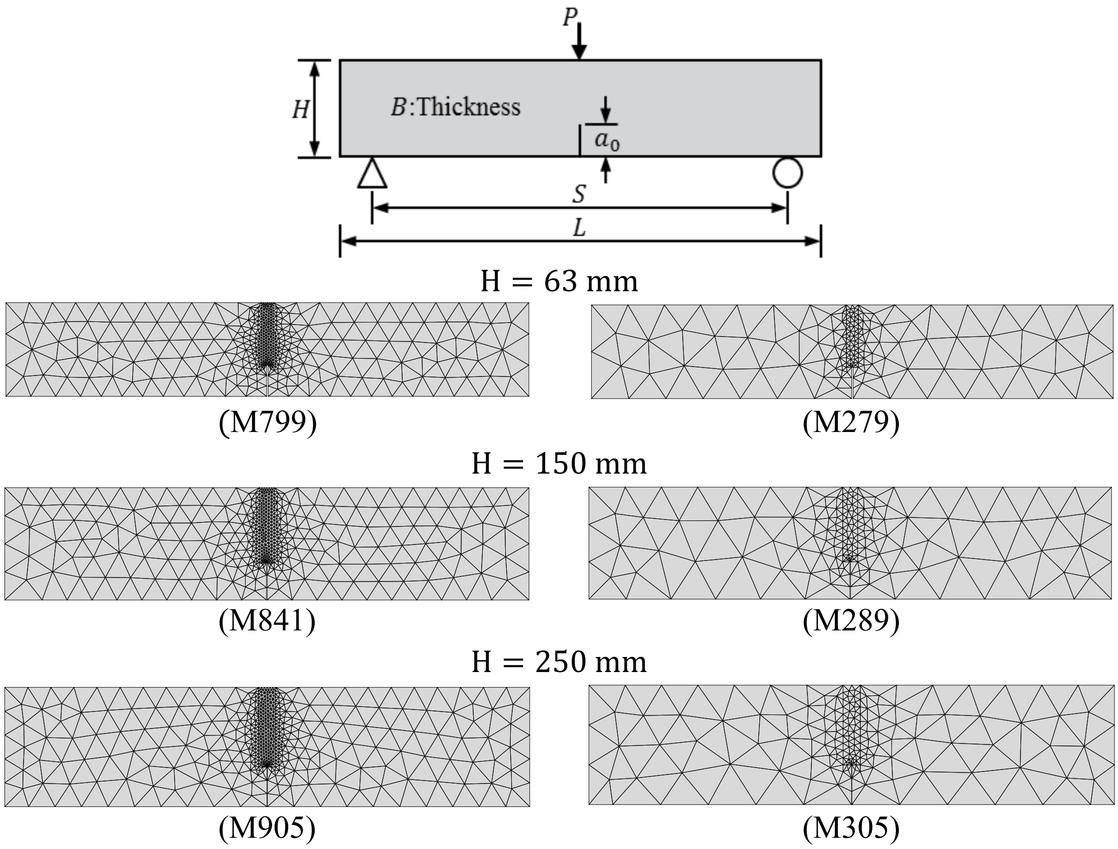

Figure 3.14 – TPB in a single edge notch beam (SEN(B)) test: geometry, boundary conditions, and finite element meshes of each specimen depth (H).

The predicted P-CMOD curves for each specimen size are compared with experimental data of [87] in Figure 3.15, the figure also shows the crack path of each simulation performed. As can be seen, the curves obtained with PPR and exponential cohesive laws result in an overestimation of the peak load, this behavior does not occur for bilinear law, this behavior was also noted in previous tests. Despite the overestimation of the peak load, the softening curve of numerical results is in good agreement with the experimental measurement. Comparing the results for fine and coarse meshes, it is clear that the strategy to combine the Heaviside enrichment function with the CT enrichment function in coarse mesh provided results with practically the same accuracy as fine mesh. However, the accuracy gain is not higher for the mesh used because even without the enrichment function the results are good, the previous test confirms this observation. Concerning the crack propagation, the implemented scheme proved efficient in predicting crack path for all simulations, even those with coarse meshes without CT enrichment.

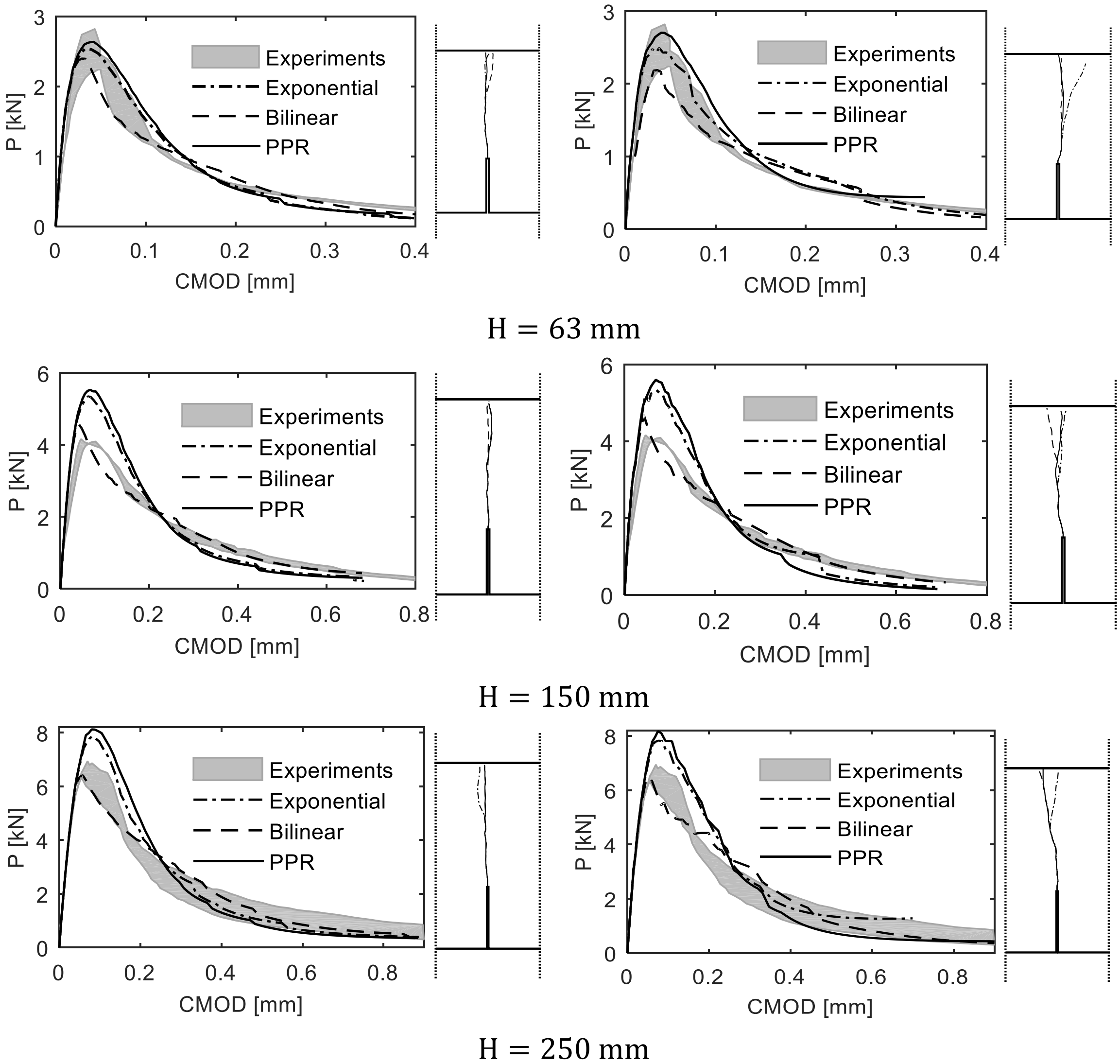

Figure 3.15 – Results of predicted P-CMOD curves compared with experimental data of [87]: using the fine mesh (left) and the coarse mesh (right). The crack paths are shown at the right of each graph.

3.5.4 Three-dimensional simulations of the unnotched TPB beam

This section presents the results obtained for three-dimensional simulations of the unnotched TPB beam described in Section 3.5.1. The simulation of this beam in 3D was chosen because it makes it possible to verify the implementation of the cohesive laws implemented in the G/XFEM framework since the problem was created for this purpose by the researchers [138]. The test setup and the 3D mesh used are shown in Figure 3.16, the mesh has 1724 tetrahedron elements. The material and fracture parameter can be accessed in Section 3.5.1.

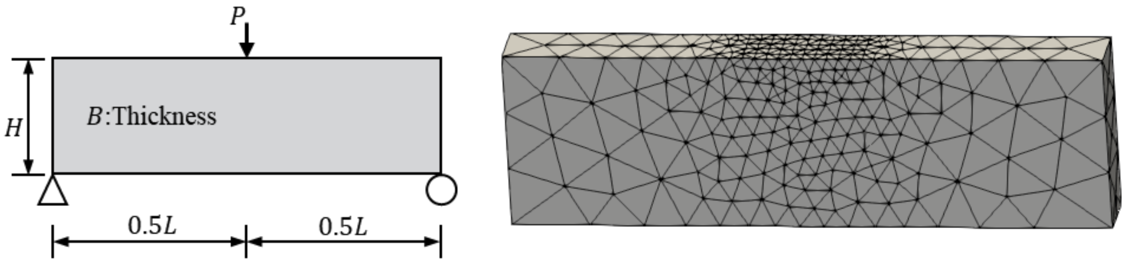

Figure 3.16 – Unnotched Three-Point Bending (TPB) test: geometry, boundary conditions, and 3D finite element mesh with 1724 elements.

The simulations were performed with the three cohesive laws implemented and the graphics of force P *versus* displacement δ is compared with the numerical reference result of [138] in Figure 3.17, the figure also shows the deformed mesh.

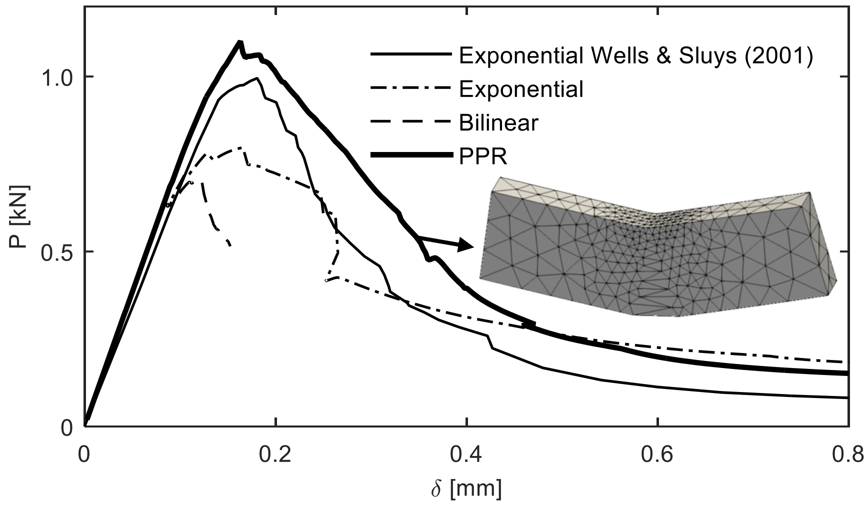

Figure 3.17 – P-δ curves for the 3D simulation of unnotched TPB beam using: comparison with numerical response of [138].

As can be seen in Figure 3.17, the P-δ responses obtained are following those observed in the 2D simulations for the P_{max} values. However, only the PPR law managed to present a softening behavior aligned with the reference curve. It is important to point out that the curves could be improved if the crack propagation was perfectly straight in the simulation. But, as can be seen in Figure 3.18, the crack path surface has a slightly tortuous appearance, this characteristic contributed to differences between the P-δ curves and the reference curve. The simulation with the bilinear law was aborted due to crack propagation problems caused by the crack path aspect mentioned.

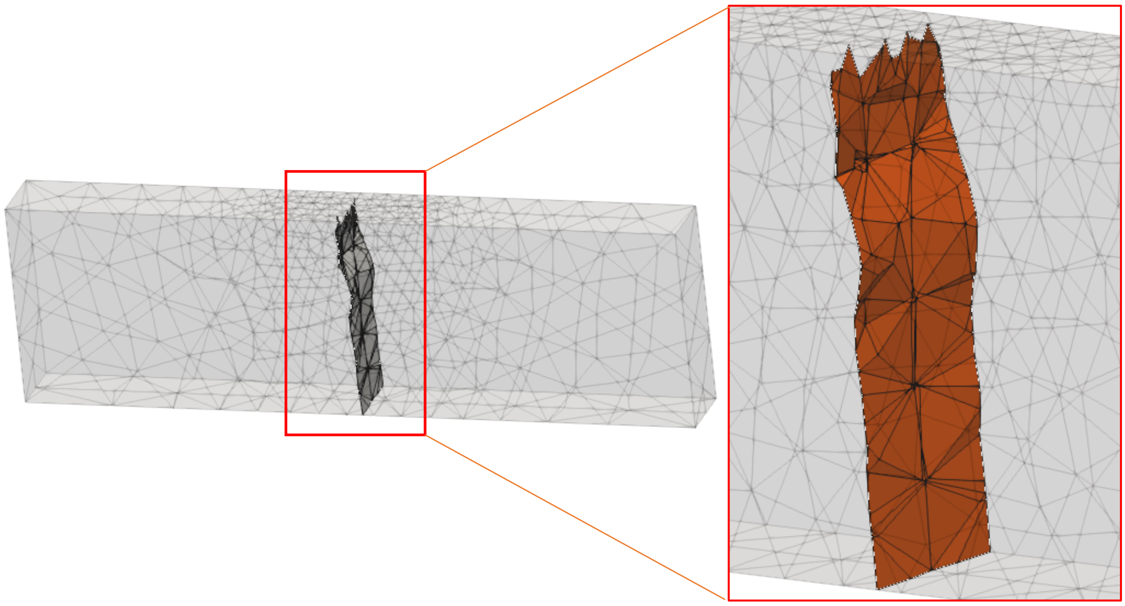

Figure 3.18 – Crack path surface of the unnotched TPB beam obtained with the PPR law.

3.6 MIXED MODE (I+II) SIMULATIONS

A study of the PPR model into the G/XFEM framework for mixed-mode failure problems is performed. The simulation characteristics described in the introduction of the previous section related to finite element meshes, stress state, and method to trace nonlinear response are adopted here. Two problems from the literature review are analyzed: the first one is a common test used to validate the PPR model implementation, and the second is a benchmark problem currently used by researchers to study cohesive crack propagation. In this section, the effects of the tangential fracture parameters (τ_{max} and $\emptyset_t$) from de PPR cohesive law in the global response and the crack path were investigated, these properties generally are not provided for the literature. Additionally, the effects of mesh resolution and the parameter k from the crack tip enrichment function are also discussed. Finally, a simulation of the DENT test reported in Section 2.4.4 is performed to show the robustness of the proposed strategy to predict the behavior of rupture in the 3D domain.

3.6.1 Mixed mode bending (MMB) simulation

Reeder and Crews [155] developed a combination of the double cantilever beam (mode I) and end-notch flexure test (mode II) to measure the fracture toughness for various mode I/II ratios. The method is known as Mixed-Mode Bending (MMB) delamination testing and has been standardized by ASTM standard D 6671/D 6671M [156]. The MMB test has been used to validate several cohesive zone models for fracture in mixed mode [109, 118, 119, 157, 158] by comparing the numerical results with the analytical solution provided by Mi *et al.* [159]. The analytical solution consists of one part based on elastic beam theory during initial elastic loading and two parts based on linear elastic fracture mechanics during debonding. More details can be found in the appendix A of Park *et al.* [109].

In the paper of Park and Paulino [118], the authors replied to the MMB test with the intrinsic PPR model in 2D for various combinations of normal and tangential cohesive strength and fracture energy. The boundary conditions of the MMB test are shown in Figure 3.19, the geometric value adopted by [118] were $\mathrm{c} = 60\ \mathrm{mm}$, $\mathrm{L} = 51\ \mathrm{mm}$, $\mathrm{b} = 25.4\ \mathrm{mm}$, $\mathrm{h} = 1.56\ \mathrm{mm}$, and $\mathrm{a_0} = 33.7\ \mathrm{mm}$. Cerrone *et al.* [119] validated the intrinsic PPR model in 3D with the MMB test and the same fracture parameter and geometric data of [118]. Thus, the extrinsic PPR model with G/XFEM for mixed states was validated by comparing the response obtained with analytical solutions of [159] and the numerical response of [118, 119].

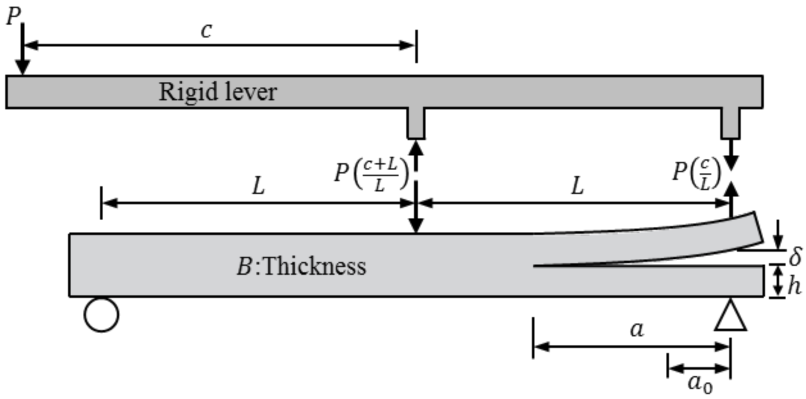

Figure 3.19 – Geometry and boundary conditions of the mixed-mode bending specimen.

The material data are Young's modulus $\mathrm{E} = 122\ \mathrm{GPa}$ and Poisson's ratio $\upsilon = 0.25$, the fracture parameters are cohesive strength $\sigma_{\max} = \tau_{\max} = 10\ \mathrm{MPa}$ and fracture energy $\emptyset_{\mathrm{n}} = \emptyset_{\mathrm{t}} = 500\ \mathrm{N/m}$ and the shape parameter are $\alpha = \beta = 3$. The finite element mesh used to discretize the main domain has 12035 three-node triangular elements; this great number is needed for the elastic beam response. Crack propagation is set to be perfectly straight to guarantee the same characteristic of the refereed papers simulations and, as the mesh is very fine, the crack tip enrichment was not considered. The obtained response for the load (P) versus displacement (δ) is compared to the analytical solution and computational response of [118, 119] in Figure 3.20, which show yet a detail of the crack crossing the elements. Note that the response obtained with the integration of the PPR model and G/XFEM is similar to the other computational curves and, therefore, converges to the analytical.

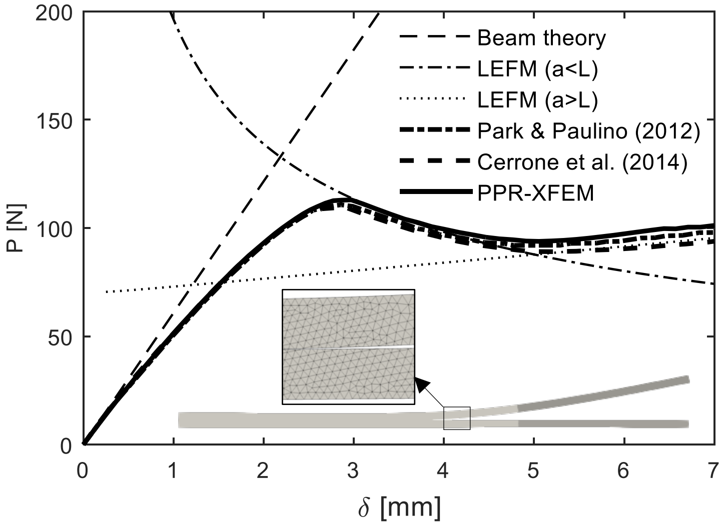

Figure 3.20 – Load (P) *versus* displacement (δ) obtained compared with analytical solutions and computational results of Park and Paulino [118] and Cerrone et al. [119].

3.6.2 SEN(B) in anti-symmetric Four-Point Shear (FPS) simulations

The single-edge notched concrete beam in anti-symmetric Four-Point Shear (FPS) is one of the tests performed by Schlangen [81] to analyze the mechanisms developed in the concrete cracking process in mixed mode. Figure 3.21 shows the geometry and boundary conditions that result in a curved crack path starting at the top right corner of the notch and propagating to the right corner of the top center loading plate. In the figure, $\mathrm{L} = 440\ \mathrm{mm}$, $\mathrm{H} = \mathrm{B} = 100\ \mathrm{mm}$, $\mathrm{a} = 20\ \mathrm{mm}$, $\mathrm{h} = 5\ \mathrm{mm}$, and loading plates have a width of $20\ \mathrm{mm}$. This problem has been used to test several computational models of fracture with arbitrary crack propagation [138, 148, 150, 160, 161]. The two meshes used (the fine and the coarse), the element size, and the element number of each one are also shown in Figure 3.21.

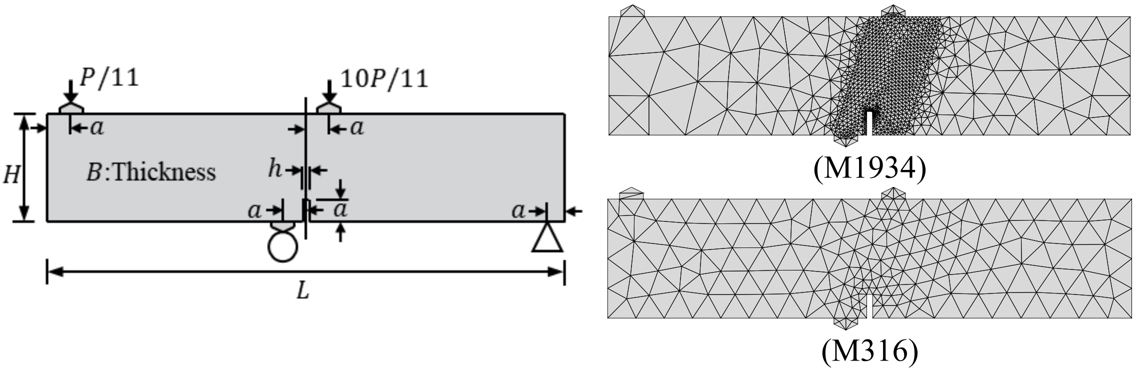

Figure 3.21 – SEN(B) in anti-symmetric Four-Point Shear: geometry, boundary conditions, and finite element meshes.

The material properties and fracture parameters used in the analysis of the SEN(B) in anti-symmetric FPS are Young's modulus $\mathrm{E} = 35\,\mathrm{GPa}$, Poisson's ratio $\upsilon = 0{,}20$, normal cohesive strength $\sigma_{\mathrm{max}} = 3{,}0\,\mathrm{MPa}$, normal fracture energy $\emptyset_{\mathrm{n}} = 100\,\mathrm{N/m}$ and shape parameter $\alpha = \beta = 5.0$. In this study, two cases are tested. In the first, several combinations of tangential cohesive strength in the function of normal cohesive strength and tangential fracture energy in the function of normal fracture energy are tested. The simulations are performed using the fine mesh and the crack tip enrichment is not used. The results obtained for the load (P) and the Crack Mouth Sliding Displacement (CMSD) measured in the mouth of the notch are shown in Figure 3.22. As can see, the extrinsic PPR model can reproduce the softening response of the experiment. The best result is obtained when the cohesive strength and fracture response has their value given by $\tau_{max} = 0.5\sigma_{max}$ and $\emptyset_t = \emptyset_n$, see the comparison with the computation result of [161]. The crack path of all simulations is in good agreement with the experimental crack envelope (right detailed in Figure 3.22), indicating the ability of the proposed strategy to predict the crack formation and propagation in materials like concrete.

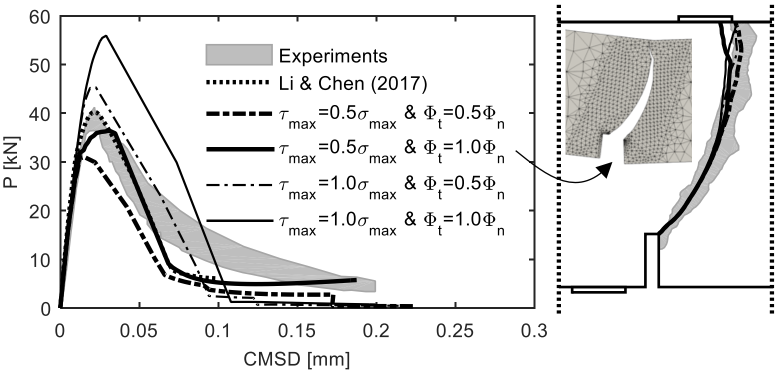

Figure 3.22 – Load (P) versus CMSD curves for the SEN(B) in anti-symmetric FPS using the fine mesh: experimental response, a computational result of Li and Chen [161], and results obtained with the PPR model. To the right the cracked envelope.

In the second case, the extrinsic PPR model into the G/XFEM framework with the coarse mesh was tested. The tangential fracture parameter adopted is the one that returned the best result in the previous case, *i.e.*, $\tau_{max} = 0.5\sigma_{max}$ and $\emptyset_t = \emptyset_n$. Simulations using the crack tip (CT) enrichment function with various values of k is performed and compared to the simulation with no CT enrichment. The curves can be seen in Figure 3.23, where the computational result of [161] is also shown. The adoption of different values of k caused considerable differences in the softening response, but not in the peak load, the best result is observed for $k = 1.0$. For this problem, the use of the CT enrichment function is determinant to achieve good results. Finally, even for the coarse mesh the crack paths remain similar to the experimental, see right detailed in Figure 3.23.

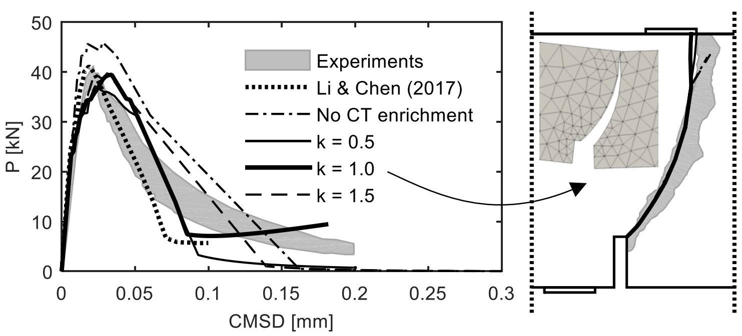

Figure 3.23 – P-CMSD curves for the SEN(B) in anti-symmetric FPS using the coarse mesh and adopting $\tau_{max} = 0.5\sigma_{max}$ and $\emptyset_t = \emptyset_n$. To the right, the crack envelop.

3.6.3 Three-dimensional simulations of the DENT test

The DENT setup simulated in Section 2.4.4 with the proposed damage approach is now tested with the PPR cohesive low in the framework of the 3D G/XFEM implemented. The setup data and the material and fracture properties can be accessed in Section 2.4.4. The simulation was performed using the coarse mesh using only the PPR law. The value of the tangential fracture parameter adopted was defined in function of the normal fracture parameter since these parameters are not reported in the literature. The values adopted were $\tau_{max} = 0.5\sigma_{max}$ and $\emptyset_t = \emptyset_n$. Figure 3.24a show the curve obtained for vertical force P_n *versus* vertical tensile displacement δ_n and compare it with experimental ones and with simulations from the literature; The results show an even greater overestimation of the response for P_{max} and softening when compared to the overestimation reported in Section 2.4.4. Despite the result for P_n *versus* $\delta_n$not being able to predict the resistance of the structure, the crack path surface of Figure 3.24b is in good agreement with the experimental crack patterns region of Figure 2.12. It is clear from the results that the strategy of the CZM associated with the G/XFEM framework can correctly predict the crack path of structures made of *quasi*-brittle materials.

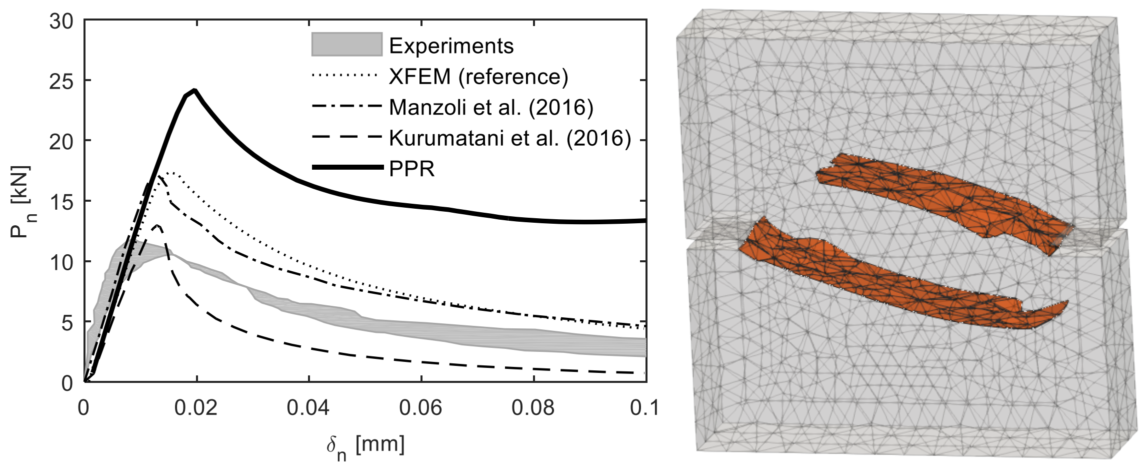

(a) (b)

Figure 3.24 – Three-dimensional simulation of DENT: (a) load *versus* displacement curve comparison with experimental ones and simulations from the literature; (b) crack path surfaces.

3.6.4 Real scale problem: Koyna dam

The Koyna dam described in Section 2.4.6 is simulated here to verify the ability of the G/XFEM approach with the PPR law to predict structural behavior and crack propagation direction in the mixed mode in a full-scale structure. The simulations were performed with the coarse mesh presented in Section 2.4.6, considering the singular enrichment with $k = 1$. The material properties and fracture parameters used are Young's modulus $E = 32$ GPa, Poisson's ratio $\upsilon = 0{,}20$, normal cohesive strength $\sigma_{max} = 1{,}0$ MPa, normal fracture energy $\emptyset_n = 100$ N/m and shape parameter $\alpha = \beta = 5.0$. In this study, several combinations of tangential cohesive strength in the function of normal cohesive strength and tangential fracture energy in the function of normal fracture energy are tested and compared with numerical simulations from the literature. The numerical curves of overflow height (h_{ov}) *versus* crest horizontal (δ_{hc}) displacements are shown in Figure 3.25. As can be seen, the graph shows that the simulations with the proposed strategy resulted in curves similar to that found in the literature for [107], but with a more rigid response than the curves of [74, 108]. This is related to the fact that both the Gioia mesh and the coarse mesh used have few elements, resulting in less displacement for the same stage of loading of the dam crest. For all combinations of cohesive strength and fracture energy, the curves were similar, indicating that the tangential part of the cohesive strength and fracture energy does not significantly influence this problem.

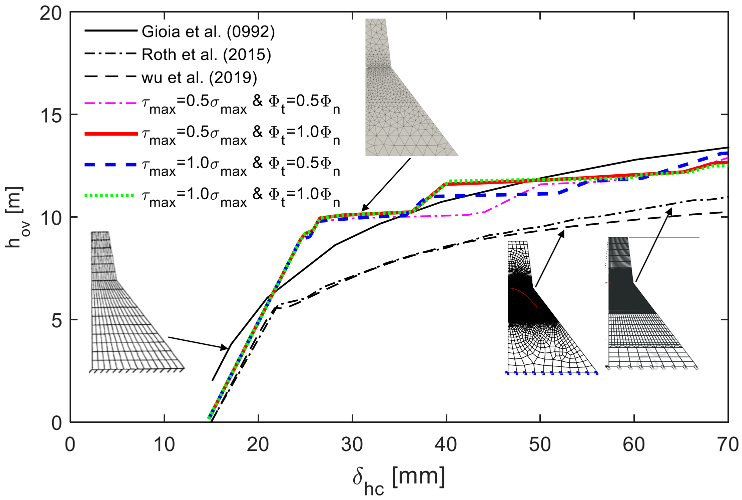

Figure 3.25 – Numerical curves of h_{ov} versus δ_{hc} of the concrete Koyna dam. Comparison with simulations from the literature.

Finally, Figure 3.26 compare the crack path of [108] with the crack path obtained with the coarse mesh. The crack paths are similar, but the proposed approach can predict the structural behavior of the Koyna dam with a mesh with much fewer elements than [108]. Regarding the crack branching captured by the implemented damage model discussed in Chapter 2, the G/XFEM strategy failed to recreate this behavior, however other similar strategies did not either.

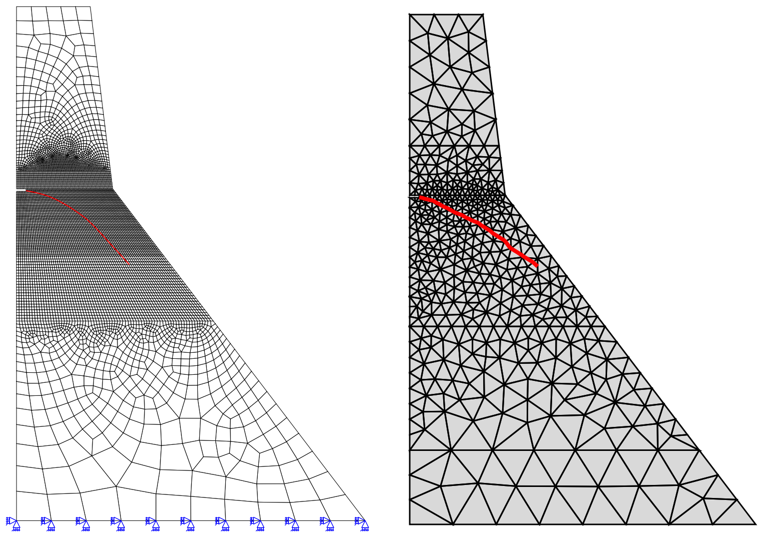

(b) (c)

Figure 3.26 – Crack path for the concrete Koyna dam of (a) Wu *et al*. [108] and (b) coarse mesh.

3.7 PARTIAL CONCLUSIONS

This chapter has implemented the Park-Paulino-Roesler (PPR) cohesive law into the Generalized Finite Element Method (G/XFEM) framework to predict the fracture behavior of *quasi*-brittle materials structures subjected to mode I and mixed mode of failure. The implementation was validated by simulating several benchmark problems from the literature and comparing the structural response obtained with the experimental, analytical, and/or numerical response found in the literature for such problems. Despite the overestimation of the peak load on the structural response, the comparison showed that the G/XFEM together with the PPR model can reproduce/predict, with mesh objectivity, the maximum tensile strength and softening behavior of the samples, proving the efficiency and accuracy of this strategy in predicting the behavior of rupture for both fracture modes.

The problem to simulate cohesive mixed mode failure with the PPR model is the non-available tangential parameter (cohesive strength and fracture energy) to characterize the softening curve. Here, these values are adopted in the function of the normal cohesive strength and normal fracture energy. Different combinations were tested and the best results are provided for the relation $\tau_{max} = 0.5\sigma_{max}$ and $\emptyset_t = \emptyset_n$. With relation to crack tip enrichment, the results showed that this feature is essential to guarantee the mesh size independence, otherwise, only fine mesh can return satisfactory results, which is an important requisite in computational modeling. The simulation for the three values of the branch function exponent returned practically the same result for the global response of the problems simulated, but the results for $k = 1$ were most consistent for both global response and crack path in all simulations performed.

The simulations performed demonstrated that the implementation of Cohesive Zone Models into the Generalized Finite Element Method managed to predict two- or three-dimensional crack path independent of the mesh adopted using a simple criterion for the direction propagation and the cohesive Park-Paulino-Roesler cohesive law was able to predict the experimental curves for structures with mixed mode of failure. The research resulted in software capable to simulate various types of *quasi*-brittle structures, with different types of loading and boundary conditions for two- and three-dimensional domains.

4 CONCLUSIONS AND SUGGESTIONS FOR FUTURE WORK

This section presents the general conclusions obtained in this research and suggestions for future work.

4.1 GENERAL CONCLUSIONS

This research formulated and implemented a novel damage approach based on damage mechanics and fracture laws within the context of the thermodynamics of irreversible processes for damage evolution in *quasi*-brittle materials, including fiber incorporation, to predict failure in modes I and mixed (I+II) conditions. The damage evolution law is based only on strength and fracture properties commonly determined in standard fracture tests, and no further calibration or analysis parameters needed to be performed. The proposed strategy for the local energy dissipation controlled by the regularization of fracture energy and element length ensured that different mesh densities dissipated the same specific energy during the damage evolution. The damage model was demonstrated to be mesh-objective and mesh-independent, and the comparison with the experimental results demonstrated the capabilities of the model in predicting the behavior of rupture of *quasi*-brittle structure with no fiber incorporation submitted to failures in mode I and mixed mode. The proposed approach managed to reduce the computational cost by using relatively coarse meshes and no expensive non-local algorithm.

This research also combined the cohesive zone model, by the Park-Paulino-Roesler law, with the Generalized Finite Element Method to predict the fracture behavior of structures made of *quasi*-brittle materials subjected to mode I and mixed crack opening. The approach was able to accurately reproduce the maximum tensile strength and softening behavior of the benchmark problem of the literature with mesh objectivity. The simulations performed demonstrated that the implementation managed to predict two- or three-dimensional crack path propagation independent of the mesh adopted using a simple criterion for the direction propagation and the cohesive Park-Paulino-Roesler cohesive law was able to predict the experimental curves for structures with a mixed mode of failure. The research resulted in software capable to simulate various types of *quasi*-brittle structures, with different types of loading and boundary conditions, for two- and three-dimensional domains.

4.2 SUGGESTIONS FOR FUTURE WORK

As recommendations for future work and, especially, for the development of the proposed damage approach and the implementation of the cohesive zone model into the G/XFEM framework, it is proposed:

- To implement the damage approach and G/XFEM framework to simulate *quasi*-brittle failure in mode I and mixed-mode conditions using a continuous-discontinuous strategy in a three-dimensional domain.

- To implement the GFEM polynomial enrichment to simulate the proposed damage approach with very coarse meshes.

- To model hydraulic fracturing by the extrinsic PPR cohesive zone law in the G/XFEM framework.

- To implement other propagation criteria and directions of the crack path, such as the acoustic tensor [19] or J integral [21], and compare it with the use of the principal stress criterion implemented in this research.

- To implement the singular enrichment to propagate the crack in three-dimensional very coarse meshes.

REFERENCES

[1] S. P. Shah, S. E. Swartz, and C. Ouyang, *Fracture Mechanics of Concrete: Applications of Fracture Mechanics to Concrete, Rock and Other Quasi-Brittle Materials* (Wiley-Interscience publication). Wiley, 1995.

[2] J. Lemaitre and H. Lippmann, *A Course on Damage Mechanics*. Springer Berlin Heidelberg, 1996.

[3] J. Lemaitre and R. Desmorat, *Engineering damage mechanics: ductile, creep, fatigue and brittle failures*. Springer Science & Business Media, 2006.

[4] G. I. Barenblatt, "The formation of equilibrium cracks during brittle fracture. General ideas and hypotheses. Axially-symmetric cracks," *Journal of Applied Mathematics and Mechanics,* vol. 23, no. 3, pp. 622-636, 1959, doi: https://doi.org/10.1016/0021-8928(59)90157-1.

[5] G. I. Barenblatt, "The Mathematical Theory of Equilibrium Cracks in Brittle Fracture," in *Advances in Applied Mechanics*, vol. 7, H. L. Dryden, T. von Kármán, G. Kuerti, F. H. van den Dungen, and L. Howarth Eds.: Elsevier, 1962, pp. 55-129.

[6] D. S. Dugdale, "Yielding of steel sheets containing slits," *Journal of the Mechanics and Physics of Solids,* vol. 8, no. 2, pp. 100-104, 1960/05/01/ 1960, doi: https://doi.org/10.1016/0022-5096(60)90013-2.

[7] C. Geuzaine and J. F. Remacle, "Gmsh: A 3-D finite element mesh generator with built-in pre-and post-processing facilities," *International journal for numerical methods in engineering,* vol. 79, no. 11, pp. 1309-1331, 2009.

[8] A. Hillerborg, "Numerical methods to simulate softening and fracture of concrete," in *Fracture mechanics of concrete: structural application and numerical calculation*: Springer, 1985, pp. 141-170.

[9] T. Belytschko and T. Black, "Elastic crack growth in finite elements with minimal remeshing," *International journal for numerical methods in engineering,* vol. 45, no. 5, pp. 601-620, 1999.

[10] P. A. Cundall and O. D. L. Strack, "A discrete numerical model for granular assemblies," *geotechnique,* vol. 29, no. 1, pp. 47-65, 1979.

[11] M. Jirásek, "Damage and smeared crack models," in *Numerical modeling of concrete cracking*: Springer, 2011, pp. 1-49.

[12] J. Hult, "Creep in continua and structures," in *Topics in applied continuum mechanics*: Springer, 1974, pp. 137-155.

[13] A. Hillerborg, M. Modéer, and P. E. Petersson, "Analysis of crack formation and crack growth in concrete by means of fracture mechanics and finite elements," *Cement and concrete research,* vol. 6, no. 6, pp. 773-781, 1976.

[14] Z. P. Bažant, "Mechanics of fracture and progressive cracking in concrete structures," in *Fracture mechanics of concrete: Structural application and numerical calculation*: Springer, 1985, pp. 1-94.

[15] Y. S. Jenq and S. P. Shah, "Nonlinear fracture parameters for cement based composites: theory and experiments," in *Application of fracture mechanics to cementitious composites*: Springer, 1985, pp. 319-359.

[16] L. Cedolin, "Fracture mechanics parameters and fracture process zone of concrete," in *Fracture of Non-Metallic Materials*: Springer, 1987, pp. 341-358.

[17] Z. P. Bažant and J. Planas, *Fracture and size effect in concrete and other quasibrittle materials*. Routledge, 2019.

[18] C. Y. Hui, S. J. Bennison, and J. D. Londono, "Crack blunting and the strength of soft elastic solids," *Proceedings of the Royal Society of London. Series A:*

Mathematical, Physical and Engineering Sciences, vol. 459, no. 2034, pp. 1489-1516, 2003.

[19] K. Ohno, K. Uji, A. Ueno, and M. Ohtsu, "Fracture process zone in notched concrete beam under three-point bending by acoustic emission," *Construction and building materials,* vol. 67, pp. 139-145, 2014.

[20] A. Tarokh and A. Fakhimi, "Discrete element simulation of the effect of particle size on the size of fracture process zone in quasi-brittle materials," *Computers and Geotechnics,* vol. 62, pp. 51-60, 2014.

[21] D. Vavrik and I. Jandejsek, "Experimental evaluation of contour J integral and energy dissipated in the fracture process zone," *Engineering Fracture Mechanics,* vol. 129, pp. 14-25, 2014.

[22] K. Ha, H. Baek, and K. Park, "Convergence of fracture process zone size in cohesive zone modeling," *Applied Mathematical Modelling,* vol. 39, no. 19, pp. 5828-5836, 2015.

[23] M. Fakoor and N. M. Khansari, "Mixed mode I/II fracture criterion for orthotropic materials based on damage zone properties," *Engineering Fracture Mechanics,* vol. 153, pp. 407-420, 2016.

[24] M. D. Wei, F. Dai, N. W. Xu, T. Zhao, and K. W. Xia, "Experimental and numerical study on the fracture process zone and fracture toughness determination for ISRM-suggested semi-circular bend rock specimen," *Engineering Fracture Mechanics,* vol. 154, pp. 43-56, 2016.

[25] J. Xie, A. M. Waas, and M. Rassaian, "Estimating the process zone length of fracture tests used in characterizing composites," *International Journal of Solids and Structures,* vol. 100, pp. 111-126, 2016.

[26] C. Comi, S. Mariani, and U. Perego, "An extended FE strategy for transition from continuum damage to mode I cohesive crack propagation," *International Journal for Numerical and Analytical Methods in Geomechanics,* vol. 31, no. 2, pp. 213-238, 2007.

[27] M. Modéer, "A fracture mechanics approach to failure analyses of concrete materials," Division of Building Materials, University of Lund Sweden, 1979.

[28] X. P. Xu and A. Needleman, "Numerical simulations of fast crack growth in brittle solids," *Journal of the Mechanics and Physics of Solids,* vol. 42, no. 9, pp. 1397-1434, 1994.

[29] J. H. Hanson and A. R. Ingraffea, "Using numerical simulations to compare the fracture toughness values for concrete from the size-effect, two-parameter and fictitious crack models," *Engineering fracture mechanics,* vol. 70, no. 7-8, pp. 1015-1027, 2003.

[30] J. Roesler, G. H. Paulino, K. Park, and C. Gaedicke, "Concrete fracture prediction using bilinear softening," *Cement and Concrete Composites,* vol. 29, no. 4, pp. 300-312, 2007.

[31] K. Park, G. H. Paulino, and J. R. Roesler, "Determination of the kink point in the bilinear softening model for concrete," *Engineering Fracture Mechanics,* vol. 75, no. 13, pp. 3806-3818, 2008.

[32] K. Park, G. H. Paulino, and J. Roesler, "Cohesive fracture model for functionally graded fiber reinforced concrete," *Cement and concrete research,* vol. 40, no. 6, pp. 956-965, 2010.

[33] F. Evangelista Jr, J. R. Roesler, and S. P. Proença, "Three-dimensional cohesive zone model for fracture of cementitious materials based on the thermodynamics of irreversible processes," *Engineering Fracture Mechanics,* vol. 97, pp. 261-280, 2013.

[34] L. Kachanov, *Introduction to continuum damage mechanics*. Springer Science & Business Media, 1986.

[35] J. Lemaitre and J.-L. Chaboche, *Mechanics of solid materials*. Cambridge university press, 1994.

[36] Z. P. Bazant and G. Pijaudier-Cabot, "Nonlocal continuum damage, localization instability and convergence," 1988.

[37] R. H. J. Peerlings, d. R. Borst, W. A. M. Brekelmans, and d. J. H. P. Vree, "Computational modelling of gradient-enhanced damage for fracture and fatigue problems," D. R. J. Owen and E. Onate, Eds., ed. Swansea: Pineridge Press, 1995, pp. 975-986.

[38] M. Jirasek, "Nonlocal models for damage and fracture: comparison of approaches," *International Journal of Solids and Structures,* vol. 35, no. 31-32, pp. 4133-4145, 1998.

[39] Z. P. Bažant, T. B. Belytschko, and T.-P. Chang, "Continuum theory for strain-softening," *Journal of Engineering Mechanics,* vol. 110, no. 12, pp. 1666-1692, 1984.

[40] A. Simone, G. N. Wells, and L. J. Sluys, "From continuous to discontinuous failure in a gradient-enhanced continuum damage model," *Computer Methods in Applied Mechanics and Engineering,* vol. 192, no. 41-42, pp. 4581-4607, 2003.

[41] G. Pijaudier-Cabot and Z. P. Bažant, "Nonlocal damage theory," *Journal of engineering mechanics,* vol. 113, no. 10, pp. 1512-1533, 1987.

[42] C. Comi, "A non-local model with tension and compression damage mechanisms," *European Journal of Mechanics-A/Solids,* vol. 20, no. 1, pp. 1-22, 2001.

[43] Z. P. Bažant and M. Jirásek, "Nonlocal integral formulations of plasticity and damage: survey of progress," *Journal of engineering mechanics,* vol. 128, no. 11, pp. 1119-1149, 2002.

[44] L. B. Rojas-Solano, D. Grégoire, and G. Pijaudier-Cabot, "Interaction-based non-local damage model for failure in quasi-brittle materials," *Mechanics Research Communications,* vol. 54, pp. 56-62, 2013.

[45] P. Grassl, D. Xenos, M. Jirásek, and M. Horák, "Evaluation of nonlocal approaches for modelling fracture near nonconvex boundaries," *International Journal of Solids and Structures,* vol. 51, no. 18, pp. 3239-3251, 2014.

[46] I. De-Pouplana and E. Oñate, "Combination of a non-local damage model for quasi-brittle materials with a mesh-adaptive finite element technique," *Finite Elements in Analysis and Design,* vol. 112, pp. 26-39, 2016.

[47] R. De Borst, J. Pamin, R. H. J. Peerlings, and L. J. Sluys, "On gradient-enhanced damage and plasticity models for failure in quasi-brittle and frictional materials," *Computational Mechanics,* vol. 17, no. 1, pp. 130-141, 1995.

[48] M. Frémond and B. Nedjar, "Damage, gradient of damage and principle of virtual power," *International journal of solids and structures,* vol. 33, no. 8, pp. 1083-1103, 1996.

[49] R. H. J. Peerlings, R. de Borst, W. A. M. Brekelmans, and J. H. P. de Vree, "Gradient enhanced damage for quasi-brittle materials," *International Journal for numerical methods in engineering,* vol. 39, no. 19, pp. 3391-3403, 1996.

[50] C. Comi and L. Driemeier, "On gradient regularization for numerical analyses in the presence of damage," 1998.

[51] C. Comi, "Computational modelling of gradient-enhanced damage in quasi-brittle materials," *Mechanics of Cohesive-frictional Materials: An International Journal on Experiments, Modelling and Computation of Materials and Structures,* vol. 4, no. 1, pp. 17-36, 1999.

[52] B. Vandoren and A. Simone, "Modeling and simulation of quasi-brittle failure with continuous anisotropic stress-based gradient-enhanced damage models," *Computer Methods in Applied Mechanics and Engineering,* vol. 332, pp. 644-685, 2018.

[53] J. G. Rots, P. Nauta, G. M. A. Kuster, and J. Blaauwendraad, "Smeared crack approach and fracture localization in concrete," *HERON, 30 (1), 1985,* 1985.

[54] A. Carpinteri, B. Chiaia, and K. M. Nemati, "Complex fracture energy dissipation in concrete under different loading conditions," *Mechanics of Materials,* vol. 26, no. 2, pp. 93-108, 1997.

[55] M. Jirásek and M. Bauer, "Numerical aspects of the crack band approach," *Computers & structures,* vol. 110, pp. 60-78, 2012.

[56] M. Kurumatani, K. Terada, J. Kato, T. Kyoya, and K. Kashiyama, "An isotropic damage model based on fracture mechanics for concrete," *Engineering Fracture Mechanics,* vol. 155, pp. 49-66, 2016.

[57] A. Wosatko, A. Genikomsou, J. Pamin, M. A. Polak, and A. Winnicki, "Examination of two regularized damage-plasticity models for concrete with regard to crack closing," *Engineering Fracture Mechanics,* vol. 194, pp. 190-211, 2018.

[58] Z. P. Bažant and G. Pijaudier-Cabot, "Measurement of characteristic length of nonlocal continuum," *Journal of engineering mechanics,* vol. 115, no. 4, pp. 755-767, 1989.

[59] E. Kuhl, E. Ramm, and R. de Borst, "An anisotropic gradient damage model for quasi-brittle materials," *Computer Methods in Applied Mechanics and Engineering,* vol. 183, no. 1-2, pp. 87-103, 2000.

[60] M. G. D. Geers, R. De Borst, W. A. M. Brekelmans, and R. H. J. Peerlings, "Strain-based transient-gradient damage model for failure analyses," *Computer methods in applied mechanics and engineering,* vol. 160, no. 1-2, pp. 133-153, 1998.

[61] A. Simone, H. Askes, and L. J. Sluys, "Incorrect initiation and propagation of failure in non-local and gradient-enhanced media," *International journal of solids and structures,* vol. 41, no. 2, pp. 351-363, 2004.

[62] A. Krayani, G. Pijaudier-Cabot, and F. Dufour, "Boundary effect on weight function in nonlocal damage model," *Engineering Fracture Mechanics,* vol. 76, no. 14, pp. 2217-2231, 2009.

[63] S. T. Pietruszczak and Z. Mroz, "Finite element analysis of deformation of strain-softening materials," *International Journal for Numerical Methods in Engineering,* vol. 17, no. 3, pp. 327-334, 1981.

[64] Z. P. Bazant, "CRACK BAND MODEL FOR FRACTURE OF GEOMATERIALS," Z. Eisenstein, Ed., ed: A. A. Balkema, 1982, pp. 1137-1152.

[65] Z. P. Bažant and B. H. Oh, "Crack band theory for fracture of concrete," *Matériaux et construction,* vol. 16, no. 3, pp. 155-177, 1983.

[66] J. G. Rots, "Computational modeling of concrete fracture," 1988.

[67] J. Oliver, "A consistent characteristic length for smeared cracking models," *International Journal for Numerical Methods in Engineering,* vol. 28, no. 2, pp. 461-474, 1989.

[68] J. Lubliner, J. Oliver, S. Oller, and E. Oñate, "A plastic-damage model for concrete," *International Journal of solids and structures,* vol. 25, no. 3, pp. 299-326, 1989.

[69] J. G. Rots and J. Blaauwendraad, "Crack models for concrete, discrete or smeared? Fixed, multi-directional or rotating?," *HERON, 34 (1), 1989,* 1989.

[70] G. N. Wells, L. J. Sluys, and R. de Borst, "Simulating the propagation of displacement discontinuities in a regularized strain-softening medium," *International Journal for Numerical Methods in Engineering,* vol. 53, no. 5, pp. 1235-1256, 2002.

[71] R. d. Borst, J. J. C. Remmers, A. Needleman, and M. A. Abellan, "Discrete vs smeared crack models for concrete fracture: bridging the gap," *International journal for numerical and analytical methods in geomechanics,* vol. 28, no. 7-8, pp. 583-607, 2004.

[72] S. Cuvilliez, F. Feyel, E. Lorentz, and S. Michel-Ponnelle, "A finite element approach coupling a continuous gradient damage model and a cohesive zone model within the framework of quasi-brittle failure," *Computer methods in applied mechanics and engineering,* vol. 237, pp. 244-259, 2012.

[73] J. Tejchman and J. Bobiński, "Continuous and discontinuous modelling of fracture in plain concrete under monotonic loading," *Continuous and Discontinuous Modelling of Fracture in Concrete Using FEM,* pp. 109-162, 2013.

[74] S.-N. Roth, P. Léger, and A. Soulaïmani, "A combined XFEM–damage mechanics approach for concrete crack propagation," *Computer Methods in Applied Mechanics and Engineering,* vol. 283, pp. 923-955, 2015.

[75] N. Moës and T. Belytschko, "Extended finite element method for cohesive crack growth," *Engineering fracture mechanics,* vol. 69, no. 7, pp. 813-833, 2002.

[76] A. B. Monteiro, A. R. V. Wolenski, F. B. Barros, R. L. S. Pitangueira, and S. S. Penna, "A computational framework for G/XFEM material nonlinear analysis," *Advances in Engineering Software,* vol. 114, pp. 380-393, 2017.

[77] A. R. V. Wolenski, A. B. Monteiro, S. S. Penna, R. L. d. S. Pitangueira, and F. B. Barros, "Damage propagation using novel G/XFEM strategies: computational aspects and numerical investigations," *Journal of the Brazilian Society of Mechanical Sciences and Engineering,* vol. 42, pp. 1-14, 2020.

[78] L. Novelli, T. S. de Oliveira, H. A. da Silveira Monteiro, G. M. Fonseca, R. L. da Silva Pitangueira, and F. B. Barros, "Stable Generalized/eXtended Finite Element Method with global–local enrichment for material nonlinear analysis," *Computer Methods in Applied Mechanics and Engineering,* vol. 372, p. 113429, 2020.

[79] J. Mazars, "Application de la mécanique de l'endommagement au comportement non linéaire et à la rupture du béton de structure," 1984.

[80] R. H. J. Peerlings, R. de Borst, W. A. M. Brekelmans, and M. G. D. Geers, "Gradient-enhanced damage modelling of concrete fracture," *Mechanics of Cohesive-frictional Materials: An International Journal on Experiments, Modelling and Computation of Materials and Structures,* vol. 3, no. 4, pp. 323-342, 1998.

[81] H. Schlangen, "Experimental and Numerical Analysis of Fracture Processes in Concrete," *HERON, 38 (2), 1993,* 1993.

[82] S. P. B. Proença and I. F. R. Torres, "Generalized finite element method for nonlinear three-dimensional analysis of solids," *International Journal of Computational Methods,* vol. 5, no. 01, pp. 37-62, 2008.

[83] J. H. P. De Vree, W. A. M. Brekelmans, and M. A. J. van Gils, "Comparison of nonlocal approaches in continuum damage mechanics," *Computers & Structures,* vol. 55, no. 4, pp. 581-588, 1995.

[84] M. Jirásek and P. Grassl, "Evaluation of directional mesh bias in concrete fracture simulations using continuum damage models," *Engineering Fracture Mechanics,* vol. 75, no. 8, pp. 1921-1943, 2008.

[85] F. Evangelista Jr, G. de Sousa Alves, J. F. A. Moreira, and G. O. F. de Paiva, "A global–local strategy with the generalized finite element framework for continuum damage models," *Computer Methods in Applied Mechanics and Engineering,* vol. 363, p. 112888, 2020.

[86] F. Evangelista Jr and J. F. A. Moreira, "A novel continuum damage model to simulate quasi-brittle failure in mode I and mixed-mode conditions using a continuous or a

continuous-discontinuous strategy," *Theoretical and Applied Fracture Mechanics,* vol. 109, p. 102745, 2020.

[87] J. Roesler, G. H. Paulino, K. Park, and C. Gaedicke, "Concrete fracture prediction using bilinear softening," *Cement and Concrete Composites,* vol. 29, no. 4, pp. 300-312, 2007a.

[88] F. Evangelista Jr, J. Roesler, and G. Paulino, "Numerical simulations of fracture resistance of functionally graded concrete materials," *Transportation Research Record,* vol. 2113, no. 1, pp. 122-131, 2009.

[89] Z. P. Bažant, "Concrete fracture models: testing and practice," *Engineering fracture mechanics,* vol. 69, no. 2, pp. 165-205, 2002.

[90] F. H. Wittmann, K. Rokugo, E. Brühwiler, H. Mihashi, and P. Simonin, "Fracture energy and strain softening of concrete as determined by means of compact tension specimens," *Materials and Structures,* vol. 21, no. 1, pp. 21-32, 1988.

[91] F. Evangelista Jr, J. R. Roesler, and C. A. Duarte, "Prediction of potential cracking failure modes in three-dimensional airfield rigid pavements with existing cracks and flaws," *Transportation research record,* vol. 2266, no. 1, pp. 11-19, 2012.

[92] *Determination of the fracture parameters (Kic and CTODc) of plain concrete using three-point bend tests*, RILEM, Committee on fracture mechanics of concrete-test methods, 1990.

[93] Y. Jenq and S. P. Shah, "Two parameter fracture model for concrete," *Journal of engineering mechanics,* vol. 111, no. 10, pp. 1227-1241, 1985.

[94] F. Evangelista Jr, J. R. Roesler, and S. P. Proença, "Three-dimensional cohesive zone model for fracture of cementitious materials based on the thermodynamics of irreversible processes," *Engineering Fracture Mechanics,* vol. 97, pp. 261-280, 2013a.

[95] C. Gaedicke, J. Roesler, and F. Evangelista Jr, "Three-dimensional cohesive crack model prediction of the flexural capacity of concrete slabs on soil," *Engineering Fracture Mechanics,* vol. 94, pp. 1-12, 2012.

[96] *Standard test method for splitting tensile strength of cylindrical concrete specimens*, A. C496-96, 1996.

[97] Ba and M. T. Kazemi, "Determination of fracture energy, process zone length and brittleness number from size effect, with application to rock and conerete," *International Journal of fracture,* vol. 44, no. 2, pp. 111-131, 1990.

[98] J. J. Ortega *et al.*, "Number of tests and corresponding error in concrete fatigue," *International journal of fatigue,* vol. 116, pp. 210-219, 2018.

[99] M. B. Nooru-Mohamed, "Mixed-mode fracture of concrete: an experimental approach," Delft University of Technology, Netherlands, 1992.

[100] O. L. Manzoli, M. A. Maedo, L. A. G. Bitencourt Jr, and E. A. Rodrigues, "On the use of finite elements with a high aspect ratio for modeling cracks in quasi-brittle materials," *Engineering Fracture Mechanics,* vol. 153, pp. 151-170, 2016.

[101] Z. Gao, L. Zhang, and W. Yu, "A nonlocal continuum damage model for brittle fracture," *Engineering Fracture Mechanics,* vol. 189, pp. 481-500, 2018.

[102] M. R. Javanmardi and M. R. Maheri, "Extended finite element method and anisotropic damage plasticity for modelling crack propagation in concrete," *Finite Elements in Analysis and Design,* vol. 165, pp. 1-20, 2019.

[103] C. Feist and G. Hofstetter, "An embedded strong discontinuity model for cracking of plain concrete," *Computer Methods in Applied Mechanics and Engineering,* vol. 195, no. 52, pp. 7115-7138, 2006.

[104] J. R. Roesler, V. G. Cervantes, and A. N. Amirkhanian, "Accelerated performance testing of concrete pavement with short slabs," *International Journal of Pavement Engineering,* vol. 13, no. 6, pp. 494-507, 2012.
[105] *Standard Test Method for Determining Fracture Energy of Asphalt-Aggregate Mixtures Using the Disk-Shaped Compact Tension Geometry*, A. D7313-13, West Conshohocken, PA,, 2013.
[106] A. M. Ioannides, J. Peng, and J. R. Swindler Jr, "ABAQUS model for PCC slab cracking," *International Journal of Pavement Engineering,* vol. 7, no. 4, pp. 311-321, 2006.
[107] G. Gioia and Z. P. Bažant, "ls no-tension dam design always safe?-a numerical study," 1992.
[108] J.-Y. Wu, J.-F. Qiu, V. P. Nguyen, T. K. Mandal, and L.-J. Zhuang, "Computational modeling of localized failure in solids: XFEM vs PF-CZM," *Computer Methods in Applied Mechanics and Engineering,* vol. 345, pp. 618-643, 2019.
[109] K. Park, G. H. Paulino, and J. R. Roesler, "A unified potential-based cohesive model of mixed-mode fracture," *Journal of the Mechanics and Physics of Solids,* vol. 57, no. 6, pp. 891-908, 2009.
[110] A. Needleman, "A continuum model for void nucleation by inclusion debonding," 1987.
[111] V. Tvergaard, "Material failure by void growth to coalescence," *Advances in applied Mechanics,* vol. 27, pp. 83-151, 1989.
[112] A. Needleman, "An analysis of tensile decohesion along an interface," *Journal of the Mechanics and Physics of Solids,* vol. 38, no. 3, pp. 289-324, 1990.
[113] X. P. Xu and A. Needleman, "Void nucleation by inclusion debonding in a crystal matrix," *Modelling and Simulation in Materials Science and engineering,* vol. 1, no. 2, p. 111, 1993.
[114] K. Park and G. H. Paulino, "Cohesive zone models: a critical review of traction-separation relationships across fracture surfaces," *Applied Mechanics Reviews,* vol. 64, no. 6, 2011.
[115] J. Roesler, G. Paulino, C. Gaedicke, A. Bordelon, and K. Park, "Fracture behavior of functionally graded concrete materials for rigid pavements," *Transportation Research Record,* vol. 2037, no. 1, pp. 40-49, 2007b.
[116] F. Evangelista Jr and J. Roesler, "Top-down cracking predictions for airfield rigid pavements," *Transportation research record,* vol. 2095, no. 1, pp. 13-23, 2009.
[117] C. Gaedicke and J. Roesler, "Fracture-based method to determine flexural capacity of concrete beams on soil," *Road materials and pavement design,* vol. 11, no. 2, pp. 361-385, 2010.
[118] K. Park and G. H. Paulino, "Computational implementation of the PPR potential-based cohesive model in ABAQUS: Educational perspective," *Engineering fracture mechanics,* vol. 93, pp. 239-262, 2012.
[119] A. Cerrone, P. Wawrzynek, A. Nonn, G. H. Paulino, and A. Ingraffea, "Implementation and verification of the Park–Paulino–Roesler cohesive zone model in 3D," *Engineering Fracture Mechanics,* vol. 120, pp. 26-42, 2014.
[120] D. W. Spring and G. H. Paulino, "A growing library of three-dimensional cohesive elements for use in ABAQUS," *Engineering Fracture Mechanics,* vol. 126, pp. 190-216, 2014.
[121] D. W. Spring and G. H. Paulino, "Computational homogenization of the debonding of particle reinforced composites: The role of interphases in interfaces," *Computational Materials Science,* vol. 109, pp. 209-224, 2015.

[122] D. W. Spring, O. Giraldo-Londono, and G. H. Paulino, "A study on the thermodynamic consistency of the Park–Paulino–Roesler (PPR) cohesive fracture model," *Mechanics Research Communications,* vol. 78, pp. 100-109, 2016.
[123] P. Gilormini and J. Diani, "Some features of the PPR cohesive-zone model combined with a linear unloading/reloading relationship," *Engineering Fracture Mechanics,* vol. 173, pp. 32-40, 2017.
[124] Y. Li, J. G. Deng, W. Liu, and Y. Feng, "Modeling hydraulic fracture propagation using cohesive zone model equipped with frictional contact capability," *Computers and geotechnics,* vol. 91, pp. 58-70, 2017.
[125] L. A. M. Camones, E. d. A. Vargas Jr, R. Q. Velloso, and G. H. Paulino, "Simulation of hydraulic fracturing processes in rocks by coupling the lattice Boltzmann model and the Park-Paulino-Roesler potential-based cohesive zone model," *International Journal of Rock Mechanics and Mining Sciences,* vol. 112, pp. 339-353, 2018.
[126] I. Babuška, G. Caloz, and J. E. Osborn, "Special finite element methods for a class of second order elliptic problems with rough coefficients," *SIAM Journal on Numerical Analysis,* vol. 31, no. 4, pp. 945-981, 1994.
[127] C. A. Duarte and J. Oden, *Hp Clouds - A Meshless Method to Solve Boundary-Value Problems*. 1995.
[128] C. A. Duarte, "The hp cloud method," 1996.
[129] C. A. Duarte and J. T. Oden, "An hp adaptive method using clouds," *Computer methods in applied mechanics and engineering,* vol. 139, no. 1-4, pp. 237-262, 1996.
[130] J. M. Melenk and I. Babuška, "The partition of unity finite element method: basic theory and applications," *Computer methods in applied mechanics and engineering,* vol. 139, no. 1-4, pp. 289-314, 1996.
[131] N. Moës, J. Dolbow, and T. Belytschko, "A finite element method for crack growth without remeshing," *International journal for numerical methods in engineering,* vol. 46, no. 1, pp. 131-150, 1999.
[132] N. Sukumar, N. Moës, B. Moran, and T. Belytschko, "Extended finite element method for three-dimensional crack modelling," *International journal for numerical methods in engineering,* vol. 48, no. 11, pp. 1549-1570, 2000.
[133] J. Dolbow, N. Moës, and T. Belytschko, "Discontinuous enrichment in finite elements with a partition of unity method," *Finite elements in analysis and design,* vol. 36, no. 3-4, pp. 235-260, 2000.
[134] T. Belytschko, N. Moës, S. Usui, and C. Parimi, "Arbitrary discontinuities in finite elements," *International Journal for Numerical Methods in Engineering,* vol. 50, no. 4, pp. 993-1013, 2001.
[135] N. Moës, A. Gravouil, and T. Belytschko, "Non-planar 3D crack growth by the extended finite element and level sets—Part I: Mechanical model," *International journal for numerical methods in engineering,* vol. 53, no. 11, pp. 2549-2568, 2002.
[136] A. Gravouil, N. Moës, and T. Belytschko, "Non-planar 3D crack growth by the extended finite element and level sets—Part II: Level set update," *International journal for numerical methods in engineering,* vol. 53, no. 11, pp. 2569-2586, 2002.
[137] F. L. Stazi, E. Budyn, J. Chessa, and T. Belytschko, "An extended finite element method with higher-order elements for curved cracks," *Computational Mechanics,* vol. 31, no. 1, pp. 38-48, 2003.
[138] G. N. Wells and L. J. Sluys, "A new method for modelling cohesive cracks using finite elements," *International Journal for numerical methods in engineering,* vol. 50, no. 12, pp. 2667-2682, 2001.

[139] S. Mariani and U. Perego, "Extended finite element method for quasi-brittle fracture," *International Journal for Numerical Methods in Engineering,* vol. 58, no. 1, pp. 103-126, 2003.
[140] J. F. Unger, S. Eckardt, and C. Könke, "Modelling of cohesive crack growth in concrete structures with the extended finite element method," *Computer methods in applied mechanics and engineering,* vol. 196, no. 41-44, pp. 4087-4100, 2007.
[141] G. Meschke and P. Dumstorff, "Energy-based modeling of cohesive and cohesionless cracks via X-FEM," *Computer methods in applied mechanics and engineering,* vol. 196, no. 21-24, pp. 2338-2357, 2007.
[142] J. V. Cox, "An extended finite element method with analytical enrichment for cohesive crack modeling," *International Journal for Numerical Methods in Engineering,* vol. 78, no. 1, pp. 48-83, 2009.
[143] A. Zamani, R. Gracie, and M. Reza Eslami, "Cohesive and non-cohesive fracture by higher-order enrichment of XFEM," *International Journal for Numerical Methods in Engineering,* vol. 90, no. 4, pp. 452-483, 2012.
[144] J. Jaśkowiec and F. P. van der Meer, "A consistent iterative scheme for 2D and 3D cohesive crack analysis in XFEM," *Computers & Structures,* vol. 136, pp. 98-107, 2014.
[145] Ł. Kaczmarczyk, M. M. Nezhad, and C. Pearce, "Three-dimensional brittle fracture: configurational-force-driven crack propagation," *International Journal for Numerical Methods in Engineering,* vol. 97, no. 7, pp. 531-550, 2014.
[146] J. Kim and C. A. Duarte, "A new generalized finite element method for two-scale simulations of propagating cohesive fractures in 3-D," *International Journal for Numerical Methods in Engineering,* vol. 104, no. 13, pp. 1139-1172, 2015.
[147] G. Ferté, P. Massin, and N. Moes, "3D crack propagation with cohesive elements in the extended finite element method," *Computer Methods in Applied Mechanics and Engineering,* vol. 300, pp. 347-374, 2016.
[148] A. Simone, "Partition of unity-based discontinuous finite elements: GFEM, PUFEM, XFEM," *Revue européenne de génie civil,* vol. 11, no. 7-8, pp. 1045-1068, 2007.
[149] F. Evangelista Jr, J. R. Roesler, and C. A. Duarte, "Two-scale approach to predict multi-site cracking potential in 3-d structures using the generalized finite element method," *International Journal of Solids and Structures,* vol. 50, no. 13, pp. 1991-2002, 2013b.
[150] R. De Borst, "Numerical aspects of cohesive-zone models," *Engineering fracture mechanics,* vol. 70, no. 14, pp. 1743-1757, 2003.
[151] J. P. Pereira, C. A. Duarte, D. Guoy, and X. Jiao, "hp-Generalized FEM and crack surface representation for non-planar 3-D cracks," *International Journal for Numerical Methods in Engineering,* vol. 77, no. 5, pp. 601-633, 2009.
[152] P. M. A. Areias and T. Belytschko, "Analysis of three-dimensional crack initiation and propagation using the extended finite element method," *International journal for numerical methods in engineering,* vol. 63, no. 5, pp. 760-788, 2005.
[153] *Standard Test Method for Splitting Tensile Strength of Cylindrical Concrete Specimens*, A. C. C496M-17, West Conshohocken, PA, 2017.
[154] N. A. García, "Quantificação da Incerteza em modelos de fratura e fadiga utilizando polinômios de expansão de caos," 2019.
[155] J. R. Reeder and J. H. Crews Jr, "Mixed-mode bending method for delamination testing," *AiAA Journal,* vol. 28, no. 7, pp. 1270-1276, 1990.
[156] *Standard Test Method for Mixed Mode I-Mode II Interlaminar Fracture Toughness of Unidirectional Fiber Reinforced Polymer Matrix Composites*, A. D. D6671M-13e1, West Conshohocken, PA, 2013.

[157] R. Dimitri, M. Trullo, L. De Lorenzis, and G. Zavarise, "Coupled cohesive zone models for mixed-mode fracture: A comparative study," *Engineering Fracture Mechanics,* vol. 148, pp. 145-179, 2015.

[158] O. Giraldo-Londoño, D. W. Spring, G. H. Paulino, and W. G. Buttlar, "An efficient mixed-mode rate-dependent cohesive fracture model using sigmoidal functions," *Engineering Fracture Mechanics,* vol. 192, pp. 307-327, 2018.

[159] Y. Mi, M. A. Crisfield, G. A. O. Davies, and H. B. Hellweg, "Progressive delamination using interface elements," *Journal of composite materials,* vol. 32, no. 14, pp. 1246-1272, 1998.

[160] J.-Y. Wu, F.-B. Li, and S.-L. Xu, "Extended embedded finite elements with continuous displacement jumps for the modeling of localized failure in solids," *Computer Methods in Applied Mechanics and Engineering,* vol. 285, pp. 346-378, 2015.

[161] X. Li and J. Chen, "An extended cohesive damage model for simulating arbitrary damage propagation in engineering materials," *Computer Methods in Applied Mechanics and Engineering,* vol. 315, pp. 744-759, 2017.